

**Phytoplankton Aggregations in a Turbulent Boundary
Layer**

Thesis submitted in accordance
with the requirements of the
University of Liverpool
for the degree of
Doctor in Philosophy
by

Ashley Brereton

August 2013

Acknowledgements

I would firstly like to thank my supervisor, Dr David Lewis, for his unbridled support throughout this challenging experience. The amount of patience and dedication he has given to my work was inspirational and uplifting and really gave me the drive to complete what was, at first, a daunting task. Although this research reached cul-de-sac after cul-de-sac, David was never fazed and always saw direction when I saw none, which gave me the confidence to carry on. David is a natural teacher and a brilliant academic nurturer and I feel very lucky to have been his student.

My PhD colleagues have been very helpful throughout the last 4 years of my student life, giving me much needed help and support and of course, scintillating discussion about my academic problems, in particular, Joe, Nigel, Graham, Andy, Heather, Jenna, Katy, Weihong, Stewart, Kirk, Ma, Joe P and Anwar. Other research collaborators have helped broaden my academic horizon, one that stands out is Vincent Hughes, who has introduced me to the fascinating world of forensic linguistics and has engaged me fully into his research.

A big thank you goes to my beautiful girlfriend Kat for her love and patience, and her ability to always keep me levelled even when stress was at an all time high. Also, to her extremely supporting family who have, in a manner of speaking, adopted me as their own. Thank you also to my family, for their continued help and support.

Contents

| | | |
|----------|--|-----------|
| 1 | Introduction | 7 |
| 2 | The Physical Model | 15 |
| 2.1 | The Reynolds Number, Re | 16 |
| 2.2 | Some Basic Observations on Solutions to Laminar Flow | 17 |
| 2.2.1 | Stokes' Equations | 17 |
| 2.2.2 | General Solutions for Laplace's Equation | 18 |
| 2.3 | Characteristics of Turbulent Dynamics | 20 |
| 2.3.1 | Eddies | 20 |
| 2.3.2 | The Kolmogorov Microscales | 21 |
| 2.3.3 | Spectral Dynamics and the Eddy Cascade | 22 |
| 2.3.4 | $E(k)$ in the Inertial Subrange | 26 |
| 2.4 | Langmuir Turbulence | 29 |
| 2.4.1 | Stokes Drift | 29 |
| 2.4.2 | Craik-Leibovich Equations | 34 |
| 2.4.3 | Consequences of Langmuir Turbulence | 35 |
| 2.5 | Large Eddy Simulation (LES) | 37 |
| 2.5.1 | Resolution Scales | 38 |
| 2.5.2 | Filtering | 39 |
| 2.5.3 | Smagorinsky Scheme | 40 |
| 2.5.4 | Numerical Techniques | 41 |

| | | |
|----------|--|-----------|
| 2.6 | Boundary Conditions | 43 |
| 3 | The Biological Model | 45 |
| 3.1 | The Nutrient-Phytoplankton-Zooplankton (NPZ) Model | 45 |
| 3.2 | Derivations of the Biological Terms | 48 |
| 3.2.1 | Nutrient Uptake by Phytoplankton | 49 |
| 3.2.2 | Phytoplankton Growth | 56 |
| 3.2.3 | Nitrate Recycled from Phytoplankton | 56 |
| 3.2.4 | Zooplankton Predation | 56 |
| 3.2.5 | Zooplankton Growth | 73 |
| 3.2.6 | Zooplankton Death | 73 |
| 3.3 | Nutrient Surges | 74 |
| 3.4 | Coupling of the LES to the NPZ | 77 |
| 3.5 | Table of Parameters | 80 |
| 4 | Model Analysis | 81 |
| 4.1 | Flow Statistics | 81 |
| 4.2 | Statistical Stability | 84 |
| 4.2.1 | Shear Turbulence (Ekman boundary layers) | 85 |
| 4.2.2 | Langmuir Turbulence (Stokes-Ekman boundary layers) | 93 |
| 4.3 | Effect of Wind on the Mixed Layer | 97 |
| 4.3.1 | Relationship Between Stokes Drift and Wind Speed | 97 |
| 4.3.2 | Wind Penetration | 98 |
| 4.4 | Analysing the NPZ Equations | 102 |
| 4.4.1 | Reducing the LES-NPZ Model for Simple Analysis | 102 |
| 4.4.2 | Stability Analysis | 103 |
| 4.4.3 | Near Extinction Behaviour | 108 |
| 4.5 | Wind Stress Effect on Biology | 112 |
| 4.5.1 | Phase Locking | 112 |
| 4.5.2 | Thin Phytoplankton Layers | 113 |

| | | |
|----------|---|------------|
| 5 | Aggregation Intensity Analysis | 119 |
| 5.1 | Plankton Aggregation Definitions | 119 |
| 5.1.1 | Aggregation Measures | 119 |
| 5.2 | Aggregation Intensity Dynamics | 124 |
| 5.2.1 | Aggregation Intensity Dynamical Decomposition | 125 |
| 5.2.2 | Biology vs. Flow | 128 |
| 5.2.3 | Biological Correlations | 134 |
| 5.3 | Effect of Friction Velocity, U_* | 139 |
| 5.3.1 | Aggregation Depth Dependence | 139 |
| 5.3.2 | Aggregation Intensity Magnitude | 144 |
| 5.3.3 | Effect of Mixed Layer Depth, z_{ML} | 145 |
| 5.4 | Effect of Biology on Aggregation Intensity | 148 |
| 5.4.1 | Phytoplankton Growth Rate, μ_P^{max} | 148 |
| 5.4.2 | Nutrient Pump Strength, Q | 151 |
| 5.4.3 | Zooplankton Contact Radius, R | 153 |
| 5.5 | Aggregation Depth and Time Persistence | 154 |
| 5.5.1 | Aggregation Thickness | 155 |
| 5.5.2 | Aggregation Time Persistence | 160 |
| 5.6 | Aggregation Distributions | 164 |
| 5.6.1 | Physical and Biological Correlation | 165 |
| 5.6.2 | Phytoplankton Structures | 166 |
| 6 | Summary | 173 |
| 6.1 | Discussion | 173 |
| 6.2 | Future Work | 177 |

Chapter 1

Introduction

Global warming has received a considerable amount of attention in recent years, with many studies presenting strong evidence for its existence (Hughes, 2000). There are many impacted areas resulting from this phenomenon and many studies have been undertaken to find out the causes and effects. A variety of reasons have been postulated as to why this is happening, however what is inescapable is the fact that atmospheric carbon levels are higher now, than in the last 26 million years (Long et al., 2004). This increased level of carbon in the atmosphere fuels the greenhouse effect, underlying the observed increases in average global temperatures in recent decades. This temperature increase has a profound impact on ecosystems across the world (Levy et al., 2004). Furthermore, studies have shown that carbon quotas in the atmosphere are increasing at an alarming rate (Cox et al., 2000; Loarie et al., 2009). The main biological regulator of atmospheric carbon is plant life, which synthesises energy from carbon dioxide via photosynthesis, giving out oxygen. However, the rate of increase in carbon emissions over the last couple of decades, combined with massive deforestation, threatens to overwhelm the delicate regulatory balance of the global ecosystem. This is likely to result in ‘permanently’ higher global temperatures, higher sea levels and floods, due to melting ice shelves and disruption to ocean current circulations. Biologically and economically, the results would be disastrous. For example, higher atmospheric carbon levels have been shown to directly effect certain phytoplankton species mortality rates

by increasing ocean acidity (Lewandowska et al., 2012). Planktonic ecosystems are particularly vulnerable to damage and dislocation brought on by rising temperatures, as their ocean environment will experience changes in salinity, viscosity, acidity and oxygen content, as well as profound changes in its dynamics. The interactions that govern the means by which a particular planktonic population flourishes in particular regions of the ocean are complex and poorly understood. One of the aims of this thesis will be to systematically investigate how the local fluid dynamics influence the biological environment.

Phytoplankton make up the most abundant of plant forms on the planet, inhabiting the world's oceans in enormous populations. Most are confined to the upper ocean mixed layer where sunlight for photosynthesis is relatively high (the euphotic zone). Despite being primarily unicellular, they are responsible for supplying the world with 50% of its total oxygen and take in a huge amount of carbon dioxide and store the carbon in the deep ocean (McQuatters-Gollop et al., 2011). As one of the first residents of the earth, starting life more than 2 billion years ago (Ratti et al., 2011), they have evolved strategies to survive and flourish in many situations.

Observations from satellite data (Abbott and Zion, 1985; Álvarez-Molina et al., 2013; Duggen et al., 2007) have given much insight into the mechanisms behind phytoplankton blooms and the dynamics have been carefully studied for a considerable time. Many mechanisms have been put forward to explain these vast, heterogeneous blooms. Phytoplankton blooms come in a range of sizes from the kilometre scale blooms which last for a number of weeks, to millimetre scale aggregations, which last for very short periods (Alvain et al., 2008). One of the unanswered questions in this field is: can a unified theory between the small scale patches and the large scale patches be established? Another curious behaviour about some phytoplankton blooms is that horizontally, they can span kilometres, yet vertically, they are of the order of 1 metre in thickness, these are referred to as thin layers (Cheriton et al., 2009; Durham and Stocker, 2012). Thin

layers have many proposed mechanisms, for example density stratification, whereby the phytoplankton aggregate in small regions where they are neutrally buoyant (Rines et al., 2010) and gyrotactic trapping, where bottom heavy swimming phytoplankton swim upwards and encounter sharp gradients in shearing motion, where they start to tumble and are no longer able to naturally swim upwards (Durham et al., 2011b; Lewis, 2003a; Thorn and Bearon, 2010). There is vortical trapping, where small scale vortices in the flow literally trap small amounts of phytoplankton inside (Durham et al., 2011c), which leads to a small scale ephemeral aggregation. Underestimations should not be made to the impact of small scale processes on large scale structures (Lévy et al., 2012), turbulence and its effect on large scale dynamics is a good example of this, which will be discussed in chapter 2. Another aim of this thesis is to explore whether small scale aggregations can initiate large scale blooms.

Although there are many processes which possibly enhance aggregations, predator-prey interactions and the source of nutrients govern the underpinning mechanism behind the spatial structure of phytoplankton. Mathematical modelling has developed greatly in the last few decades with the popular Nutrient-Phytoplankton-Zooplankton (NPZ) model (Franks et al., 1986; Roy et al., 2012). Zooplankton are tiny animals, although usually a lot larger than phytoplankton. Zooplankton are generally classified in two subgroups, micro-zooplankton ($10^{-5}\text{m} - 10^{-4}\text{m}$) and macro-zooplankton ($10^{-4}\text{m} - 10^{-3}\text{m}$), although there is no exact dichotomy. Together they form the next rung of the oceanic food chain, founded on the phytoplankton. The key feature that the zooplankton as a class share with phytoplankton is their relatively small size, which means that they are highly dependant upon their local fluid environment when foraging for prey, as the chaotic nature of a turbulent flow can make capturing a prey a difficult proposition. In the ocean mixed layer, one often finds a predatory (zooplankton) - prey (phytoplankton) cycle regulating the biology (Eiser and Hassett, 1994; Muylaert et al., 2010). This oscillatory behaviour has been observed many times in experiments, when species of phytoplankton and zooplankton are abundant for a certain amount of time

before they vanish and then reappear, usually in the same place as before (Sommer and Lewandowska, 2011). Nutrient sources, such as Nitrates and Phosphates, which are brought up from deep waters into sunlit regions of the oceans (euphotic zones), via ocean currents, are also instrumental to the phytoplankton temporal dynamics (Williams, 2011). It is key that this network needs a large amount of consideration, to really understand the spatial dynamics of the biology.

Large-scale models have long been used to examine the spatial structures of phytoplankton (Dubois, 1975; Denman and Platt, 1976; Powell and Okubo, 1994). Usually, turbulence is modelled either by isotropic turbulence assumptions (Kolmogorov, 1941) (i.e. the cascading property is based on the turbulent kinetic energy) or in two dimensions (Kraichnan, 1976) (where the cascading model is based on enstrophy, which is essentially a measure of the vorticity squared) (Martin, 2003). High resolution models give insight into the role of smaller scale flows on larger scales, for instance, global circulation models which resolve meso-scale eddies and how these dynamics add consequence to primary production levels (Fouest et al., 2006; McGillicuddy et al., 1998; Lewis, 2002). With the advent of community based models, such as the Nucleus for European Modelling of the Ocean (NEMO) (Madec, 2008), which is a structured grid model now being developed by a vast network of researchers. This gives the advantage of testing out various ecosystem models which have been coupled, for example the European Regional Seas Ecosystem Model (ERSEM) (Baretta et al., 1995; Baretta-Bekker et al., 1997), which is a complicated biogeochemical cycling model and the HADley centre Ocean Carbon Cycle model (HadOCC) (Cox et al., 2000), which is a relatively simple NPZD (Nutrient Phytoplankton Zooplankton Detritus) model developed by the Met Office. Also, the advantage of NEMO is that it comes equipped with various turbulence parametrisations, most notably, the General Ocean Turbulence Model (GOTM) (Burchard et al., 1999). Although only 1-dimensional (vertical mixing) currently, it carries with it a suite of turbulence parametrisations for testing against different scenarios in oceanic and ecosystem modelling. There are also unstructured grid software

available which incorporate similar moduled components to that of NEMO, for example the the unstructured grid Finite Volume Coastal Ocean Model (FVCOM) (Chen et al., 2006), which can be used to increase resolution in selective regions of the domain and includes various ecosystem models (Franks et al., 1986; Steele, 2006) with a pool of biological variables to develop custom models.

Although advancements in macro-scale modelling have come a long way in recent years, they are still nowhere near being able to predict spatial structures of biology, which was shown quite elegantly in Abraham (1998), that the Fourier power spectra associated with plankton distribution changes significantly when subjected to non-linear, submeso-scale resolved flow. Although Abraham only gives a very simple inclusion of small-scale advections (via the seeded-eddy model), it is still a powerful example of how small scale dynamics play a fundamental role in the structure of biological concentrations in the ubiquitously turbulent ocean. Many studies have also made comparisons between the spectra of phytoplankton distribution and inert tracers such as temperature and salinity (Seuront et al., 1996; Denman and Platt, 1976). This method however, does not take into account the flow field itself being dependent upon temperature and salinity distributions, as these effect density and convective currents (Lovejoy et al., 2001) (and hence, not strictly passive). in other words, these “inert” tracers cannot necessarily be used as a proxy for chlorophyll distribution (Mahadevan and Campbell, 2002). Vorticity is another key factor proposed in the distribution, with spectra of vorticity being closely linked to the spectra of phytoplankton and zooplankton, as plankton species are more abundant in vorticity (Levy et al., 2004) and hence small scale eddies which are not directly resolved will have impact on spatial distribution.

Small-scale modelling, particularly with the use of direct numerical simulation (DNS), gives an insight into how small scale dynamics have a big effect on the spatial distribution of phytoplankton. Recent studies have shown how small scale turbulence interacts heavily with biological distributions, in particular how vortices bias a motile,

gyrotactic cell towards the centre of vorticity (Durham et al., 2011a, 2013). DNS can also be used to test biological parameters, such as uptake rate in various turbulent flow regimes (Taylor and Stocker, 2012), but this will not be the focus of this work. The fact that eddies have been shown to effect biological distributions on small and large scales makes it surprising that the investigation into intermediate scales (sub-meso and lower) has not been looked into in great detail, with only a handful of papers investigating biological dynamics on these scales (Lewis, 2005; Taylor and Ferrari, 2011). One of the most prominent structures on this scale is the so-called Langmuir circulation, after its discoverer (Langmuir, 1938). These Langmuir cells are vortical by nature and have a readily observable consequence in the form of wind rows (these circulations will be discussed in more detail in chapter 2). The motivation behind the investigation into this scale stems from the lack of literature in this field, the advancements in computer power allowing such scales to be resolved and the clear indication that eddies on all scales have their own quality in the developmental phase of biological spatial structure. For example, on sub-meso scales, strong upwellings, which are not apparent in large-scale hydrostatic models, play a significant role in pumping nutrients from deep waters to the euphotic zone (Lévy et al., 2001; Martin et al., 2002).

Studying the mechanisms, for this reason, is extremely important. The influence of fluid dynamics on plankton populations and distributions has been a fertile area of research for many decades. Many such studies involve laminar flows (Latz et al., 1994), as laminar flow is a well understood field of fluid dynamics. However, little is understood about bloom formation in turbulent flows, how these tiny plants overcome the strong mixing mechanisms associated with turbulence and how they even manage to flourish in such environments. Intuitively, one would expect that in turbulent flows, small organisms would be dispersed by the flow and unable to aggregate at all. But it has been observed in many settings that phytoplankton blooms are highly heterogeneous in structure and densely aggregated in predominantly turbulent flows (Sanford, 1997; Steinbuck et al., 2010). Many studies have coupled simple flow fields into the biological

dynamics to capture possible reasons for the aggregation of phytoplankton, which is a first step in really understanding the dynamics of this complex system (Doney et al., 1996; Fennel et al., 2011; Franks, 2002; Sibert et al., 2011). The suspicion is that whilst turbulent mixing is undoubtedly a means of breaking down planktonic aggregations, some other inter-related property of the turbulent boundary layer actually acts to promote aggregation. For example, where turbulent mixing is less strong deeper in the boundary layer and upwelling of flow (and hence nutrients) are prominent. A third aim of this thesis will be to try and establish whether this supposition is correct.

In order to answer these questions, it is necessary to couple a working model of the ocean boundary layer in combination with a type of generic NPZ model discussed above. Up to now, the problem with this kind of combined model is that computers were simply not powerful enough to numerically integrate these types of systems to the level of spatial accuracy needed over long enough time periods, for biological concentrations to manifest themselves. However, modern computing resources are now so extensive that it has become possible to employ a technique known as large-eddy simulation (LES) to formulate a fully 3-dimensional model of the ocean boundary layer which can combine with the NPZ model. Large-eddy simulation (LES) is a method whereby large scale flow features can be solved exactly whilst small scale is modelled. Incorporation of this flow field model into a standard generic type advection-diffusion style NPZ model will be used to model the effects of phytoplankton behaviour, without any enhancing effects, such as density stratification and cell swimming, to establish if there are any general mechanisms behind the formation of blooms in typical boundary layers.

Chapter 2

The Physical Model

The governing equations of fluid flow are called the Navier-Stokes equations, first formulated by Navier (1827). These equations are derived from Newton's second law of motion (Force = mass \times acceleration) and give us the various velocities and pressures at prescribed points in space and time. This is fundamental to studying any biological process which occurs in a fluid, particularly a turbulent fluid. The equations can be stated as follows:

$$\frac{\partial u_i}{\partial t} + u_j \frac{\partial u_i}{\partial x_j} = -\frac{1}{\rho} \frac{\partial p}{\partial x_i} + \nu \frac{\partial^2 u_i}{\partial x_j \partial x_j} + F_i, \quad (2.1)$$

where u_i - velocity component, t - time, x_i - displacement, ρ - density, p - hydrodynamic pressure, ν - viscosity, F - body forces (gravity, buoyancy etc) and i is the dimension ($i = 1 : 3$ for 3-dimensional space).

However, since there are 4 variables and only 3 equations, another equation is needed. This equation is known as the continuity equation. This equation implies there is a conservation of mass and can be given in the form (Happel and Brenner, 1965)

$$\frac{D\rho}{Dt} = -\rho \frac{\partial u_i}{\partial x_i}, \quad (2.2)$$

where $\frac{D}{Dt} = \frac{\partial}{\partial t} + u_j \frac{\partial}{\partial x_j}$ is the material derivative.

Fluids can be classed very broadly into two categories, compressible and incompressible, which describes how the volume of the fluid changes subject to an external force. A property of an incompressible fluid is that when a fixed volume of the fluid is subjected to a force, the volume of that fluid stays fixed. As a consequence, the density remains constant for all space and time, so it follows from equation 2.2 that

$$\frac{\partial u_i}{\partial x_i} = 0, \quad (2.3)$$

where equation 2.3 is used to close the Navier-Stokes equations.

2.1 The Reynolds Number, Re

The Navier-Stokes equations are extremely complex and have no analytical solutions to date. However, certain simplifications can be made for when a fluid has low Reynolds number. The difference between a low energy flow (laminar) and a high energy flow (turbulent) is associated with which physical process dominates. In a laminar flow the linear viscous term dominates over the non-linear advection term, this is advantageous as then the equations can be linearised and in some cases, analytically solved. In a turbulent flow, however, the equations are non-linear and cannot be solved analytically and so numerical techniques must be employed.

Non-dimensionalisation of the Navier-Stokes equations show which parameters are conducive in determining the type of flow that can be expected (Stokes, 1851). Using the dimensionless quantities $x^* = \frac{x}{L}$, $u^* = \frac{u}{U}$, $t^* = \frac{U t}{L}$, $p^* = \frac{U^2 p}{\rho}$, where U and L are velocity and length scales respectively (and removing the asterisk for brevity), the Navier-Stokes equations become

$$\frac{\partial u_i}{\partial t} + u_j \frac{\partial u_i}{\partial x_j} = -\frac{\partial p}{\partial x_i} + \frac{1}{Re} \frac{\partial^2 u_i}{\partial x_j \partial x_j} + F_i, \quad (2.4)$$

where $Re = \frac{UL}{\nu}$ is the Reynolds number.

Equation 2.4 encapsulates the importance of the Reynolds number. If viscosity is high relative to the flow speed and size, the Reynolds number is low and the viscous term dominates. Hence the advection terms can be neglected and the equations become approximately linear. If the viscosity is low in respect to the flow speed and size, the Reynolds number is high, the advection term dominates and the equations cannot be linearised. It is this non-linearity that makes solutions of the Navier-Stokes equations so difficult to obtain. At low Reynolds number, flows take on a stable and laminar flow pattern i.e. instabilities are, for the most part, unnoticeable. However, as advection dominates, disturbances in the laminar flow become apparent. Small disturbances are actually part of any laminar flow, but if Re is large enough, these disturbances get amplified leading to greater instabilities in the flow, and ultimately its breakdown (i.e. behaviour becomes less predictable and more chaotic) and the onset of turbulence.

2.2 Some Basic Observations on Solutions to Laminar Flow

There is a huge body of work done on solving the Navier-Stokes equations at low Reynolds numbers (Happel and Brenner, 1965; Lamb, 1932; Oseen, 1910; Purcell, 1976). In this work however we are not primarily interested in low Reynolds flow, but it is useful to know some basic ideas on their solutions.

2.2.1 Stokes' Equations

As can be seen from the non-dimensional Navier-Stokes equations, if $Re \ll 1$ then the inertia forces are dominated by the viscous term,

$$\left| \frac{\partial u_i}{\partial t} \right| \sim \left| u_j \frac{\partial u_i}{\partial x_j} \right| \ll \frac{1}{Re} \frac{\partial^2 u_i}{\partial x_j \partial x_j}. \quad (2.5)$$

This observation allows the non-linear Navier-Stokes equations to be simplified to a steady-state linear set of equations, known as the ‘‘Stokes’ equations’’ and can be expressed as

$$\frac{\partial p}{\partial x_i} = \frac{1}{Re} \frac{\partial^2 u_i}{\partial x_j \partial x_j} \quad (2.6)$$

$$\frac{\partial u_i}{\partial x_i} = 0. \quad (2.7)$$

Taking the divergence of both sides of the equation and invoking the incompressibility condition we see that equations 2.6 - 2.7 give rise to a simple Laplace equation for the pressure field,

$$\frac{\partial^2 p}{\partial x_i \partial x_i} = 0, \quad (2.8)$$

which is a starting point to generate solutions.

2.2.2 General Solutions for Laplace’s Equation

Reverting to vector notation, the simplest solution of Laplace’s equation , $\nabla^2 p = 0$, is of the functional form $p = \frac{1}{r}$ where r is a radial component. Using this as a starting point it is easy to generate more general solutions in form

$$p_n = \frac{\partial^n}{\partial x_i \partial x_j \dots} \left(\frac{1}{r} \right), n = 0, 1, 2, \dots \quad (2.9)$$

as the Laplace operator is commutative with differentiation e.g.

$$\nabla^2 \frac{\partial^n}{\partial x_i \partial x_j \dots} \left(\frac{1}{r} \right) = \frac{\partial^n}{\partial x_i \partial x_j \dots} \nabla^2 \left(\frac{1}{r} \right) = 0.$$

These solutions are known as spherical solid harmonics. From now on it will be useful to consider solutions to Laplace’s equation in standard spherical co-ordinates (r, θ, ϕ) .

An observation that can be made from the solution p_n in equation 2.9 is that

$$r^{n+1} \frac{\partial^n}{\partial x_i \partial x_j \dots} \left(\frac{1}{r} \right) = S_n(\theta, \phi),$$

where S_n is known as a surface harmonic of order n (Jeffreys and Jeffreys, 1956). So we write

$$p_n = \frac{1}{r^{n+1}} S_n(\theta, \phi), n = 0, 1, 2, \dots \quad (2.10)$$

However this solution only takes into account non-negative n . Consider the function $q_n = r^n S_n(\theta, \phi)$. Substituting this into Laplace's equation gives

$$\begin{aligned} \nabla^2 q_n &= \nabla^2 [r^n S_n] = \\ & S_n \frac{1}{r^2} \frac{\partial}{\partial r} \left(r^2 \left(\frac{\partial r^n}{\partial r} \right) \right) + r^n \left[\frac{1}{r^2 \sin \theta} \frac{\partial}{\partial \theta} \left(\sin \theta \frac{\partial S_n}{\partial \theta} \right) + \frac{1}{r^2 \sin^2 \theta} \frac{\partial^2 S_n}{\partial \phi^2} \right]. \end{aligned}$$

Using the fact that $\nabla^2 p_n = \nabla^2 \left[\frac{1}{r^{n+1}} S_n \right] = 0$ it follows that

$$\nabla^2 q_n = S_n n(n+1)r^{n-2} - S_n n(n+1)r^{n-2} = 0 \text{ for } n = 0, 1, 2, \dots$$

So this means we have two fundamental solutions to Laplace's equation in 3-dimensions, $p_n = \frac{1}{r^{n+1}} S_n$ for $n = 0, 1, 2, \dots$ and $p_n = r^n S_n$ for $n = 0, 1, 2, \dots$. More compactly these can be written as

$$p_n = \begin{cases} r^n S_n & \text{for } n \geq 0, n \in \mathbb{Z}, \\ r^n S_{-n-1} & \text{for } n < 0, n \in \mathbb{Z}. \end{cases} \quad (2.11)$$

All solutions to Laplace's equation can be written as a linear combination of these solutions based on surface harmonics and so

$$p = \sum_{-\infty}^{\infty} c_n p_n, \quad (2.12)$$

where c_n depends on the boundary conditions which are imposed on the system. Analytical solutions of the flow can be derived using equations 2.6 and 2.53, however, details will not be given in this work (see Lamb (1932) or Happel and Brenner (1965) for details).

If Re is large, so that the non-linear term cannot be ignored, then one must con-

sider the full Navier-Stokes equations without any simplifications. This is the situation that pertains for turbulent flows. As our biological population dynamics takes place in a turbulent boundary layer, the solution characteristics of the resulting flows are those that directly impact on this study.

The study of turbulence presents vastly different problems, as the equations cannot be simplified in this way and as of yet, no analytical solutions of the full Navier-Stokes equations exist. This inevitably leads to numerical simulation of the equations, which is computationally expensive and much of the modern advances in understanding the characteristics of turbulent flows is due to the increases in processor speed.

2.3 Characteristics of Turbulent Dynamics

2.3.1 Eddies

In a laminar flow as described in section 2.2, the environment is relatively quiescent. However in turbulence, small scale perturbations and instabilities are common throughout the flow. These instabilities allow individual fluid particles to travel in the opposite direction to the main current on many scales, permitting vortical motions in a range of sizes. This type of motion is very common in a turbulent flow and is known as an eddy. The architecture of an eddy however is not so easy to define,

It is as if we fear that, as soon as we try to define an eddy, the entire concept will melt away.

Peter Davidson, 2004

In general though an eddy is loosely defined as a region of vorticity acting as an overturning process in a fluid (Davidson, 2004). It can be thought of as a disturbance in ‘wavenumber space’, which will be analysed in greater detail in a subsequent section. This process acts as a catalyst towards the strong mixing behaviour of turbulence.

In a fluid subjected to wind forcing (i.e. a flow with wind acting on the surface of the fluid) large eddies are generated due to the shear stress acting. This large vortical motion can potentially act down to scales of about 10 – 100 metres below the surface (Carton et al., 2008), creating a region of eddy mixing known as the mixed layer. This large vortical motion sets up a slightly smaller eddy inside itself, which in turn, generates even smaller eddies etc. This ‘eddy cascade’ process carries on until the size of the eddies reaches a scale where viscous damping forces start to exceed the inertial driving forces (i.e. $Re = 1$ on these scales). At which point the eddy cascade process ceases and the small eddies are dampened out before they can become established.

Big whirls have little whirls, That feed on their velocity; And little whirls
have lesser whirls, And so on to viscosity.

Lewis Richardson, 1920

In reality this is a crude summary of what is actually a very complicated process, however a relatively simple formulation of these ideas was postulated by Kolmogorov (1941), which describes the energy transfer process of this eddy cascade.

2.3.2 The Kolmogorov Microscales

In a turbulent flow, different processes dominate on different scales. On the largest scales advection is the prevalent physical process, where the driving force and the scale of motion are the parameters which are most important, whereas on the smaller scales, the parameters which determine how the flow will act are viscosity and how much energy is dissipated via heat. Kolmogorov (1941) used this assertion to determine the small scales of turbulence, otherwise known as the Kolmogorov microscales. Through dimensional analysis it can be shown that length, time and velocity scales, based solely on the parameters which govern the small scale motions, can be defined as,

$$\eta_K = \left(\frac{\nu^3}{\epsilon} \right)^{\frac{1}{4}},$$

$$\tau_K = \left(\frac{\nu}{\epsilon} \right)^{\frac{1}{2}},$$

$$v_K = (\nu\epsilon)^{\frac{1}{4}},$$

where η_K - Kolmogorov length scale, τ_K - Kolmogorov time scale, v_K - Kolmogorov velocity scale, ν - kinematic viscosity, ϵ - net energy dissipation rate. Note that these scales are not independent of each other.

As such, these scales have not been derived through first principles but give a reasonable indication of the scales at which a particular flow acts down to. For example if a flow in water had a particular turbulent characteristic parameter set $(\nu, \epsilon) = (10^{-6} \text{ m}^2\text{s}^{-1}, 10^{-6} \text{ m}^2\text{s}^{-3})$, then it would have a η_K value of 1mm. That is the turbulent flow can not act on scales below 1mm and analogously any eddy cascade that is set up will not be able to sustain vortical motions below this scale. This means organisms smaller than 1mm would experience a quiescent life protected from turbulence in a Kolmogorov length scale sized bubble.

2.3.3 Spectral Dynamics and the Eddy Cascade

In this section we will discuss how energy is transferred from large scales to small scales. Through the efforts of Richardson and Kolmogorov it was found that the kinetic energy exchange, through an intermediate portion of length scales connecting the large scales and the small scales (the inertial subrange), displays universal properties which was a discovery of some magnitude (Kolmogorov, 1941; Richardson, 1921),

The first assumption to be made is that turbulence is homogeneous, that is the turbulent characteristics of the flow do not vary in space. To have an idea of how turbulence effects the flow we take a velocity measure at two different points in space and establish the degree of correlation between them when the separation is increased. This correlation tensor takes the form

$$R_{ij}(\mathbf{r}) = \langle u_i(\mathbf{x}, t)u_j(\mathbf{x} + \mathbf{r}, t) \rangle \quad (2.13)$$

Note that R_{ij} is a function of \mathbf{r} only, as the flow is assumed to be homogeneous. It turns out that in order to express the universal behavior of the inertial subrange, it is more convenient to study the situation in wave-number space. To do this we define the spectrum tensor as the Fourier transform of the correlation tensor,

$$\phi_{ij}(\mathbf{k}) = \frac{1}{(2\pi)^3} \int \int \int e^{-i\mathbf{k}\cdot\mathbf{r}} R_{ij}(\mathbf{r}) d\mathbf{r}, \quad (2.14)$$

and the inverse Fourier transform is defined as

$$R_{ij}(\mathbf{r}) = \int \int \int e^{i\mathbf{k}\cdot\mathbf{r}} \phi_{ij}(\mathbf{k}) d\mathbf{k}. \quad (2.15)$$

One of the most important statistics taken from the spectrum tensor is

$$\phi_{ii}(\mathbf{k}) = \phi_{11}(\mathbf{k}) + \phi_{22}(\mathbf{k}) + \phi_{33}(\mathbf{k}) \quad (2.16)$$

as it is proportional to the kinetic energy of the flow at a given wave-number. This is apparent as

$$\int_{\mathbf{k}} \phi_{ii}(\mathbf{k}) d\mathbf{k} = R_{ii}(0) = \langle u_1^2 \rangle + \langle u_2^2 \rangle + \langle u_3^2 \rangle = 3u^2. \quad (2.17)$$

If we assume u_1 , u_2 and u_3 are of the same order of magnitude (this implies the turbulence to be isotropic which is a good approximation at small scales, one of the universal properties of turbulence), we can integrate ϕ_{ii} over a spherical shell in wave-number space, so that $d\mathbf{k} = k^2 \sin\theta_{\mathbf{k}} d\phi_{\mathbf{k}} d\theta_{\mathbf{k}}$, and prescribe

$$E(k) = \frac{1}{2} \int_0^\pi \int_0^{2\pi} \phi_{ii}(\mathbf{k}) k^2 \sin\theta_{\mathbf{k}} d\phi_{\mathbf{k}} d\theta_{\mathbf{k}}, \quad (2.18)$$

where $E(k)$ is the turbulent kinetic energy spectrum, which gives an estimate of the amount of energy associated with an eddy of wave-number between k and $k + \delta k$. So to find the total kinetic energy of the system we simply integrate over all wave-numbers,

$$\int_0^\infty E(k) dk = \frac{1}{2} \langle u_i u_i \rangle = \frac{3}{2} u^2. \quad (2.19)$$

We can examine some simple cases of $E(k)$ by considering experimental results for 1-dimensional correlations, for example $R_{11}(r, 0, 0)$ and $R_{22}(r, 0, 0)$ which are known as the longitudinal and transverse correlations respectively. They are defined as

$$R_{11}(r, 0, 0) = \int e^{i\mathbf{k}_1 \cdot \mathbf{r}} F_{11}(k_1) dk_1 \quad (2.20)$$

$$R_{22}(r, 0, 0) = \int e^{i\mathbf{k}_1 \cdot \mathbf{r}} F_{22}(k_1) dk_1, \quad (2.21)$$

where F_{11} and F_{22} are the longitudinal spectrum and transverse spectrum respectively. As discussed in Tennekes and Lumley (1972), R_{11} is positive for all r , which implies that F_{11} has a maximum at the origin and is symmetric around $k = 0$ as R_{11} is real. By contrast R_{22} usually becomes negative at some large r . This implies that F_{22} is symmetric but with a peak away from the origin $k = 0$.

It can be shown that if the flow is homogeneous and isotropic then the following relationships can be derived for $E(k)$, $F_{11}(k)$ and $F_{22}(k)$ (Batchelor, 1953; Hinze, 1959).

$$E(k) = k^3 \frac{d}{dk} \left(\frac{1}{k} \frac{dF_{11}}{dk} \right) \quad (2.22)$$

$$\frac{d}{dk} F_{22}(k) = -\frac{k}{2} \frac{d^2}{dk^2} F_{11}(k). \quad (2.23)$$

From inspecting the characteristics of R_{11} , we know that F_{11} is an even function with a maximum at the origin. Assuming $F_{11}(k)$ takes a power law form, this implies $F_{11} = A - Bk^2 + Ck^4 + \dots$ with A, B and C all positive. If we take F_{11} up to the quartic term, then $E(k) = 8Ck^4$ and hence $E(k) \propto k^4$ at small k values. Using this and equation 2.18 we find $\phi_{ii} \propto k^2$ near $k = 0$. However, this observation of $E(k) \propto k^4$ is rarely exhibited in practice, since at large scales the assumption of isotropy and homogeneity breaks down. Nevertheless this is a theoretical observation with regard to the behaviour of $E(k)$.

As we discussed in the previous section, an eddy is defined loosely as a disturbance in a discrete band of wave-numbers around the region k . We note that energy is transferred from the large scales to the small scales (although this is a simplified view). In fact small scale eddies transfer energy to the larger too. However, the overall the transfer from small to large is less than the transfer from large to small, so what we are interested in is the net transfer of energy from large eddies to small eddies.

The strain rate associated with an eddy of size k is given by

$$s(k) \sim \frac{U}{L} \quad (2.24)$$

where U - velocity scale, L - integral length scale.

We can also find a relationship between the strain rate and $E(k)$ as follows. By definition

$$\begin{aligned} U &\sim (kE(k))^{\frac{1}{2}}, \\ \Rightarrow s(k) &\sim \frac{k}{2\pi} [kE(k)]^{\frac{1}{2}}, \end{aligned}$$

where $L = \frac{2\pi}{\langle k \rangle}$. We can use this relation to find the strain rate around $k = 0$. As $E(\langle k \rangle) \sim k^4$, this gives

$$s(k) \sim k^{\frac{7}{2}}, \quad (2.25)$$

which tells us, initially at least, that the strain rate is increasing. Assuming this strain rate increase is valid for all k , we can introduce a time-scale T

$$T \sim \frac{1}{s(k)}. \quad (2.26)$$

We note that as the strain rate increases, T decreases. Kolmogorov termed this time scale as the ‘return to isotropy’. We can deduce then that smaller eddies ($k \rightarrow \infty$)

return to isotropy faster than large eddies ($k \rightarrow 0$) and so smaller eddies have a harder time creating anisotropy in the flow. This realisation clarifies the fact that large scale features exhibit distinct directional characteristics whereas small scale features tend to be isotropic in character.

2.3.4 $E(k)$ in the Inertial Subrange

It has been ascertained that large scales are anisotropic and small scales are isotropic. However, the intermediate region between these scales has not been discussed. This middle range is home to a set of mid-scale sized eddies who respond quickly to changes in the mean flow but are in an approximate isotropic equilibrium. In this range the eddies associated are not dependant on the boundary conditions governing the mean flow (wind speed etc), but will only depend upon the dissipation rate ϵ (the rate at which energy is converted into heat) and the viscosity of the fluid ν , that is $E = E(k, \epsilon, \nu)$ in this range. Using this we can form a non-dimensional quantity of the kinetic energy,

$$\frac{E(k)}{\nu^{\frac{5}{4}}\epsilon^{\frac{1}{4}}} = \frac{E(k)}{v_K^2\eta_K} = f(k\eta_K), \quad (2.27)$$

where η_K - Kolmogorov length scale, v_K - Kolmogorov velocity scale and f is an undetermined non-dimensional function of a non-dimensional parameter $k\eta_K$.

Now as the Reynolds number increases, ϵ increases and $\eta_K \rightarrow 0$, so that at high Reynolds numbers we require this scaling to hold as $k\eta_K \rightarrow 0$. At large scales, viscosity is unimportant, rather the key parameter is the mean strain rate $\langle s(k) \rangle \sim \frac{U}{L}$ which is instrumental in the production of the turbulent (small scale) kinetic energy via the term $\langle u'_i u'_j \rangle s_{ij}$ in the turbulent kinetic energy budget equation (see Tennekes and Lumley (1972) pg 63-64). By this reasoning, the parameters most associated with kinetic energy at large scales are $\langle s(k) \rangle$ and ϵ and so using dimensional arguments again, one would expect $\epsilon \sim \frac{U^3}{L}$. Using this result we can non-dimensionalise the

kinetic energy in terms of large scale processes, that is,

$$\frac{E(k)}{\epsilon^{\frac{3}{2}} \langle s(k) \rangle^{-\frac{5}{2}}} \sim \frac{E(k)}{U^2 L} = F(kL), \quad (2.28)$$

where F is another non-dimensional function, this time of a non-dimensional parameter kL . We also see that in an inviscid flow as $Re = \frac{UL}{\nu} \rightarrow \infty$ then $L \rightarrow \infty$ and so we require this scaling to hold as $kL \rightarrow \infty$. What Kolmogorov did was to use $Re \rightarrow \infty$ in such a way that both $k\eta_K \rightarrow 0$ and $kL \rightarrow \infty$ hold simultaneously,

$$k\eta_K = kL \left(\frac{\eta_K}{L} \right) = kL \left(\left(\frac{\nu^3}{\epsilon} \right)^{\frac{1}{4}} \frac{1}{L} \right) \sim kL \nu^{\frac{3}{4}} \left(\frac{L}{U^3} \right)^{\frac{1}{4}} \frac{1}{L} = kL \left(\frac{1}{Re} \right)^{\frac{3}{4}}.$$

Now suppose that $kL = Re^n$ so that when one takes the limit $Re \rightarrow \infty$, one is effectively taking the limit $kL \rightarrow \infty$ too. If $kL = Re^n$ then

$$k\eta_K = Re^{n-\frac{3}{4}} \quad (2.29)$$

so provided $n < \frac{3}{4}$, taking the limit $Re \rightarrow \infty$ is equivalent to taking $k\eta_K \rightarrow 0$, at the same time as taking the limit $kL \rightarrow \infty$.

Matching up the large scale and small scale expressions (equations 2.27 and 2.28) allows one to determine the unknown functional forms $f(k\eta_K)$ and $F(kL)$, i.e.

$$\begin{aligned} E(k) &= U^2 L F(kL) = v_K^2 \eta_K f(k\eta_K) \\ \Rightarrow \frac{U^2 L}{v_K^2 \eta_K} F(Re^n) &= f(Re^{n-\frac{3}{4}}) \end{aligned}$$

Using the definitions of v_K , η_K and $\epsilon \sim \frac{U^3}{L}$

$$\Rightarrow Re^{\frac{5}{4}} F(Re^n) = f(Re^{n-\frac{3}{4}}).$$

If we assume F and f possess (to first order) some ‘power law behaviour’, then $F(Re^n) = (Re^n)^a$ and $f(Re^{n-\frac{3}{4}}) = \left(Re^{n-\frac{3}{4}}\right)^b$ then

$$\begin{aligned}\frac{5}{4} + an &= b\left(n - \frac{3}{4}\right) \\ \Rightarrow \frac{5}{4} + \frac{3}{4}b &= n(b - a).\end{aligned}$$

For this equation to hold for all $n \in (0, \frac{3}{4})$, there is only one possibility, namely that $a = b = -\frac{5}{3}$. Hence $F(kL) \sim (kL)^{-\frac{5}{3}}$ and $f(k\eta_K) \sim (k\eta_K)^{-\frac{5}{3}}$ so that

$$E(k) \sim \frac{U^2}{L^{\frac{2}{3}}} k^{-\frac{5}{3}} \sim \epsilon^{\frac{2}{3}} k^{-\frac{5}{3}}$$

and hence

$$E(k) = \alpha \epsilon^{\frac{2}{3}} k^{-\frac{5}{3}} \tag{2.30}$$

where α - constant.

This remarkable prediction was made in the 1940’s, but it was only validated in the 1960’s thanks to many experimental measurements (Grant et al., 1962; Maurer et al., 1994). Its importance lies in its universality, the assumptions on which it lies applies for any turbulent flow of sufficiently large Re . The wave-number range for which this $-\frac{5}{3}$ law operates is called the inertial subrange, which is the middle ground between small and large scales.

The irony is that back in the 1920’s Richardson’s experiments with dispersion (Richardson, 1921) had hinted that clouds spread according to a simple scaling law equivalent to $E(k) \sim \epsilon^{\frac{2}{3}} k^{-\frac{5}{3}}$. However, Richardson failed to predict that this behaviour is universal to all turbulent flows, and consequently missed out one of the greatest discoveries in the physical sciences.

2.4 Langmuir Turbulence

An aspect which the Navier-Stokes equations do not capture is the result of wave actions set up on the surface of the boundary layer, first noted in detail by Langmuir (1938). This section sets out what influence wave actions have on the flow derived from the Navier-Stokes equations, and how they can be modified to give a more precise description of the fluid motion in a turbulent boundary layer.

2.4.1 Stokes Drift

In general, the geometry of the surface of the ocean is extremely complicated, and cannot be readily formalised in an equation. It depends on wind speed and direction, wave height, wave breaking plus a myriad of other factors, which are far too complicated to be incorporated into any formalism. However, if the wind speed is moderate, so that the sea surface conditions approximate a gentle swell, then it is possible to devise a simple model of at least the first order effects brought about by the ocean waves on the turbulent boundary layer (Phillips, 1977; Stokes, 1847). First, the sea surface is assumed to conform to a simple travelling sinusoidal wave in the direction of wind (in the x direction for convenience), which takes the form

$$\gamma(\mathbf{x}, t) = a \cos(kx - \sigma t), \quad (2.31)$$

where γ - position of the free surface, a - wave amplitude, k - wave-number and σ - wave frequency. These parameters are not independent as the wave frequency σ can be written in terms of the wave-number via the relationship $\sigma = \sqrt{gk}$, where g is the acceleration due to gravity.

Along with 2.31 an associated velocity potential ϕ needs to be found, for reasons that will become apparent. Assuming the flow is irrotational (i.e. $\nabla \times \mathbf{u} = 0$) and incompressible, the velocity field can be defined by $\mathbf{u} = \nabla\phi$, note ϕ is a scalar quantity. Using this fact and the incompressibility condition, Laplace's equation for ϕ i.e. $\nabla^2\phi = 0$ is

satisfied, which is useful as Laplace's equation has been studied in great detail due to its applications in a wide variety of application (see section 2.2.1).

As 2.31 applies for waves propagating in the x direction only, one can assume that the velocity potential is independent of y and hence $\phi = \phi(x, z, t) = c(t)a(x)b(z) = c(t)\phi_1(x, z)$, making the assumption that ϕ is separable. Substituting this expression for $\phi_1(x, z)$ into Laplace's equation (as ϕ_1 also satisfies Laplace equation, as the Laplace operator is a spatial operator only) one obtains two second order ODE's for $a(x)$ and $b(z)$ respectively, that is,

$$a''(x) + Ca(x) = 0$$

$$b''(z) - Cb(z) = 0$$

where C is an arbitrary constant. Each equation gives general solutions of the form

$$\begin{aligned} a(x) &= A\cos Cx + B\sin Cx \\ b(z) &= De^{-Cz} + Ee^{Cz}, \end{aligned} \tag{2.32}$$

where A, B, D and E are arbitrary constants. Assuming that 2.31 is representative of a deep water wave and that $b(z)$ is bounded for $z \rightarrow -\infty$, one can deduce $D = 0$. Also, by definition, the z component of the velocity field at the surface is given by

$$\left. \frac{\partial \phi}{\partial z} \right|_{z=0} = \frac{d\gamma}{dt} \approx \frac{\partial \gamma}{\partial t},$$

for linear approximation. This can be used to yield a unique solution of ϕ , namely

$$\phi = \frac{\sigma a}{k} e^{kz} \sin(kx - \sigma t). \tag{2.33}$$

One is interested in seeing how a fluid particle near the surface is affected by the wave motions brought about by 2.31 and 2.33. To describe the type of motion associated with surface wave geometry, a Lagrangian framework is more appropriate, as we are interested in the effect on a particular particle. A Lagrangian framework follows an

individual particle pathway throughout the flow rather than analysing what the local velocity is at a fixed frame of reference at one particular point in space. A Lagrangian co-ordinate is therefore defined as a function of some fixed starting point in space and in time, e.g.

$$\zeta = \zeta(\mathbf{a}, t)$$

where ζ is the position of the fluid particle starting at position $\mathbf{a} = \zeta(\mathbf{a}, t_0)$, for example. This leads to an equivalence between Lagrangian and Eulerian co-ordinate frameworks, specifically

$$\mathbf{x} = \mathbf{a} + \int_0^t \mathbf{u}_L(\mathbf{a}, t') dt', \quad (2.34)$$

where \mathbf{u}_L is the Lagrangian velocity component and is defined as

$$\mathbf{u}_L(\mathbf{a}, t) = \frac{\partial \zeta(\mathbf{a}, t)}{\partial t}. \quad (2.35)$$

By definition, the Lagrangian velocity component $\mathbf{u}_L(\mathbf{a}, t)$ is equal to that of the Eulerian velocity component at the same point in space i.e.

$$\mathbf{u}_L(\mathbf{a}, t) = \mathbf{u}_E(\mathbf{x}, t)|_{\mathbf{x}=\zeta(\mathbf{a}, t)} \quad (2.36)$$

and hence

$$\mathbf{u}_L(\mathbf{a}, t) = \mathbf{u}_E(\mathbf{a} + \int_0^t \mathbf{u}_L(\mathbf{a}, t') dt', t). \quad (2.37)$$

This form is convenient as by using the Taylor expansion on the right hand side, we can find the differences between the Lagrangian and Eulerian velocity fields, e.g.

$$\begin{aligned} \mathbf{u}_L(\mathbf{a}, t) &= \\ &= \mathbf{u}_E(\mathbf{a} + \int_0^t \mathbf{u}_L(\mathbf{a}, t') dt', t) = \\ &= \mathbf{u}_E(\mathbf{a}, t) + \left(\int_0^t \mathbf{u}_L(\mathbf{a}, t') dt' \right) \cdot \nabla_{\mathbf{a}} \mathbf{u}_E(\mathbf{a}, t) + \text{h.o.t.} \end{aligned} \quad (2.38)$$

This relationship shows the divergence of the Eulerian and Lagrangian velocity components as time increases. This difference, to second order, is known as the Stokes drift named after it's discoverer and fundamentally changes the velocity field description. Linearising the integral in the Stokes drift term we reach a form that can be analytically formulated i.e.

$$\mathbf{U}_s = (u_s, v_s, w_s) = \left(\int_0^t \mathbf{u}_E(\mathbf{a}, t') dt' \right) \cdot \nabla_{\mathbf{a}} \mathbf{u}_E(\mathbf{a}, t) \quad (2.39)$$

where \mathbf{U}_s is the Stokes drift vector and u_s, v_s and w_s are the associated components. All that is left to do is formulate the Stokes drift into an analytical function based on the results detailed so far. Firstly, we can write

$$\mathbf{u}_E(\mathbf{a}, t) = \nabla \phi(\mathbf{x}, t)|_{\mathbf{x}=\mathbf{a}} = \sigma a e^{kz_0} \begin{pmatrix} \cos(kx_0 - \sigma t) \\ 0 \\ \sin(kx_0 - \sigma t) \end{pmatrix}, \quad (2.40)$$

where $\mathbf{a} = (x_0, y_0, z_0)$. Calculating each Stokes drift component separately, we find

$$\mathbf{U}_s = \left[a e^{kz_0} \begin{pmatrix} -\sin(kx_0 - \sigma t) + \sin(kx_0) \\ 0 \\ \cos(kx_0 - \sigma t) - \cos(kx_0) \end{pmatrix} \right] \cdot \left[a \sigma k e^{kz_0} \begin{pmatrix} -\sin(kx_0 - \sigma t) \\ 0 \\ \cos(kx_0 - \sigma t) \end{pmatrix} \right] \quad (2.41)$$

which, in component form gives

$$u_s = a^2 \sigma k e^{2kz_0} (1 - \cos(\sigma t)), \quad (2.42)$$

$v_s = 0$ and in a similar way we deduce

$$w_s = a^2 \sigma k e^{2kz_0} (\sin(\sigma t)). \quad (2.43)$$

This gives the local drift velocity to first order, however, we are only interested in the overall effect on a global frame and so the time averaged quantities are more appropriate. As $\overline{\cos(\sigma t)} = \overline{\sin(\sigma t)} = 0$, we are left with

$$\bar{\mathbf{U}}_s = (a^2 \sigma k e^{2kz_0}, 0, 0) = (U_s e^{2kz_0}, 0, 0) \quad (2.44)$$

where U_s is the Stokes drift magnitude.

This drift effect not only has a non-uniform impact on particles in the flow, but it also has an overturning effect on particle paths, which can be readily seen in figure 2.1. It is evident that the particles have a greater net drift over the time period nearer

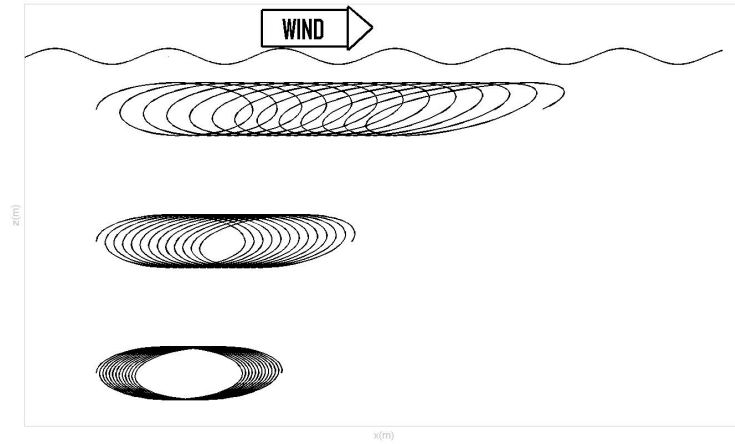


Figure 2.1: A schematic of three particle paths starting at 3 different depths when the boundary layer experiences surface waves. Surface water waves are propagating in the direction of wind, shown by the arrow.

to the surface. This has a tilting effect on vortices which are vertical in the boundary layer, overturning them to become horizontal.

The problem in calculating the Navier-Stokes equations with a propagating surface wave built in lies in the numerics. It would involve an extremely fine resolution grid at

the surface and would also need to be spatially dynamic, to include surface oscillations. The cost of this numerical set-up is of many orders of magnitude larger than the set-up without surface waves and just infeasible for simulation time particularly in biological time scales. However, it is possible to incorporate the average effects encapsulated by equation 2.44 into a fixed rectangular spatial domain.

2.4.2 Craik-Leibovich Equations

Craik and Leibovich (1976) were able to show that for a deep water wave (given above) a resulting coupling of the ‘Stokes drift’ term ‘ U_{s_i} ’ and the vertical vorticity ‘ ω_j ’ occurs into what is known as a vortex force term. This leads to a modified version of the Navier-Stokes equations which includes wave action, particularly applicable for oceanic boundary layer flows. These equations are called the Craik-Liebovich equations. This means that vertical eddies are tilted and intensified in the direction (horizontally) perpendicular to the wave front propagation. The Craik-Leibovich equations are defined as

$$\frac{\partial u_i}{\partial t} + u_j \frac{\partial u_i}{\partial x_j} + \epsilon_{ij3} f (u_i + U_{s_i}) = -\frac{1}{\rho} \frac{\partial p}{\partial x_i} + \nu \frac{\partial^2 u_i}{\partial x_j \partial x_j} + \epsilon_{ijk} U_{s_i} \omega_j + F_i \quad (2.45)$$

where

$$\epsilon_{ijk} = \begin{cases} 1 & \text{if } (i, j, k) = (1, 2, 3), (3, 1, 2), (2, 3, 1) \\ -1 & \text{if } (i, j, k) = (1, 3, 2), (3, 2, 1), (2, 1, 3) \\ 0 & \text{or if } i = j, j = k \text{ or } i = k, \end{cases}$$

and f is the Coriolis frequency. The cross product involving f describes planetary vorticity. $f = 10^{-4} \text{s}^{-1}$ will be used for all simulations in this work, which corresponds to a latitude of 45 degrees north (a mid-latitude in the northern hemisphere).

This coupling of the vorticity, ω , and the Stokes drift creates a series of counter-rotating vortices below the surface of the wave front, these are known as ‘Langmuir circulations’. This can advect nutrient rich water from the deep ocean into the euphotic zone of the water column. On the surface these ‘Langmuir cells’ manifest themselves in a series of

windrows parallel to the direction of the wave propagation. These equations also take into account the contribution of flow due to planetary rotation (the Coriolis force). A curious behaviour of the flow field is that, due to planetary rotation, a depth dependant directional mean flow is observed which is at an angle to the direction of wind, known as Ekman transport (Ekman, 1905). This angle is dependent on both depth and latitude and in this work; it will also be dependent upon the magnitude of the Stokes drift (Lewis and Belcher, 2004). This deflection of flow can be observed in the wind rows shown in section 2.4.3 where, without the Coriolis effect, the passive tracers would simply go in the direction of wind, without any angular deflection. The influence this has on plankton aggregations is not at all clear, so it will not be considered, but the distribution of plankton concentrations will certainly be effected.

In the physical-biological model implemented in this work (see later), I will use the Craik-Leibovich equations to generate the turbulent boundary layer flows in which my biological investigations will take place.

2.4.3 Consequences of Langmuir Turbulence

In many models, such as popular weather prediction models (e.g. Lean et al. (2008)), wave effects are not taken into account. We will explore the significance of the extra vortex term in the Craik-Liebovich equations and how this effects boundary layer simulations.

Wind rows

As was discussed, the motivation behind developing a model for the incorporation of wave effects, was the observation that debris in the ocean collects in convergent zones, perpendicular to the direction of wave propagation (Langmuir, 1938). These are known as ‘wind rows’. This behaviour was tested in simulations when wave effects were present and when they were not. We released a number of particles at the surface and noted the dynamics, see figure 2.2. Figure 2.2(a) shows that without any surface wave effects, all particles travel in the same directions and spread out very slightly.

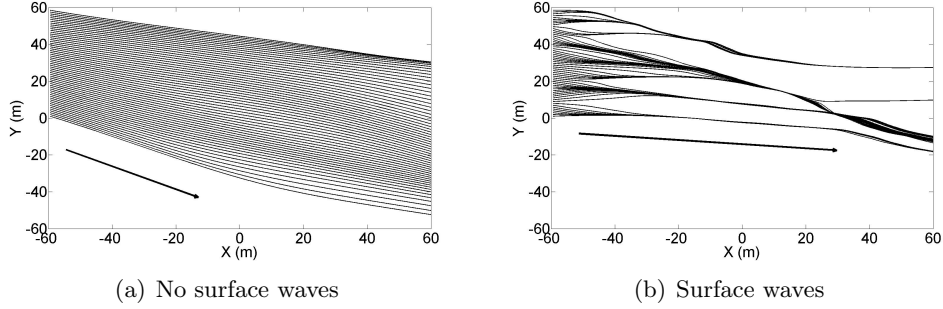


Figure 2.2: A set of 60 particle paths all starting at $X = -60$ m at different $y \in (0, 60)$. The direction the particles are travelling is indicated by the arrow.

However, the dynamics of the passive tracers change dramatically when subjected to wave forcing. As time goes on, we see a clustering of tracers (in convergent zones), see figure 2.2(b). This convergence behaviour should not be ignored, particularly when modelling such systems that include analysing the dynamics of spatial distributions, such as planktonic and nutrient concentrations.

Next, we need to quantify the amount of energy in the system and how wave forcing impacts upon this, as turbulent mixing is very important to the aim of this study.

Energy Dissipation Rate, ϵ

In a boundary layer, energy is usually lost through viscous effects and transferred to heat energy. This amount of energy that is lost in the system is indicative of the amount of energy in the system. The rate of energy lost to heat in the system is known as the energy dissipation rate and is a small scale process, comparable to that of the Kolmogorov length scale. This energy dissipation rate can be calculated via the (statistically stationary) mean turbulent kinetic energy budget given by Lewis (2005),

$$\epsilon = -\frac{\partial \langle \mathbf{u}'^2 w \rangle}{\partial z} - \langle \mathbf{u}' w \rangle \frac{\partial \mathbf{u}}{\partial z} - \frac{1}{\rho_0} \frac{\partial \langle p' w \rangle}{\partial z} - \langle u' w \rangle \frac{\partial u_s}{\partial z} \quad (2.46)$$

Figure 2.3 shows the differences in energy in the two boundary layers, particularly near the surface. This energy difference is staggering considering wave effects are usually neglected in a system and contribute vastly to the boundary layer. Although the energy dissipation rate (small scale) is much larger in a Stokes-Ekman boundary layer than the traditional Ekman boundary layer, it accounts for a smaller percentage of the total kinetic energy (small scale + large scale) in the system (McWilliams et al., 1997) and hence the Stokes-Ekman boundary layer is more accurate as large scale processes are solved exactly in the model setup in this work, details of which will be given in the next section.

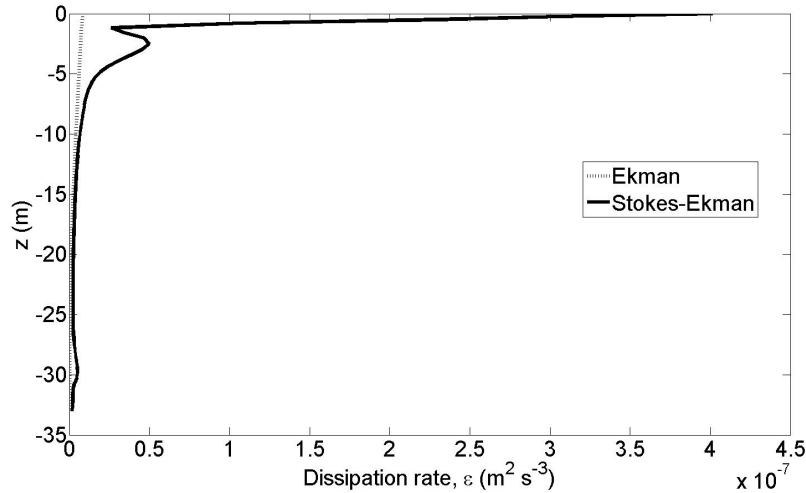


Figure 2.3: Profile of the energy dissipation rate for a boundary layer with surface water waves (Stokes-Ekman boundary layer), in the solid line, and a boundary layer without surface waves (Ekman boundary layer), in the dashed line. These two simulations were identical except for the Stokes drift value, $U_s = 0.067$ and $U_s = 0$ respectively.

2.5 Large Eddy Simulation (LES)

To compute such a complex set of equations (such as the Navier-Stokes equations) is obviously unfeasible due to the length scales involved (for reasons given in 2.5.1). So a method must be utilised that can resolve the main features of the flow, but be simple

enough to make simulations feasible. There are many techniques in the literature to do this, for example, a popular model is the $k - \epsilon$ turbulence model (Jones and Launder, 1972) which attempts to find solutions of a fully turbulent flow, which stems from the Reynolds-Averaged-Navier-Stokes equations (RANS), which are essentially a time averaged solution of the Navier-Stokes equations (Reynolds, 1895). However, turbulent flows are very transient and there are no steady state solutions in a turbulent flow. Therefore the model which will be utilised is one which will capture the dynamics of the large scale motions, whilst sacrificing the small scale motion. This method is known as large eddy simulation.

2.5.1 Resolution Scales

The Kolmogorov length scale $\eta_K = \left(\frac{\nu^3}{\epsilon}\right)^{\frac{1}{4}}$, gives an indication to what scale viscosity acts upon, i.e. the scale at which the Navier-Stokes equations become approximately linear. If we solved the Navier-Stokes equations numerically (using a finite difference scheme) and we had a very large amount of computing power, we would use this length scale as resolution for our solution grid. The energy dissipation rate ϵ is essentially a measure of how turbulent the fluid is; hence the higher the level of turbulence, the lower η_K will be and the finer the resolution scale of the solution grid needs to be.

In order to generate an exact solution of the Navier-Stokes (or Craik-Liebovich) equations as a manifestation of an oceanic boundary layer, one must first resolve the flow across all of its relevant constituent parts. The depth of an ocean boundary layer is usually of the size of tens to hundreds of metres. The corresponding large scales that drive the flow will be of a comparable size. Energy is then transferred by means of the ‘eddy cascade’ model describes in 2.3.3 down to the smallest Kolmogorov length scales where it is dissipated as heat. So to give a complete and reliable numerical solution to the Navier-Stokes (Craik-Liebovich) equations representative of an oceanic boundary layer, one must resolve down through a hierarchy of scales from say 10^2 metres down to 10^{-3} metres of the wave-number scale.

As an indication of the computing power needed to do just that, for a turbulent flow $\eta_K \sim 1 \times 10^{-3} \text{m}$ and for a 3 dimensional solution grid covering $100\text{m} \times 100\text{m} \times 30\text{m}$ we would need to make 3×10^{14} calculations, for just one moment in time, which is unfeasible even for the most powerful of computers. This highlights the most fundamental difficulty in solving the Navier-Stokes equations over domains roughly equivalent in size to an ocean boundary layer. Numerical approximations must therefore be made to account for this shortcoming to reduce the resolution scale but at the same time retaining the fundamental characteristics of a full boundary layer solution, which still allows us to predict the evolution of the ocean dynamics over biologically significant time periods.

2.5.2 Filtering

Large eddy simulation is an averaging technique used to permit a reasonable resolution to be used (Sagaut, 2000). The idea is that the flow ‘ \mathbf{u} ’ is split up into 2 parts, Large scale flow ‘ \mathbf{U} ’ and small scale flow ‘ \mathbf{u}' ’ (the same routine is implemented for the pressure term $p = P + p'$). For our model, we pick a grid spacing of approximately 1 m, so \mathbf{U} would account for the flow above 1 metre and \mathbf{u}' would account for the flow below this scale; this small scale is known as the sub-grid scale.

These substitutions are made into the Navier-Stokes equations to yield a mixture of resolved and unresolved differential terms,

$$\frac{\partial U_i}{\partial t} + U_j \frac{\partial U_i}{\partial x_j} = -\frac{1}{\rho} \frac{\partial P}{\partial x_i} + \nu \frac{\partial^2 U_i}{\partial x_j \partial x_j} + F + SGS \quad (2.47)$$

where

$$SGS = -\frac{\partial u'_i}{\partial t} - u'_j \frac{\partial u'_i}{\partial x_j} - \frac{1}{\rho} \frac{\partial p'}{\partial x_i} + \nu \frac{\partial^2 u'_i}{\partial x_j \partial x_j} \quad (2.48)$$

The LES method uses the assumption that linear small scale terms equate to zero (although this is not the case). More formally, we apply a Fourier transform to our

flow i.e.

$$\mathbf{u}(\mathbf{k}, t) = \int \mathbf{u}(\mathbf{x}, t) e^{i\mathbf{k}\cdot\mathbf{x}} d\mathbf{x}, \quad (2.49)$$

where k - wave-number.

A cut-off wave-number (k_c) is then introduced which is equivalent to $\frac{1}{L_0}$, where L_0 is the resolution of the solution grid. Using k_c the flow can be filtered to remove the small scale processes,

$$\overline{\mathbf{u}(\mathbf{x}, t)} = \begin{cases} \frac{1}{(2\pi)^3} \int \mathbf{u}(\mathbf{k}, t) e^{i\mathbf{k}\cdot\mathbf{x}} d\mathbf{k} & \text{if } k \leq k_c \\ 0 & \text{otherwise.} \end{cases} \quad (2.50)$$

Consequently, $\overline{u'} = 0$. This can be used to eliminate the linear terms in the sub-grid scale. However this technique can not be used for the non-linear small SGS advection term and a parametrisation need to be employed.

2.5.3 Smagorinsky Scheme

The problem with solving the Navier-Stokes equations with regards to splitting the flow and filtering is we have an unresolved term left over,

$$\frac{\partial \overline{u_i u_j}}{\partial x_j}$$

which simply cannot be calculated directly or assumed to be negligible. The higher the spatial resolution is, the less of a problem this non-linear term becomes, however, the computer power at our disposal doesn't permit going to a fine resolution. This is known as the closure problem.

Large-Eddy simulation is a method which tries to 'close' this problem by modelling the non-linear sub-grid processes in terms of large scale processes (which can then be numerically solved). There are many ways which this has been attempted (Germano et al., 1991; Schumann, 1975; Yakhot and Orszag, 1985), but we will use the method

outlined in Smagorinsky (1963). Using dimensional arguments, Smagorinsky (1963) assumes that small scale advection can be modelled proportional to large scale diffusion, i.e.

$$\frac{\partial \overline{u_i u_j}}{\partial x_j} = -\nu_t(\mathbf{x}) \frac{\partial^2 U_i}{\partial x_j \partial x_j} \quad (2.51)$$

where ν_t is known as the eddy viscosity (due to its units). The problem is then calculating ν_t . It was postulated that ν_t should be a function of the amount of shear in the flow and the size of the largest eddies as these govern how much work is being done in the flow. The following relationship was put forward (again from dimensional arguments),

$$\nu_t(\mathbf{x}) = CL^2 \sqrt{\frac{S_{ij} S_{ij}}{2}}, \quad (2.52)$$

where $C = O(1)$ constant, L is the size (depth) of the boundary layer and $S_{ij} = \frac{1}{2} \left(\frac{\partial U_i}{\partial x_j} + \frac{\partial U_j}{\partial x_i} \right)$ is the rate of strain (which is a measure of shear of the resolved flow). Then it is a matter of choosing appropriate values of L and C to satisfy surface boundary conditions (Sullivan et al., 1994).

2.5.4 Numerical Techniques

The difficulty in solving the Navier-Stokes equations is finding the pressure term. In this model, we take the divergence of the Navier-Stokes equations (similar to that of section 2.2.1) and solve the Poisson equation for pressure, i.e.

$$\frac{\partial^2 p}{\partial x_i \partial x_i} = \frac{\partial S_u}{\partial x_i} \quad (2.53)$$

where S_u comprises the velocity dependant terms in the Navier-Stokes equations. Then a Fourier transform is taken to simplify the problem. However the Fourier transform will only be taken in the lateral domain due to the depth grid points being non-uniform. We then define the pressure term to be

$$p = \int_0^\infty \int_0^\infty e^{i(k_x x + k_y y)} \tilde{p} dk_x dk_y \quad (2.54)$$

where \tilde{p} is the Fourier transform of p . Then taking the Fourier transform of equation 2.53, one yields the equation

$$\frac{d^2\tilde{p}(k_x, k_y, z)}{dz^2} - (k_x^2 + k_y^2)\tilde{p} = G(k_x, k_y, z) \quad (2.55)$$

where G is the (known) Fourier transform of the right hand side of equation 2.53. Then discretising the z second derivative in equation 2.55, e.g.

$$\frac{d^2p(k_x, k_y, z)}{dz^2} = \frac{\tilde{p}(k_x, k_y, z + \delta z) - 2\tilde{p}(k_x, k_y, z_n) + \tilde{p}(k_x, k_y, z - \delta z)}{\delta z^2} \quad (2.56)$$

one can pose the solution of $\tilde{p}(k_x, k_y, z)$ as an inverse problem in the form

$$\begin{pmatrix} \frac{-2}{\delta z^2} - k_x^2 - k_y^2 & \frac{1}{\delta z^2} & 0 & \dots & 0 \\ \frac{1}{\delta z^2} & \frac{-2}{\delta z^2} - k_x^2 - k_y^2 & \frac{1}{\delta z^2} & \dots & 0 \\ 0 & \ddots & \ddots & \ddots & 0 \\ 0 & 0 & \dots & \frac{1}{\delta z^2} & \frac{-2}{\delta z^2} - k_x^2 - k_y^2 \end{pmatrix} \begin{pmatrix} \tilde{p}(z_0) \\ \tilde{p}(z_1) \\ \vdots \\ \tilde{p}(z_n) \end{pmatrix} = G. \quad (2.57)$$

It is then a straight forward case of finding the pressure term by taking an inverse Fourier transform of $\tilde{p}(k_x, k_y, z)$. Now that both the velocity field and the pressure field are both known, we can advect forward in time using the discretisation of the time derivative

$$\frac{\partial \mathbf{U}}{\partial t} = \frac{\mathbf{U}(x, y, z, t + \delta t) - \mathbf{U}(x, y, z, t)}{\delta t}. \quad (2.58)$$

It is now left to define the dynamic time-step δt . The dynamic time-step is prescribed to be smaller if a more turbulent flow is detected and vice versa. This is to give more accuracy, as this is needed with higher turbulence levels as the Kolmogorov length scale is smaller. This is defined by

$$dt = \left(\sqrt{\left| \frac{u}{\delta x} \right|^2 + \left| \frac{v}{\delta y} \right|^2 + \left| \frac{w}{\delta z} \right|^2} + \frac{2\nu}{\delta x^2 + \delta y^2 + \delta z^2} \right)^{-1} \quad (2.59)$$

where the first term (the $\sqrt{\quad}$ term) characterises the level of advection and the second term characterises the level of diffusion. If the magnitude of the velocity field is large, then the time-step will decrease to account for the unpredictability inherent with a flow that is more turbulent. Also, if the grid spacing is too large then this will have the same effect as solutions are less reliable for a larger grid spacing. In other words, the more unpredictable the solutions are, the finer the time resolution will be to account for this.

2.6 Boundary Conditions

The main driving force of our boundary layer is a wind blowing over the surface of the water. This is characterised by a shear force at the surface,

$$\nu_t \frac{\partial u}{\partial z} \Big|_{z=0} = \frac{\tau}{\rho_w} = U_*^2 \quad (2.60)$$

where τ is the wind stress, ρ_w is the density of water and U_* is the friction velocity. This friction velocity is an important parameter as it is related directly to the wind speed above the surface. It enables us to prescribe the level of turbulence in a particular simulation. The shear force which this friction velocity produces gives rise to an overturning eddy motion and is one possible mechanism behind plankton aggregation (Birch et al., 2008).

Periodic lateral boundary conditions were imposed on the solution grid. These can be given in the form

$$\begin{aligned} u(x_{\min}, y, z) &= u(x_{\max}, y, z) \\ u(x, y_{\min}, z) &= u(x, y_{\max}, z). \end{aligned} \quad (2.61)$$

The solution grid was set up to have dimensions $x \times y \times z = 120\text{m} \times 120\text{m} \times 33\text{m}$ and resolutions $\delta x = 3\text{m}$, $\delta y = 3\text{m}$ $\delta z = 0.45\text{m}$ although the z grid spacing is staggered so that there is more resolution at the surface, as this where turbulence is the most abundant. With this choice of grid size and spacing, we can achieve solutions on biological

time scales (weeks) and also maintain reasonable accuracy.

Now that the flow field has been set up, it will be fed into a biological model which will govern the dynamics of plankton in a realistic flow field. The main interest in this work is the levels of turbulence and how they effect planktonic aggregations. Therefore, with regards to the physical model, the wind stress will be the key component in analysing plankton formations as this is a measure for the amount of energy which is being pumped into the system.

Chapter 3

The Biological Model

3.1 The Nutrient-Phytoplankton-Zooplankton (NPZ) Model

The NPZ model I will utilise is a three component ODE model given in the form

$$\frac{d\Gamma_i}{dt} = f_i(\Gamma_1, \Gamma_2, \Gamma_3, \dots, \Gamma_i; \mathbf{x}, t)\Gamma_i, \quad i = 1, 2, 3 \quad (3.1)$$

where $\Gamma_1 = N$ is the nutrient, $\Gamma_2 = P$ is the phytoplankton, $\Gamma_3 = Z$ is the zooplankton and f_i is an arbitrary function depending on the state, spatial and time variables. This is a subset of a more general set of equations for $i = 1 \dots N$ components known as the Kolmogorov system (Kolmogorov, 1936; Cropp and Norbury, 2009). More qualitatively, the NPZ model will take the form

$$\begin{aligned} \frac{dN}{dt} &= \text{'N recycled from P'} - \text{'N uptake by P'} \\ \frac{dP}{dt} &= \text{'P growth from N'} - \text{'P grazing loss from Z'} \end{aligned} \quad (3.2)$$

$$\frac{dZ}{dt} = \text{'Z growth from P'} - \text{'Z death'}$$

This model is the most popular for studying the complex dynamics of planktonic populations and is used in a variety of forms, from the simple three component model

stated in equation 3.1 (Steele and Henderson, 1981; Franks et al., 1986; Roy et al., 2012), to many compartments (Baird and Emsley, 1999; Banas et al., 2009). This encourages the question, how simple is too simple? Most parameters that are added to a model must be estimated either experimentally or probabilistically. Consequently each of these parameter values contain an associated error, which has the potential to influence the model's predictive capabilities. Incorporating too many such parameters will increase the range of the model's output to such an extent that its predictive capability is rendered essentially meaningless. So a compromise between complexity and generality must always be sought. The key is to identify the parameters which have a really significant impact on a model's output and thus should be modelled in detail, from those which are essentially neutral and can either be ignored, or their effects incorporated in a much simpler form.

Common choices of functional forms for f_i range from the simple linear e.g.

$$\frac{dP}{dt} = aPN - bPZ,$$

to more complicated forms, which for instance, can encapsulate saturation behaviour,

$$\frac{dP}{dt} = \frac{a}{c + N}P - \frac{bP}{\lambda + P}Z,$$

where a , b , c , λ are constant parameters (Franks, 2002).

A particular example where there are many elements to consider is the formulation of the zooplankton predation rate. For example, the spatial range and density levels of the prey, the foraging and capture capabilities of the predator, its perception capabilities plus external factors such as temperature, light levels and background turbulence. All these features can interact with one another to potentially produce an extremely complicated picture of this crucial parameter in the population dynamics. In this thesis, I shall try to encapsulate the effects of as many of these features as possible, whilst

at the same time attempting to keep the model's complexity down to an acceptable level.

This work is devoted to turbulence and so a parametrisation of the turbulent flow must also be included in the biological model, as the flow plays a major role in predation and nutrient uptake which will be discussed in more detail in a subsequent section. In this work the energy dissipation rate ϵ , a good measure which characterises how turbulent the flow is, will be employed (Fasham, 1993; Gaylord et al., 2013).

I will discuss the terms which I have chosen for the model and explain the reasoning behind each choice. I will also show how the flow calculated using the LES method can be incorporated into the NPZ model by means of an advection-diffusion system of equations.

The reasons behind the adoption of a mechanistic approach to finding model parameters over simply empirically fitting curves to experimental data, are rather subtle. Quantitatively both routes could arrive at the same outcome and give the same theoretical predictions. Qualitatively however, a mechanistic approach can give information about which biological characteristics affect the model and in what way. Arbitrarily changing curve fitting parameters can bring about the same results, but does not highlight the physical/biological basis of the findings. This is not to say finding estimates for overall parameters based on raw data alone is not important, indeed this methodology is vital in validating the mechanistic approach.

Of course the great advantage of choosing to parametrise a process probabilistically and/or experimentally is the ease of doing so. Curve fitting software packages are readily available and extremely easy to use and so even non-specialists can describe a particular process with no great difficulty. This can be extremely useful, especially to non-specialists (who don't have knowledge of how to manually implement a curve

fitting technique for instance), in particular when interest is only in what the process is doing, rather than why it is doing it.

However, the question being asked in this work is essentially, ‘which biological parameters are most conducive to the formation of planktonic patches?’ so logically a mechanised approach to parametrising the model is the most appropriate direction to take (if possible). The following sections will be devoted to deriving all the parameters necessary to describe the population dynamics of the generic phytoplankton and zooplankton species.

3.2 Derivations of the Biological Terms

When modelling, there are a number of different approaches one can take. A heuristic approach, where models are based on simple, intuitive functional forms, an empirical approach, where formulae are based on experimental data only, a semi-empirical approach, where formulae are based on combined theoretical and experimental results or mechanistic, where formulae are derived from theoretical considerations only (Baird and Emsley, 1999). It is logical then that if knowledge of the theoretical considerations is strong, then the latter is the best process to use.

As a side note, for the remainder of this section, we will be interested in the non-dimensional quantities

$$P = \frac{P^*}{P_0} \quad Z = \frac{Z^*}{Z_0} \quad N = \frac{N^*}{N_0} \quad (3.3)$$

where P , Z , N are non-dimensional quantities, P^* , Z^* , N^* are the actual concentration and P_0 , Z_0 , N_0 are reference concentrations (taken to be an average background concentration).

3.2.1 Nutrient Uptake by Phytoplankton

Phytoplankton have evolved to obtain sustenance from the many chemical compounds which reside in the ocean and seas. The main compounds which can be used as nutrients include phosphates, ammonia, iron and the most abundant chemical compound, nitrate. On top of this, dead phytoplankton cells also nourish the phytoplankton population (Li et al., 2013; Weber and Deutsch, 2010). Other chemicals are negligible in comparison and so this group of compounds is usually the subject of nutrient modelling (Fasham et al., 1990). Following the work of Baird and Emsley (1999), the framework of this term will be based on a diffusive type model. Solutions can

Formulation

Solutions to the following can be found in many texts, e.g. Crank (1979). To derive the formula for nutrient uptake, one must first examine the process of nutrient absorption by a typical phytoplankton cell in some detail in order to formulate a general mechanism. For simplicity, it is assumed the phytoplankton is a spherical cell, of radius R_p , residing in a large volume V of solute. In this situation the absorption process is primarily driven by diffusion, that is, nutrients outside of the cell wall will diffuse into the cell in a similar process to that of osmosis (a process that will cease when the cell is ‘full’).

The ambient concentration of nutrients outside the cell, N , assuming there is no fluid flow, is governed by a simple diffusion equation of the form

$$\frac{\partial N}{\partial t} = D_N \nabla^2 N, \quad (3.4)$$

where D_N is the diffusion coefficient.

Let us assume that nutrient solute is absorbed into the phytoplankton cell at a rate of Q particles per unit time, so the cell acts as a ‘sink’ of the surrounding solute. Suppose the system is in dynamic equilibrium, i.e. at a steady state where $\frac{\partial N}{\partial t} = 0$. In this case

the system satisfies the following equations:

$$D_N \nabla^2 N = 0, \quad (3.5)$$

if the volume does not contain the cell and

$$D_N \nabla^2 N = \delta(\mathbf{r}), \quad (3.6)$$

if the volume in question encompasses the cell. It is assumed that the cell is centred at the origin $\mathbf{r} = 0$ and

$$\delta(\mathbf{r}) = \begin{cases} \infty & |\mathbf{r}| = R_P, \\ 0 & |\mathbf{r}| \neq R_P. \end{cases} \quad (3.7)$$

Equations 3.5 - 3.7 can also be written in the more compact form

$$\int \int \int_V \delta(\mathbf{r}) dV = \begin{cases} Q & \text{if volume contains cell,} \\ 0 & \text{otherwise.} \end{cases} \quad (3.8)$$

Firstly, taking equation 3.5 and assuming spherical symmetry leaves us with solving the relatively simple equation

$$\frac{d}{dr} \left(r^2 \frac{dN}{dr} \right) = 0,$$

which yields a general solution of the form

$$N = \frac{A}{r} + B,$$

where A and B are arbitrary constants to be determined. Assuming as $r \rightarrow \infty$, $N \rightarrow N_0$, where N_0 is the average ambient nutrient concentration, this gives

$$N = \frac{A}{r} + N_0.$$

Taking equation 3.6 and integrating it over a volume which encompasses the cell gives

$$D_N \int \int \int_V \nabla \cdot (\nabla N) dV = \int \int \int_V \delta(\mathbf{r}) dV = Q. \quad (3.9)$$

Now by the divergence theorem,

$$D_N \int \int \int_V \nabla \cdot (\nabla N) dV = \int \int_S (\nabla N) \cdot \mathbf{n} dS, \quad (3.10)$$

where \mathbf{n} is the outward normal directed from the surface S of the sphere. As $r \rightarrow R_p$

$$\nabla N = \left. \frac{d}{dr} \left(\frac{A}{r} + N_0 \right) \right|_{r=R_p} \mathbf{n} = -\frac{A}{R_p^2} \mathbf{n},$$

$$\mathbf{n} dS|_{r=R_p} \equiv R_p^2 \sin\theta d\theta d\phi,$$

and hence

$$\begin{aligned} D_N \int_0^\pi \int_0^{2\pi} \left(-\frac{A}{R_p^2} \right) R_p^2 \sin\theta d\theta d\phi &= Q, \\ \Rightarrow -4\pi D_N A &= Q, \\ \Rightarrow A &= -\frac{Q}{4\pi D_N}, \end{aligned}$$

and so the concentration of nutrients is given by

$$N = -\frac{Q}{4\pi D_N r} + N_0. \quad (3.11)$$

At the cell wall, when $r = R_p$, $N = N_W$, hence the flux Q at the cell wall becomes

$$Q = 4\pi R_p D_N (N_0 - N_W), \quad (3.12)$$

draining steadily into a spherical cell of radius R_p . (The case is studied in Baird and Emsley (1999) for the cases of other cell geometries.)

This result is too simple because it neglects the possibility that the solute fluid could

be in relative motion with respect to the cell wall. The effect of fluid motion outside the cell (brought about by turbulence or cell swimming) is to advect more solute into the vicinity of the cell wall and hence potentially increase the uptake rate. The details of how this comes about are very complicated (Batchelor, 1980), too complicated to be incorporated into an uptake model, which we propose to couple with an LES code. So instead, the effects of fluid motion on the uptake rate will be encapsulated by the relatively simple means of employing a ‘turbulent Sherwood number’ Sh . This non-dimensional number $Sh \geq 1$ is a measure of the ratio of the total nutrient flux into the cell in the presence of relative fluid motion, to the flux obtained through diffusion alone. Consequently the revised uptake rate in the presence of relative fluid motion is defined by

$$Q = 4\pi R_p D_N Sh (N_0 - N_W), \quad (3.13)$$

with $Sh = 1$ when there is no fluid motion.

The problem now is to determine the value of Sh from the boundary layer dynamics generated by the LES code. This can be done indirectly by first noting that typical values of Sh are themselves a function of another non-dimensional number, called the Peclet number, denoted by Pe . The Pe number measures the relative strength of advective transport to diffusive transport over a certain length scale, which we can denote by r . It is defined by

$$Pe = \frac{\text{advective transport}}{\text{diffusive transport}} = \frac{Ur}{D_N}. \quad (3.14)$$

Here U is a velocity scale characterising the relative speed of the fluid near the cell wall. In a turbulent flow, this depends upon the average value $\langle \epsilon \rangle$, the energy dissipation rate. In addition, in this application we are assuming that the phytoplankton cells are small, in particular, the cell radius $R_p < \eta_\kappa$. Under these assumptions, Karp-Boss et al. (1996), closely following Batchelor (1980), postulated that a suitable definition

for a turbulent Peclet number would be

$$Pe_t = \frac{R_p v_K}{D_N}, \quad (3.15)$$

where $v_K = \left(\frac{\langle \epsilon \rangle}{\nu}\right)^{\frac{1}{2}}$ is Kolmogorov velocity scale and R_p is the radius of the phytoplankton cell. In addition Karp-Boss et al. (1996) go on to postulate that the corresponding turbulent Sherwood number can be calculated from equation 3.15, via the following relations

$$Sh_{\text{turb}} = \begin{cases} 1 + 0.29Pe_{\text{turb}}^{\frac{1}{2}} & Pe_t \leq 0.01 \\ \frac{1}{2} \left[1.969 + 0.15Pe_{\text{turb}}^{\frac{1}{2}} + 0.344Pe_{\text{turb}}^{\frac{1}{3}} \right] & 0.01 < Pe_t < 100 \\ 0.55Pe_{\text{turb}}^{\frac{1}{3}} & Pe_t \geq 100. \end{cases} \quad (3.16)$$

So knowing $\langle \epsilon \rangle$ as we do from the LES boundary layer dynamics, it is possible to estimate Equation 3.16 using Equation 3.15 and hence quantify the effects of small scale background turbulence on the nutrient uptake rate (equation 3.13) of a single phytoplankton cell. It should be pointed out that the expression for Sh is based upon theoretical predictions of nutrient uptake rates in pure shear (non-rotating) flows and its extension to general turbulent flows is somewhat problematic and experiments in the literature are scarce (Keshishian et al., 2013). However in this application typical phytoplankton cells are of the order of $R_p \simeq 10^{-5}\text{m}$ which implies that $Pe_t(z) < 0.008$ for all $\langle \epsilon(z) \rangle$ values derived from the boundary layer dynamics, even in the most turbulent simulations. Consequently Sh is never greater than about 1.08, meaning that the uptake rate is only marginally above that generated by diffusion alone, for which there is strong empirical evidence (Yao et al., 2011). Hence equation 3.13 and equation 3.16 should provide good estimates of the required uptake rate.

Equations 3.13 and 3.16 give the uptake rate as a prescribed by the physical fluid dynamics in which the cell finds itself. However, it is important to recognise that the physiological state of the cell also plays a key role in regulating the uptake rate. In

particular if $\frac{N_W}{N_0} > 1$ the cell is satiated with nutrient, in which case uptake will cease. So the level of satiation as prescribed by the parameter $\frac{N_W}{N_0}$ is important. Unfortunately estimating N_W , the nutrient concentration at the cell wall, against the backdrop of a turbulent flow is a difficult proposition. So instead, following the example of Baird et al. (2001), we frame the question in a somewhat different way. The uptake rate will obviously depend upon the nutrient reserve in the cell, which are already stored at any one time. This level of reserves will be denoted by R_N , the reserves available assuming the local nutrient concentration is N . If R_N is low, the cell will be ‘hungry’ for nutrients and consequently the nutrient uptake rate is likely to be large. Baird et al. (2001) formulated the assumption that the level of R_N was linearly related to the local nutrient concentration and consequently the question of determining the level of $\frac{N_W}{N_0}$ in 3.13, could be answered by establishing the level of the relative nutrient reserves $\frac{R_N}{R_N^{\max}}$ currently within the cell (here R_N^{\max} is a measure of the maximum storage capacity of an average cell).

To establish the level of nutrient reserves, Baird et al. (2001) then asked the question, for what reason does the cell require to take up nutrients? The answer of course is to promote cell growth, from which the authors postulated the idea that storage reserves depend upon cell reproduction and that all things considered, a position of equilibrium would eventually be reached, in which there is a mass balance between the nutrients taken in and the nutrients used up to promote cell growth. This led them to postulate the following equation (with $\frac{N_W}{N_0}$ replaced by $\frac{R_{N_0}}{R_N^{\max}}$, where R_{N_0} is the reserves assuming the global average nutrient concentration is $N = N_0$), linking the uptake rate to cell reproduction,

$$4\pi R_p ShDN_0 \left(1 - \frac{R_{N_0}}{R_N^{\max}}\right) = \mu_P^{\max} \frac{R_{N_0}}{R_N^{\max}} (s_N + R_{N_0}). \quad (3.17)$$

Here μ_P^{\max} is the maximum phytoplankton growth rate and s_N is a nutrient stoichiometry coefficient, which quantifies the minimal amount of nutrient a cell needs to be

viable. Cell reproduction can only take place if $R_N^{max} > s_N$. The excess can be used in the production of daughter cells. In this work R_N^{max} was assumed to equal three times s_N (Lewis, 2005). The assumption made by Baird et al. (2001) in formulating 3.17, was that mass balance will occur in the absence of any relative fluid motion and it is arguable that no such equilibrium could ever be attained in a situation of a rapidly varying turbulent flow. It is our assumption that on small planktonic scales the fluid motion is dominated by viscosity and consequently is relatively slow moving and hence equation 3.17 is not too far from reality.

Equation 3.17 is essentially a quadratic equation for the unknown value R_{N_0} and the ratio $\frac{R_{N_0}}{R_N^{max}}$. However, even after solving equation 3.17 for R_{N_0} we must still compute the value of $\frac{R_N}{R_N^{max}}$ at a general nutrient concentration level N (different from the background concentration N_0 due to the local flow field). Usually N will not differ substantially from N_0 , so we choose to employ a linear relationship linking the general ratio to the specific background level of the form,

$$\frac{R_N(\mathbf{x}, t)}{R_N^{max}} = \begin{cases} \frac{R_{N_0}}{R_N^{max}} \times N & \text{provided this is } \leq 1 \\ 0 & \text{otherwise.} \end{cases} \quad (3.18)$$

Substituting this result into 3.13 gives our final expression for the nutrient uptake rate,

$$Q(\mathbf{x}, t) = \begin{cases} 4\pi R_P Sh(z) D_N N \left[1 - \frac{R_N}{R_N^{max}} \right] & 0 \leq \frac{R_N}{R_N^{max}} \leq 1 \\ 0 & \text{otherwise,} \end{cases} \quad (3.19)$$

and hence

$$\text{'N uptake by P'} = \begin{cases} P_0 4\pi R_P Sh(z) D_N \left[1 - \frac{R_N}{R_N^{max}} \right] P N & 0 \leq \frac{R_N}{R_N^{max}} \leq 1 \\ 0 & \text{otherwise,} \end{cases} \quad (3.20)$$

at any position \mathbf{x} and time t in the flow.

3.2.2 Phytoplankton Growth

When modelling phytoplankton growth, there are certain things to take into account. Phytoplankton use photosynthesis as a way to take in energy and so part of it's growth must be attributed to light levels, which decrease with depth (we will assume this decrease is exponential). There is also an efficiency to how much energy phytoplankton can take out of the nutrients which are ingested, this efficiency will be denoted by $\beta_E \in (0, 1)$ and there is a limit with regards to how satiated the cell is (as described in the previous term). Hence, following Baird et al. (2001), phytoplankton growth can be modelled in the following way,

$$\text{'P growth from N'} = \beta_E \min \left[\frac{R_N}{R_N^{\max}}, 1 \right] e^{\alpha z} \mu_P^{\max} P \quad (3.21)$$

where μ_P^{\max} is the maximum growth rate of the phytoplankton and α is a light attenuation co-efficient.

3.2.3 Nitrate Recycled from Phytoplankton

Again, analogous to the previous term, this term is proportional to the growth of phytoplankton. Additionally, it takes into account that when the phytoplankton cell dies, it is converted solely into nutrients. It also assumes that when the phytoplankton cell dies, it has a nutrient reserve of that equal to the stoichiometry co-efficient (the minimum amount of nutrients needed to survive). This term can be expressed as

$$\text{'N recycled from P'} = (1 - \beta_E) \min \left[\frac{R_N}{R_N^{\max}}, 1 \right] e^{\alpha z} \mu_P^{\max} \frac{s_N P_0}{N_0} P. \quad (3.22)$$

3.2.4 Zooplankton Predation

Many studies have shown that enhanced levels of turbulent mixing can bring about profound changes to the predation rate (Pécseli et al., 2012; Visser et al., 2009). Consequently one needs a model of planktonic predation that provides robust predation estimates in turbulent flows of the kind simulated in the LES boundary layer model

discussed in Chapter 2. I will be using a term based on the formulation (and derivation) of Rothschild and Osborn (1988) and Lewis and Pedley (2000, 2001).

Formulation

The basis of the formulation of zooplankton predation capabilities in turbulence relies on certain simplifying characteristics of turbulence at small length scales (e.g. between $\eta_k - 10\eta_k$). These include isotropy, homogeneity and statistical stationarity. All ocean boundary layer flows exhibit these characteristics at small scales. In addition, it is assumed that predator and prey are sufficiently small that their presence creates no significant disturbance to the flow itself, although in some cases, zooplankton generate their own flow fields to entrain prey into their vicinity (Malkiel et al., 2003).

Zooplankton have particular sensory organs to detect prey chemically, hydrodynamically and in the case of fish larvae, visually (Price, 1988). This means a sensory perception field must be included. Experimental studies have shown zooplankton have varying fields of perception, depending on the species and these take on a variety of complex geometrical shapes (Lewis and Bala, 2006). Again, such complexity and variety is too difficult to attempt to incorporate in an LES code so in this work, zooplankton predation will be based around the premise that the perception field is hemispherical. That means if any prey comes within a distance ‘ R ’ of the zooplankton, at any orientation directed in front of the predator, it will be perceived and an attack sequence will be initiated.

Most zooplankton are capable of swimming (Li et al., 2013) and any such motion must be taken into account as this is how the zooplankton forage for prey. The background turbulent motion is also crucial, as the length scales on which the zooplankton tend to perceive their prey lie in the inertial subrange, the characteristics of which are fairly well understood. Rather than model the mechanism for predation in an Eulerian framework, a Lagrangian framework is taken for convenience. To do this we first need to define variables which describe the constituent velocity components which, when

pieced together, comprise the relative velocity scale. These are \mathbf{v}_Z , \mathbf{v}_P and \mathbf{w} , which are the swimming velocities of the zooplankton and phytoplankton, and the local turbulent velocity scale respectively. Now assuming the zooplankton and phytoplankton are at distance r from each other, the velocity component of each of these can be expressed as

$$\mathbf{V}_Z = \mathbf{v}_Z + \mathbf{w}(\mathbf{x}, t), \quad (3.23)$$

$$\mathbf{V}_P = \mathbf{v}_P + \mathbf{w}(\mathbf{x} + \mathbf{r}, t). \quad (3.24)$$

Here \mathbf{V}_Z and \mathbf{V}_P are the velocities of each planktonic particle and we define the relative velocity at a distance R (the contact radius of the zooplankton perception field) apart by

$$\mathbf{U}(\mathbf{x}, R, t) = \mathbf{V}_Z(\mathbf{x}, t) - \mathbf{V}_P(\mathbf{x} + R, t). \quad (3.25)$$

Now consider a frame of reference centred on the zooplankton predator moving at this relative speed \mathbf{U} (so the prey is stationary). Without loss of generality, one can assume the predator is moving in a straight line along the z -axis for instance, see figure 3.1. (the modifications necessary to account for an irregular foraging trajectory will be discussed later in the section). Mathematically, the structure of the predation rate term takes the form;

Predation rate = Number of contacts encountered per unit time (Encounter rate) \times probability of a contact being subsequently captured.

The encounter rate is a precondition for the predation rate (a prey must first be encountered before it can be captured) and will be derived first.

In words, the encounter rate can be formulated as follows;

Encounter rate (ER) =

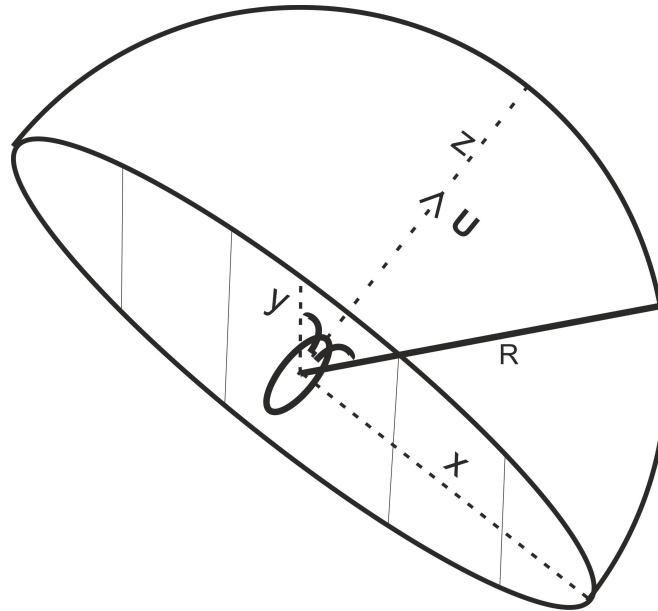


Figure 3.1: Schematic showing the relative swimming trajectory in the z direction, the radius of R of the hemisphere and the relative velocity of the zooplankton \mathbf{U} .

area of the perception field at $r = R$ projected onto the $x - y$ plane (perpendicular to the direction of swimming along the z -axis) \times

prey density (ρ_P - where P denotes phytoplankton) \times

relative velocity, \mathbf{U} , on entering the sphere \times

probability of moving with that velocity.

As discussed, the shape of the volume in which zooplankton can perceive their prey is assumed to be hemispherical. It is therefore convenient to work in spherical polar co-ordinates. The zooplankton will register a contact the moment a prey particle enters the shell of its contact hemisphere at a radial distance $r = R$, between polar and

azimuthal angle intervals $(\chi, \chi + \delta\chi)$ and $(\phi, \phi + \delta\phi)$. It is also important to note that it is not the resulting surface area that will be proportional to the amount of prey passing into the contact hemisphere, but rather the surface area as a projection onto the ‘base’ of the hemisphere, see figure 3.2. In general the projected cross sectional area is based

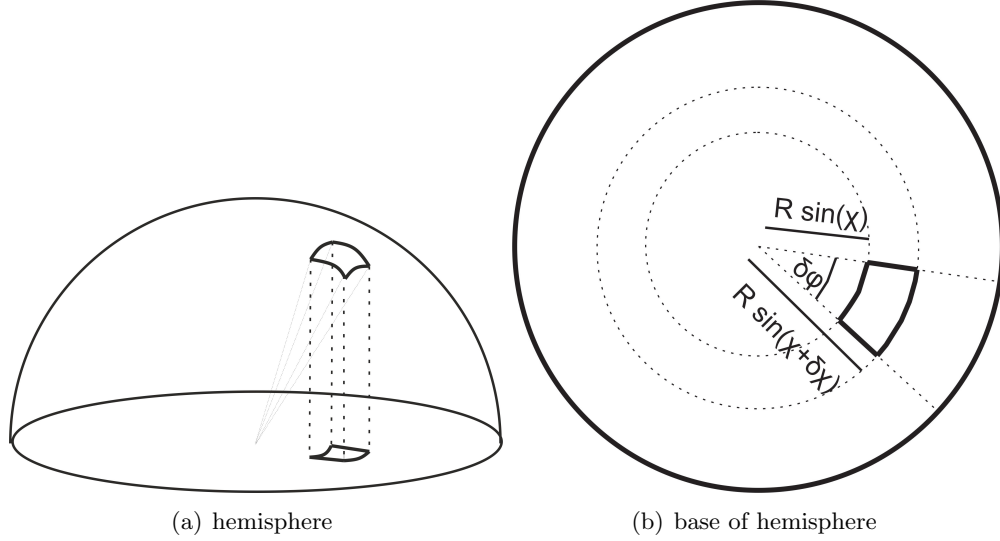


Figure 3.2: Diagram showing the surface element, where a prey particle can be potentially detected and its elemental area as a projection on to the base of the contact hemisphere.

on how good the predators sensory organs are i.e. for what range of (r, ϕ, χ) it can detect chemical trails over or sense the presence of something edible hydro-mechanically. For a hemispherical perception field, the elemental cross sectional area (shown in figure 3.2(b)) can be calculated in the form,

$$\begin{aligned}
 & \frac{R^2}{2} \{ \sin^2(\chi + \delta\chi) - \sin^2\chi \} \delta\phi \\
 &= \frac{R^2}{2} \delta(\sin^2\chi) \delta\phi \\
 &= \frac{R^2}{2} \sin(2\chi) \delta\chi \delta\phi.
 \end{aligned} \tag{3.26}$$

Now consider the relative velocity scale \mathbf{U} and the probability that predator and prey close in on one another at this velocity. The probability density function of travelling with velocities between intervals $(\mathbf{V}_P, \mathbf{V}_P + \delta\mathbf{V}_P)$ and $(\mathbf{V}_Z, \mathbf{V}_Z + \delta\mathbf{V}_Z)$ conditional of being a distance R apart is given by

$$p_{P,Z}(\mathbf{V}_Z, \mathbf{V}_P | R) \delta\mathbf{V}_P \delta\mathbf{V}_Z. \quad (3.27)$$

The form of this distribution will be discussed later. We can formulate the product (relative velocity and the associated probability) needed for the encounter rate by,

$$\mathbf{U}(R) p_{P,Z}(\mathbf{V}_Z, \mathbf{V}_P | R) \delta\mathbf{V}_P \delta\mathbf{V}_Z. \quad (3.28)$$

Consequently in mathematical form, the number of prey first registered when entering the elemental section of the ‘contact hemisphere’ in spherical polar co-ordinates is given by

$$\rho_P \frac{R^2}{4} \sin(\theta) \mathbf{U}(R) p_{P,Z}(\mathbf{V}_Z, \mathbf{V}_P | R) d\mathbf{V}_P d\mathbf{V}_Z d\theta d\phi. \quad (3.29)$$

where $\theta = 2\chi$. Here we assume ρ_P is a constant. Obviously ρ_P falls as the prey are consumed, but usually the density of the prey is very much larger than the number of predators, so these losses are negligible.

We now need to integrate over all angle and velocity variables to give the encounter rate over the entire hemisphere

$$\frac{\rho_P R^2}{2} \int_{\mathbf{V}_P} \int_{\mathbf{V}_Z} \int_0^{\frac{\pi}{2}} \int_0^{2\pi} \mathbf{U}(R) p_{P,Z}(\mathbf{V}_Z, \mathbf{V}_P | R) \sin(2\chi_R) d\phi_R d\chi_R d\mathbf{V}_P d\mathbf{V}_Z.$$

However, since the integrand contains the relative velocity variable \mathbf{U} , it is easier to compute this integral by means of the following change of variables:

$$\mathbf{U}(\mathbf{x}, \mathbf{r}, t) = \mathbf{V}_Z(\mathbf{x}, t) - \mathbf{V}_P(\mathbf{x} + \mathbf{r}, t),$$

$$\mathbf{V}(\mathbf{x}, \mathbf{r}, t) = \frac{\sigma_{\mathbf{V}_Z}^2 \mathbf{V}_P(\mathbf{x} + \mathbf{r}, t) + \sigma_{\mathbf{V}_P}^2 \mathbf{V}_Z(\mathbf{x}, t)}{\sigma_{\mathbf{V}_Z}^2 + \sigma_{\mathbf{V}_P}^2}, \quad (3.30)$$

where $\sigma_{\mathbf{V}_i}^2$ is the variance of the velocity component \mathbf{V}_i , $i = Z, P$ and $\sigma_{\mathbf{V}_i}^2 = \frac{1}{3}(\langle \mathbf{V}_i \cdot \mathbf{V}_i \rangle - \langle \mathbf{V}_i \rangle \langle \mathbf{V}_i \rangle)$. Here $\langle \cdot \rangle$ denotes a probability average and will be used throughout this work. Equation 3.30 is completely general and applies for any type of flow field and swimming distributions. However, it can be greatly simplified if one makes certain assumptions about the characteristics governing the dynamics of an encounter event. For example, the swimming speeds, v_i (where $i = P, Z$), of the phytoplankton and zooplankton vary from individual to individual, about a certain mean value. This type of behaviour is well summarised by assuming planktonic swimming speeds are drawn from Gaussian distributions. Using an appropriate probability distribution for Gaussian swimming, given by the normal (3 dimensional) distribution, one can determine an average value for the swimming velocity variance, i.e.

$$\begin{aligned} \langle \mathbf{v}_i \cdot \mathbf{v}_i \rangle = & \\ & \left(\frac{1}{\sqrt{2\pi}\sigma_i} \right)^3 \int_{-\infty}^{\infty} \int_{-\infty}^{\infty} \int_{-\infty}^{\infty} |\mathbf{v}_i|^2 \exp \left[\frac{-(v_{ix}^2 + v_{iy}^2 + v_{iz}^2)}{2\sigma_i^2} \right] dv_{ix} dv_{iy} dv_{iz}, \end{aligned} \quad (3.31)$$

where σ_i is the standard deviation of \mathbf{v}_i . Then, transforming into spherical polar coordinates, we arrive at the equation

$$\langle \mathbf{v}_i \cdot \mathbf{v}_i \rangle = \frac{4\pi}{(\sqrt{2\pi}\sigma_i)^3} \int_0^{\infty} v_{ir}^4 \exp \left[\frac{-v_{ir}^2}{2\sigma_i^2} \right] dv_{ir} = 3\sigma_i^2, \quad (3.32)$$

where $v_{ir} = \sqrt{v_{ix}^2 + v_{iy}^2 + v_{iz}^2}$. Also, in a similar way, we can derive an expression for the average speed

$$v_i = \langle |\mathbf{v}_i| \rangle = \frac{4\pi}{(\sqrt{2\pi}\sigma_i)^3} \int_0^{\infty} v_{ir}^3 \exp \left[\frac{-v_{ir}^2}{2\sigma_i^2} \right] dv_{ir} = \sqrt{\frac{8}{\pi}} \sigma_i, \quad (3.33)$$

where v_i is the average swimming speed (as distinct from the velocity). This result will be used later in the derivation for the predation rate.

For the change of variables in equation 3.30, it can be shown that the Jacobian determinant is given by,

$$\left| \frac{\partial(\mathbf{V}_Z, \mathbf{V}_P)}{\partial(\mathbf{U}, \mathbf{V})} \right| = 1,$$

so that that encounter rate can be rewritten in the form

$$\text{ER} = \frac{\rho_P R^2}{4} \int_{\mathbf{U}} \int_{\mathbf{V}} \int_0^\pi \int_0^{2\pi} \mathbf{U}(R) p_{\mathbf{U}, \mathbf{V}}(\mathbf{U}, \mathbf{V} | R) \sin(\theta_R) d\phi_R d\theta_R d\mathbf{U} d\mathbf{V}$$

where $\theta_R = 2\chi_R$. This can be simplified slightly (by integrating over all angle components), assuming $\mathbf{U}(\mathbf{R}) = \mathbf{U}(R)$ to an integral depending on velocity components alone, i.e.

$$\text{ER} = \rho_P \pi R^2 \int_{\mathbf{U}} \int_{\mathbf{V}} \mathbf{U}(R) p_{\mathbf{U}, \mathbf{V}}(\mathbf{U}, \mathbf{V} | R) d\mathbf{U} d\mathbf{V}. \quad (3.34)$$

In principle, if $p_{\mathbf{U}, \mathbf{V}}(\mathbf{U}, \mathbf{V} | R)$ is known, then it would be possible to calculate the contact rate exactly. Unfortunately, there is only a rather incomplete knowledge pertaining to $p_{\mathbf{U}, \mathbf{V}}(\mathbf{U}, \mathbf{V} | R)$ applicable to turbulent flows. Consequently we have to put forward a model approximation for $p_{\mathbf{U}, \mathbf{V}}(\mathbf{U}, \mathbf{V} | R)$ which encapsulates the main features of the flow. Lewis and Pedley (2000) argue that a suitable choice of distribution is the following binormal probability density function given by

$$p_{\mathbf{U}, \mathbf{V}}(\mathbf{U}, \mathbf{V} | r) = \frac{1}{\left[2\pi\sigma_U\sigma_V(1-\zeta^2)^{\frac{1}{2}} \right]} \exp \left[\left\{ -\frac{1}{2(1-\zeta^2)} \right\} \right. \\ \left. \left\{ \frac{(\mathbf{V} - \langle \mathbf{V} \rangle)^2}{\sigma_V^2} + \frac{(\mathbf{U} - \langle \mathbf{U} \rangle)^2}{\sigma_U^2} \right. \right. \\ \left. \left. - \frac{2\zeta(\mathbf{U} - \langle \mathbf{U} \rangle) \cdot (\mathbf{V} - \langle \mathbf{V} \rangle)}{\sigma_U\sigma_V} \right\} \right] \quad (3.35)$$

where $\zeta = \frac{\mathbf{U} \cdot \mathbf{V}}{3\sigma_U\sigma_V}$. Lewis and Pedley (2000) argue this distribution is a good approximation, partly because the distribution is exact when the separation $r \rightarrow 0$ and $r \rightarrow \infty$.

It is also convenient to employ, because the binormal distribution is readily integrated. We will also make the assumption that zooplankton and phytoplankton display ‘Gaussian swimming’ behaviour (discussed above). This means v_P and v_Z follow three dimensional isotropic Gaussian distributions with zero means and standard deviations σ_P and σ_Z respectively. Applying this assumption means that both $\langle \mathbf{U} \rangle = \langle \mathbf{V} \rangle = 0$.

To compute the complicated integral, the following change of variables is employed

$$\mathbf{p} = \frac{\mathbf{U} - \langle \mathbf{U} \rangle}{\sigma_U} \Rightarrow |\sigma_U \mathbf{p}| = |\mathbf{U}|$$

$$\mathbf{q} = \frac{1}{(1 - \zeta^2)^{\frac{3}{2}}} \left(\frac{\mathbf{V} - \langle \mathbf{V} \rangle}{\sigma_V} - \zeta \frac{\mathbf{U} - \langle \mathbf{U} \rangle}{\sigma_U} \right). \quad (3.36)$$

The choice of variable becomes clear when looking at the term $p^2 + q^2$ as this is, except for a factor, the argument in the exponential term in $p_{\mathbf{U}, \mathbf{V}}(\mathbf{U}, \mathbf{V} | r)$. The determinant of the Jacobian is given by

$$\left| \frac{\partial(\mathbf{p}, \mathbf{q})}{\partial(\mathbf{U}, \mathbf{V})} \right| = \frac{1}{(\sigma_U \sigma_V)^3 (1 - \zeta^2)^{\frac{3}{2}}}$$

and so the integral in equation 3.34 becomes

$$\rho_P \pi R^2 \int_q \int_p \frac{1}{(2\pi)^3} p \sigma_U(R) e^{-\frac{1}{2}(p^2 + q^2)} dp dq.$$

Expressing \mathbf{p} and \mathbf{q} in spherical polar co-ordinates (e.g. $\mathbf{q} = q(\sin\theta_q \cos\phi_q, \sin\theta_q \sin\phi_q, \cos\theta_q)$) and finding Jacobian determinants of each i.e.

$$\left| \frac{\partial \mathbf{p}}{\partial(p, \theta_p, \phi_p)} \right| = p^2 \sin\theta_p,$$

$$\left| \frac{\partial \mathbf{q}}{\partial(q, \theta_q, \phi_q)} \right| = q^2 \sin\theta_q,$$

equation 3.34 can be expressed as

$$ER = \frac{\rho_P \pi R^2 \sigma_U(R)}{(2\pi)^3} \int_0^\infty p^3 e^{-\frac{p^2}{2}} dp \times \int_0^\infty q^2 e^{-\frac{q^2}{2}} \times \int_0^\pi \sin\theta_p d\theta_p \times \int_0^\pi \sin\theta_q d\theta_q \times \int_0^{2\pi} d\phi_p \times \int_0^{2\pi} d\phi_q. \quad (3.37)$$

This can finally be integrated relatively simply to give the encounter rate,

$$ER = 4\rho_P R^2 \sqrt{\frac{\pi}{2}} \sigma_U(R) \quad (3.38)$$

We now need to find $\sigma_U(R)$ explicitly in terms of R . This term will also give information about the flow as the relative velocity $\mathbf{U}(R)$ is a function of the turbulent velocity component. This term is essential in characterising the effect of which turbulence has on planktonic competition. $\sigma_U(R)$ is defined as

$$\sigma_U^2(R) = \frac{\langle \mathbf{U} \cdot \mathbf{U} \rangle - \langle \mathbf{U} \rangle \cdot \langle \mathbf{U} \rangle}{3} = \frac{\langle \mathbf{U} \cdot \mathbf{U} \rangle}{3} \quad (3.39)$$

assuming Gaussian swimming. Decomposing $\mathbf{U}(R)$ into it's constituent parts (equations 3.23 - 3.25) we find that equation 3.39 includes many cross terms which equate to zero because the turbulent velocity, zooplankton swimming and phytoplankton swimming are independent. For example $\langle \mathbf{v}_P \cdot \mathbf{v}_Z \rangle = 0$. With these simplifications, equation 3.39 becomes

$$\begin{aligned} \frac{\langle \mathbf{U} \cdot \mathbf{U} \rangle}{3} &= \frac{\langle \mathbf{v}_P \cdot \mathbf{v}_P \rangle}{3} + \frac{\langle \mathbf{v}_Z \cdot \mathbf{v}_Z \rangle}{3} + \\ &\frac{2 \langle \mathbf{w}(\mathbf{x}, t) \cdot \mathbf{w}(\mathbf{x}, t) \rangle}{3} - \frac{2 \langle \mathbf{w}(\mathbf{x}, t) \cdot \mathbf{w}(\mathbf{x} + R, t) \rangle}{3} \\ &= \sigma_{v_P}^2 + \sigma_{v_Z}^2 + \frac{2}{3} [\langle \mathbf{w}_x^2 \rangle - \langle \mathbf{w}_x \mathbf{w}_{x+R} \rangle] \end{aligned} \quad (3.40)$$

Batchelor (1953) derived an exact formulation for the latter term in equation 3.40 in the form,

$$[\langle w_x^2 \rangle - \langle w_x w_{x+R} \rangle] = 2 \int_0^\infty E(k, t) \left[1 - \frac{\sin(kR)}{kR} \right] dk, \quad (3.41)$$

where $E(k, t)$ is the turbulent kinetic energy spectrum of the flow in question, it depends mainly upon at what depth one is at in the boundary layer. Now as the contact radius lies within the inertial subrange, one typically only requires the contribution of that part of $E(k, t)$ relevant to that range. Usually, that mean $E(k, t) \propto \langle \epsilon \rangle^{2/3} k^{-5/3}$. The integral can then be approximated by

$$\frac{4}{3} \int_0^\infty E(k) \left(1 - \frac{\sin(kR)}{kR} \right) dk = 2 \langle \epsilon \rangle^{2/3} \int_{\frac{1}{L}}^{\frac{1}{\eta_K}} k^{-5/3} \left(1 - \frac{\sin(kR)}{kR} \right) dk \quad (3.42)$$

where L is the large eddy size, η_K is the Kolmogorov length scale and the inertial subrange is defined to lie between $k \in (\frac{1}{L}, \frac{1}{\eta_K})$. Then let $k^* = k\eta_K$, equation 3.42 becomes

$$2 \langle \epsilon \rangle^{2/3} \int_{\frac{\eta_K}{L}}^1 \left(\frac{k^*}{\eta_K} \right)^{-5/3} \left(1 - \frac{\sin(k^*R/\eta_K)}{k^*R/\eta_K} \right) dk^* = \quad (3.43)$$

$$2 \langle \epsilon \rangle^{2/3} \int_0^1 \left(\frac{k^*}{\eta_K} \right)^{-5/3} \left(1 - \frac{\sin(k^*R/\eta_K)}{k^*R/\eta_K} \right) dk^*$$

since $\frac{\eta_K}{L} \ll 1$. Now, let $x = \frac{k^*R}{\eta_K}$, then equation 3.43 becomes

$$2 \langle \epsilon \rangle^{2/3} \int_0^{\frac{R}{\eta_K}} x^{-5/3} \left(1 - \frac{\sin(x)}{x} \right) dx \approx \langle \epsilon \rangle^{2/3} \times 0.6 \quad (3.44)$$

where the integral has been calculated for $\frac{R}{\eta_K} = 2$, a value that will be used later in this work, and finally,

$$\begin{aligned} \sigma_U^2(R) &= \sigma_P^2 + \sigma_Z^2 + 0.6(\langle \epsilon \rangle R)^{2/3} = \\ &= \frac{\pi}{8} \left(v_P^2 + v_Z^2 + \frac{8}{\pi} 0.6(\langle \epsilon \rangle R)^{2/3} \right) = \\ &= \frac{\pi}{8} (v_P^2 + v_Z^2 + w_T^2), \end{aligned} \quad (3.45)$$

where w_t is the turbulent velocity scale. So finally, one obtains a relatively simple (but quite accurate) approximation to the encounter rate, given by

$$ER = \pi \rho_p R^2 [w_T^2 + v_P^2 + v_Z^2]^{\frac{1}{2}}. \quad (3.46)$$

This relatively ‘simple’ formula has a crucial drawback in its formulation as we have implicitly assumed that all the motion is linear, i.e. the relative trajectory of a predator and its prey is a straight line. The vector \mathbf{U} is assumed to correspond to the z -axis. In reality, this is not so. Planktonic predators are observed to frequently change direction whilst foraging (Bundy et al., 1998) and even if they did swim in straight lines, the random nature of the turbulent flow would gradually cause the predators path to become irregular (Yamazaki and Kamykowski, 1991). This observation means that formula 3.46 is actually an upper bound on the predators encounter rate and one should say, more precisely, that

$$\max(ER) = \pi \rho_p R^2 [w_T^2 + v_P^2 + v_Z^2]^{\frac{1}{2}}. \quad (3.47)$$

The reason equation 3.46 is an upper bound is that if the predator follows an irregular trajectory, it must at some stage revisit a volume of the water column that it has al-

ready visited. Hence its total search volume is reduced and consequently the effect is most apparent if the predator changes swimming direction relatively rapidly, which is in fact what is observed. Typically, copepods tend to re-orientate their search patterns after only a few seconds (Bundy et al., 1998). Fish larvae forage using a ‘pause-travel’ type strategy (Galbraith et al., 2004). This involves swimming at a relatively low speed in a certain direction for a few seconds, before pausing and scanning the local environment for any potential prey. If there is nothing to be found, they initiate a new ‘travel’ phase in a different direction.

Lewis and Pedley (2000, 2001) and Lewis (2003b) examined, in considerable detail, the consequences of adopting these types of non-linear foraging strategies on the encounter rate. In the process, it was established that the actual encounter rate could be estimated using the formula

$$ER = f_v(U(R), R, n, \tau) \times \max(ER), \quad (3.48)$$

where $f_v(U(R), R, n, \tau) \in (0, 1)$ is a volume fraction term. This encapsulated the ratio of the volume mapped out by a predator following a non-linear trajectory to that of a straight-line trajectory. It depends upon $U(R)$ - the relative swimming speed, R - the contact radius of the perception field, τ - the time spent foraging and n - the number of direction changes (or ‘pause-travel’ sequences) the predator makes in a time τ . The formulation of f_v is quite complicated and its evaluation depends upon a series of Monte-Carlo simulations. For this work, very accurate values are not necessary and we note from the papers cited that typical values based upon parameters derived from real planktonic predators suggest f_v takes values in the range from 0.6 to 0.8. In this work a value of 0.7 will be used throughout.

However, knowledge of the contact rate is not sufficient to fully encapsulate the planktonic population dynamics. The interaction term linking the zooplankton (Z) to the

phytoplankton (P) populations is based on the predation rate of the zooplankton. In other words, we want to estimate what proportion of the prey encountered by the predator is actually captured and eaten. Experimental observations indicate this is less than 50% for some predator-prey encounters (Jönsson et al., 2012). So the question becomes, how can one utilise the ideas behind the formulation of the encounter rate in equation 3.48, to derive a separate estimate of the predation rate, to be employed in the LES-NPZ model? This is difficult question. The major complication inherent in any estimate of the predation rate is the fact that on encountering a potential prey, predatory reactions are highly specific to the particular species in question.

Zooplankton, as a whole, have a plethora of mechanisms which aid in survival. Sacrifices must be made however, as feeding, survival, reproduction and growth cannot be maximised simultaneously (Litchman et al., 2013). For a swimmer, encounters with prey particles will be greatly increased, but will greatly increase their chance of being perceived by a predator via being sensed through fluid disturbances (Kiørboe et al., 2010; Tiselius et al., 1997). Diel vertical migration (DVM) is also a strategy used to avoid predators, whereby they swim deeper in the daytime to avoid being perceived by visual predators (Bianchi et al., 2013; Fiksen, 1997) and swim upwards of a night to avoid non-visual predators (Ohman, 1990). In this study however, these effects will not be attempted to be encapsulated as these are enhancing effects to phytoplankton thin layering and patchiness and we are only interested in how the flow stimulates spatial distribution.

To try and encapsulate all these different modes of predatory behaviour, for a myriad of different zooplankton species, into the large scale LES-NPZ model is simply not a feasible proposition due to computational restrictions. What is needed is a relatively simple formalism of estimating predation rates from encounter rates, that can be applied generically across a wide range of different species. It should also be able to include the influence exerted by the small scale fluid motion encapsulated by the

energy dissipation rate $\langle \epsilon \rangle$. In Lewis and Pedley (2001), such a formalism originally derived specifically for predators with spherical perception fields, was proposed. This was based on assigning a simple capture probability to each predator-prey encounter event. Specifically, the probability of capture was given by

$$p_{\text{cap}}(t_{r_m}) = \frac{\langle t_{r_m} \rangle^2}{\langle t_{r_m} \rangle^2 + T_R^2}. \quad (3.49)$$

Here, T_R is a reaction time, specific to each predator, which roughly encapsulates how long it needs to fixate and reduce the relative distance between itself and its prey, in order to be able to capture it. It could also depend upon the prey's escape capabilities. Such a parameter would be relatively easy to estimate for any predator-prey combination. The parameter $\langle t_{r_m} \rangle$ is the average time a prey particle would take to traverse the predators perception field moving at relative speed U , if the predator chose to ignore the prey completely, Lewis and Pedley (2001) suggested that this time frame is indicative of how long the predator would have to make its capture attempt. If $\langle t_{r_m} \rangle \ll T_R$ then the prey would almost certainly escape, but if $\langle t_{r_m} \rangle \gg T_R$ it should be easy for a predator to make a capture. In the formalism $\langle t_{r_m} \rangle$ is not calculated directly. Rather it is written as a function of r_m , defined as the distance of closest approach of the predator and prey under the assumption that neither reacts to the presence of the other. This is important because it makes $p_{\text{cap}}(t_{r_m})$, essentially a function of distance, and we can estimate the number of prey which approach to within an exact distance r_m , by employing an analogous method that used to estimate ER, without going into all the details here, which are discussed in Lewis and Pedley (2001), the predation rate can then be written in the form (c.f. equations 3.38 and 3.48)

$$b(z) = 4\rho_P \sqrt{\frac{\pi}{2}} \int_0^R \frac{\partial}{\partial r_m} [f_v(U(r_m), r_m, n, \tau) r_m^2 \sigma_U(r_m)] p_{\text{cap}}(r_m) dr_m, \quad (3.50)$$

where $b(z)$ is the predation rate. Note that the predation rate is only depth dependant as the turbulent kinetic energy is assumed to be only depth dependant. The partial derivative in this term is a difficult term to calculate but we can see that, when

integrating over r_m we can note the following relationship

$$\begin{aligned}
& \int_0^R \frac{\partial}{\partial r_m} [f_v(U(r_m), r_m, n, \tau) r_m^2 \sigma_U(r_m)] p_{\text{cap}}(r_m) dr_m \\
&= p_{\text{cap}}(r_m) f_v(U(r_m), r_m, n, \tau) r_m^2 \sigma_U(r_m) \Big|_0^R - \\
& \int_0^R \frac{dp_{\text{cap}}}{dr_m} f_v(U(r_m), r_m, n, \tau) r_m^2 \sigma_U(r_m) dr_m \\
&= \int_0^R \frac{-dp_{\text{cap}}}{dr_m} f_v(U(r_m), r_m, n, \tau) r_m^2 \sigma_U(r_m) dr_m
\end{aligned} \tag{3.51}$$

This assumes that $p_{\text{cap}}(R) = 0$, which is satisfied because if the prey's closest approach was R , then it would spend, by definition, no time in the perception field, and the predator would have no chance to catch it. Now, as $\sigma_U(r_m)$ has only been calculated for the limit $r_m = R$ so far, a simple interpolation will be used, so that in the limit $r \rightarrow 0$, there is no contribution from the turbulent flow. Monin and Yaglom (1975) proposed that this should take the form

$$\sigma_U^2(r_m) = \frac{C_1 r_m^2}{1 + C_2 r_m^{\frac{4}{3}}} + \sigma_P^2 + \sigma_Z^2, \tag{3.52}$$

where

$$C_2 = \frac{C_1 R^2 / (w_T^2 - 1)}{R^{\frac{4}{3}}}.$$

Monin and Yaglom (1975) estimate that $C_1 \approx \frac{1}{9}$.

All that remains is to specify the relative path by which the prey traverses the interior of the perception field. Without going into detail, the assumptions are that prey takes a circular arc path through the contact hemisphere and Lewis and Pedley (2001)

derive the average amount of time the prey stays in the contact hemisphere by

$$\langle t_{r_m} \rangle = \sqrt{\frac{2}{\pi}} \int_{\frac{\pi}{2} - \cos^{-1}\left(\frac{R+r_m}{2R}\right)}^{\frac{\pi}{2} + \cos^{-1}\left(\frac{R+r_m}{2R}\right)} \frac{R}{\sigma_U(r_m(s))} ds, \quad (3.53)$$

where $r_m(s) = [(R + r_m)^2 + R^2 - 2R(R + r_m)\sin(s)]^{1/2}$ and s is the path taken through the contact hemisphere. This circular arc patch was adopted for the predation rate estimates employed in the LES-NPZ model.

Finally, using a simple interpolation for $\langle f_v \rangle$ so that $f_v = 1$ at $r_m = 0$ (when the predator won't need to change direction to catch the prey), we can set $\langle f_v \rangle = 1 - 0.3\frac{r_m}{R}$, which gives the predation rate,

$$\text{'P grazing loss from Z'} = Z_0 A \sqrt{\frac{\pi}{2}} \int_0^R \frac{-dp_{\text{cap}}}{dr_m} \left(1 - 0.3\frac{r_m}{R}\right) r_m^2 \sigma_U(r_m) dr_m PZ. \quad (3.54)$$

This is a straight-forward integral to evaluate numerically at all depths z . Note that the depth dependence comes about through σ_U , which declines with depth because $E(k, t)$ is also declining with depth. Figure 3.3 shows the profile of the predation rate. It shows that higher levels of turbulence (inherent in higher wind-stress regimes) increase the predation rate, it also shows that for the highest wind-stress value, the high levels of turbulence at the surface have a negative impact on the predation rate. This shows that turbulence is beneficial for zooplankton as it drastically increases the amount of predator-prey encounters, but too much turbulence can be a hindrance, as prey can escape more easily (Pécseli et al., 2012).

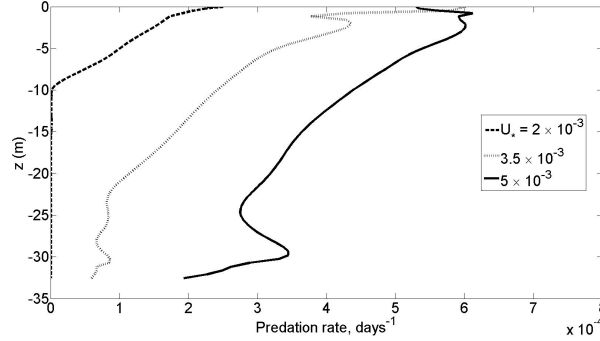


Figure 3.3: Graph showing the different predation rates one can expect to find in a turbulent regime driven by different levels of wind stress. The dashed line indicates the predation rate in a flow subjected to low wind stress ($U_* = 2 \times 10^{-3} \text{ms}^{-1}$), the dotted (fainter) line shows the predation rate for a moderate wind stress ($U_* = 3.5 \times 10^{-3} \text{ms}^{-1}$) and the solid line, a high wind stress ($U_* = 5 \times 10^{-3} \text{ms}^{-1}$).

3.2.5 Zooplankton Growth

Using the previous term derived, we can construct an analogous term for the growth of Z , i.e.

‘Z growth from P’ =

$$\min \left[\mu_Z^{\max}, Y Z_0 4 \rho_P \sqrt{\frac{\pi}{2}} \int_0^R \frac{-dp_{\text{cap}}}{dr_m} \left(1 - 0.3 \frac{r_m}{R} \right) r_m^2 \sigma_U(r_m) dr_m \right] P Z \quad (3.55)$$

where μ_Z^{\max} is the maximum growth rate of the zooplankton and $Y \in (0, 1)$ describes how efficient the zooplankton are extracting energy from the phytoplankton.

3.2.6 Zooplankton Death

As we are not including any organism higher up the food chain than zooplankton in this model (due to computational restrictions), it only makes sense to model the death rate as a simple linear function,

$$\text{‘Z death’} = \mu_Z^{\text{death}} Z \quad (3.56)$$

where μ_Z^{death} is the zooplankton death rate.

3.3 Nutrient Surges

In nature, nutrients can enter a system in many circumstances, from oceanic currents, which carry nutrients from the ocean floor up to the surface waters (Traganza et al., 1980), to a river estuary, which carries nutrients from mountains, volcanoes or land into the seas (Frogner et al., 2001). The Galapagos Islands, for instance, consist of newly formed volcanic rock which is rich with iron from the Earth's core and is subject to abrasion from the surrounding waters and so the surrounding ocean waters are iron rich (Palacios, 2002) which is one of the reasons why this group of islands are a fertile breeding ground for phytoplankton populations.

Many models in the literature which predict nutrient dynamics in the ocean must take into account the oceanic currents (Lancelot et al., 2009; Palter et al., 2010; Tagliabue et al., 2010), which are very large scale processes, something which cannot be incorporated into the LES model due to spatial restrictions. Nutrient waves can be very diverse in form, from large scale currents pulling up ocean-bed nutrients (Anderson et al., 2009) to smaller (but significant) nutrient fluxes from rivers and estuaries (Moore, 2010). The process, yet so diverse, is most notably on large scales and so a first principles mechanistic derivation is not appropriate and a simple model is all that is needed.

There will be two aspects to take into consideration when modelling the local concentration of nutrients. The internal nutrient dynamics, for example, the replenishment from the death and decay of phytoplankton cells which are already in the system, offsetting the losses due to phytoplankton ingestion. Also, as would be expected, the external nutrient influxes, which are arguably the most conducive to the formation of phytoplankton blooms. This is because a nutrient surge is likely to promote a growth

spurt in the local phytoplankton populations which rely principally on nutrient ingestion as a food resource. This in turn will provide additional resources for larger species higher up in the planktonic food chain.

The nutrient boundary conditions imposed include zero flux at the surface, i.e.

$$\left. \frac{\partial N}{\partial z} \right|_{z=0} = 0 \quad (3.57)$$

and a net positive flux from the base of the mixed layer e.g.

$$D_N \left. \frac{\partial N}{\partial z} \right|_{z=z_{ml}} = \langle wN \rangle, \quad (3.58)$$

where z_{ml} is the depth of the mixed layer.

Based on the work of Williams and Follows (1998), we employ a basic background flux into the mixed layer of $2 \times 10^{-8} \text{ mol Nm}^{-2} \text{ s}^{-1}$, which is equivalent to $\langle wN \rangle = 2.8 \times 10^{-10} \text{ kg m}^{-2} \text{ s}^{-1}$ and so the boundary condition is given by

$$wN(x, y)|_{z=z_{ml}} = \langle wN \rangle|_{z=z_{ml}} = 2.42 \times 10^{-5} \text{ kg m}^{-2} \text{ days}^{-1}. \quad (3.59)$$

This background boundary condition is taken at the base of the mixed layer as this is where new nutrients will enter the system.

In terms of simulating a successful phytoplankton bloom, it is important to also incorporate some form of nutrient surge into these boundary conditions. In this instance, we decided to impose the surge at the mixed layer base, but we equally well could have employed it at the surface. In our case, the surge is modelled mathematically in the form of a Gaussian distribution at $z = z_{ml}$ with mean at the centre $x = y = 0$. This means that this ‘Gaussian pump’ will be concentrated at the centre and small near the horizontal boundaries ($x, y \in [-60\text{m}, 60\text{m}]$). The reason for this particular het-

erogeneous construct is to encourage heterogeneity in the phytoplankton distribution. Specifically this boundary condition will therefore take the form

$$wN(x, y) = \langle wN \rangle|_{z=z_{ml}} \left[1 + Q \exp\left(\frac{-x^2 - y^2}{\sigma_{xy}^2}\right) \right]. \quad (3.60)$$

Here Q is a measure of the nutrient pump strength, (x, y) are the horizontal spatial variables and $\sigma_{xy}^2 > 0$ is the variance of the Gaussian distribution associated with the nutrient pump. This parametrisation is also very convenient as it will be easy to analyse the effect of different nutrient pump strengths simply by augmenting the parameter Q . Figure 3.4 shows this boundary condition for $Q = 10$ and $\sigma_{xy}^2 = 50$ and 200 respectively. The main objective of this work is to find the link between turbulent mixing and phytoplankton heterogeneity; therefore we don't want to help aggregations too much with nutrients. A way to make sure that the nutrient field is not playing a major spatial role is to have a large constant flux of nutrients. This will ensure that the phytoplankton become satiated within a given time frame, which means they won't feel the spatial distribution of nutrients after this time. A value of $Q = 130$ (with realistic biological parameters) ensures satiation happens after ≈ 7 days and hence forth will be used for most simulations in this work. This of course is not biologically plausible, but is key to removing the biological contribution towards patch formation (although it is definitely needed initially to promote patchiness).

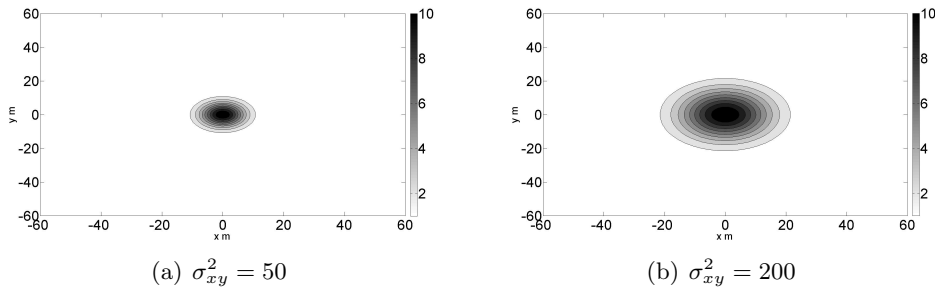


Figure 3.4: Nutrient concentrations at the base of the mixed layer, with pump strength, $Q = 10$ with two different variances. These nutrient concentrations are also normalised by the ambient nutrient flux $\langle wN \rangle|_{z=z_{ml}}$.

This concludes the formulation of the biological model that will be used, emphasis now lies on each of the state variables and how the physical model will be coupled to the biological model.

3.4 Coupling of the LES to the NPZ

Emphasis so far has been placed on how the flow has profound effect on the biological dynamics. However, it is also of primary interest how the flow affects the spatial variability of the biological fields and so a coupling of the physical and the biological will be encapsulated by means of an advection-diffusion equation (such as Mirbagheri et al. (2011); Pérez-Muñuzuri and Huhn (2010)) in the form

$$\frac{\partial \Gamma}{\partial t} + \mathbf{u} \cdot \nabla \Gamma = D_{\Gamma} \nabla^2 \Gamma + \text{Biological dynamics}, \quad (3.61)$$

where $\Gamma = N, P, Z$ and \mathbf{u} is the flow calculated in the LES simulation. The most important term here is the advection (or transport) term $\mathbf{u} \cdot \nabla \Gamma$. This term describes how the flow carries the biological fields Γ in space and is the main link in the model between the fluid flow and the biology.

In the biological model alone, the driving parameters are only depth dependant, due to dependence on the energy dissipation rate, $\langle \epsilon \rangle$, which is a depth dependant parameter. Therefore, if one wants to stimulate heterogeneity in the lateral domain, there is a need for a 3-dimensional driver, namely the flow field. Not only is the flow needed to make this model realistic, it is critical in initiating heterogeneity (even though it is possible that it could also be the cause of dispersing dense aggregations). That being said, it is apparent that for aggregations to manifest themselves, the level of mixing needs to be such that,

- (a) the level of turbulence is enough to initiate heterogeneity in the biological fields, via upwellings

(b) the level of turbulence is not too strong as to fully disperse aggregations.

Therefore, it follows that there will be some optimum level of vertical mixing (parametrised by the level of wind stress, U_*) which will give ideal conditions for plankton aggregations to thrive.

The diffusion term in equation 3.61 is standard except for the diffusion rate parameter D_Γ itself. The problem lies in the fact that the flow is resolved down to a scale of about 1 metre. If the diffusion rate is of a certain size then it could give information about the biology below that of the resolution scale which is prescribed in this model, which is an unreasonable construct. The diffusion parameter can be considered by means of the non-dimensional quantity, the Schmidt number Sc . This is given in the form,

$$Sc = \frac{\nu}{D}, \quad (3.62)$$

where ν is the viscosity of the water. This term can be thought of in the following way

$$\frac{\nu}{D_\Gamma} = \frac{\text{level of physical diffusion}}{\text{level of biological diffusion}}.$$

Diffusion is a small scale process. Therefore, the ratio of these two parameters will suggest the level of small scale spatial structure which the biology can achieve and sustain. So, as the Schmidt number increases, the scale at which aggregations can feasibly occur will decrease. A limit on this number will need to be imposed, dependant on the spatial resolution prescribed to the solution grid. If the Schmidt number is too high then we will have assumed there is small scale pattern formation below what will be observable in the simulation. In fact, if $Sc > 1$ then this would imply there is more structure in the biological fields than that of the velocity fields and so it makes sense to limit $Sc < 1$ (Lewis, 2005).

Setting a limit on the biological diffusion co-efficient has implications. It means that we could be prescribing a diffusion parameter which is lower than that in nature. It

is possible in nature that this higher diffusion rate which acts on small scales (which we won't include) that can feed back into the large scales. However, over the time scale we are looking at, it is arguable that this feedback would be negligible and so this limitation is not detrimental to the results.

Sullivan et al. (1994) suggest that Sc should be based on the resolution scale alone, they give this in the form

$$Sc = \frac{\nu}{D_\Gamma} = \frac{1}{1 + \frac{2L_0}{\Delta}}, \quad (3.63)$$

where $\Delta^3 = \frac{3\Delta x}{2} \frac{3\Delta y}{2} \Delta z$ and L_0 is a resolution scale. In our simulations, $\Delta \approx 2$ and $L_0 = 1$ giving $Sc = \frac{1}{2}$ which satisfies the limit imposed. As we know ν we now have our parameter D_Γ and can finally solve the NPZ-LES model given by

$$\begin{aligned} \frac{\partial N}{\partial t} + \mathbf{u} \cdot \nabla N &= D_N \nabla^2 N + \text{'N recycled from P'} - \text{'N uptake by P'}, \\ \frac{\partial P}{\partial t} + \mathbf{u} \cdot \nabla P &= D_P \nabla^2 P + \text{'P growth from N'} - \text{'P grazing loss from Z'}, \\ \frac{\partial Z}{\partial t} + \mathbf{u} \cdot \nabla Z &= D_Z \nabla^2 Z + \text{'Z growth from P'} - \text{'Z death'}. \end{aligned} \quad (3.64)$$

3.5 Table of Parameters

| Parameter | Description | Numeric Values | Units |
|------------------------|-------------------------------|-----------------------|-----------------------|
| P_0 | background P concentration | 5×10^6 | cells m^{-3} |
| Z_0 | background Z concentration | 2×10^4 | cells m^{-3} |
| N_0 | background N concentration | 2.8×10^{-5} | kg m^{-3} |
| β_E | P growth efficiency | 0.75 | |
| α | light attenuation coefficient | 0.04 | m^{-1} |
| μ_P^{\max} | maximum P growth rate | 1 - 10 | days $^{-1}$ |
| s_N | N stoichiometry coefficient | 2.7×10^{-14} | kg cells $^{-1}$ |
| R | Z contact radius | 2×10^{-3} | m |
| T_R | Z reaction time | 5 | s |
| μ_Z^{\max} | maximum Z growth rate | 0.86 | days $^{-1}$ |
| μ_Z^{death} | Z death rate | 0.35 | days $^{-1}$ |
| Y | Z yield from P | 0.003 | |

Sources: Fasham et al. (1990); Muelbert et al. (1994); Lewis and Pedley (2000)
 Lewis and Pedley (2001); Baird and Emsley (1999); Williams and Follows (1998)
 Bissinger et al. (2008); Hansen (1997); Richmond et al. (2013); Straile (1997)

Chapter 4

Model Analysis

When dealing with such a complicated coupled model, one must first have a deep understanding of the two models individually. This chapter will underline the key components in each of the models (physical and biological) before pressing on some ideas of the consequences of the coupling. This chapter will be devoted to validating the model and using standard techniques to give a robust model setup.

4.1 Flow Statistics

Turbulence, as discussed in chapter 2, is a very unpredictable process. However, in a scenario where a body of water is subjected to fixed boundary conditions, the flow patterns generated often exhibit certain quasi-steady characteristics (McWilliams et al., 1997; Sullivan and Patton, 2011b). This means that properties of the turbulent flow can be summarised by the levels of key parameters which prescribe the boundary conditions. In this work, the most important parameter controlling the physical boundary conditions is the friction velocity, U_* , which is essentially a measure of the local wind stress.

A fixed wind stress may not be a realistic construct in a wind-driven oceanic mixed layer model. However, it is important to try to understand the long term behaviour

of the model, subject to constant boundary conditions when the flow reaches a state of quasi-equilibrium. In this work we are interested in trying to understand when the physical conditions are conducive to the formation of planktonic patches. If the wind stress is too large and the mixing too strong, biological heterogeneities will be smoothed away (Huisman et al., 1999). But if the wind stress is weak, the level of mixing will be too low to advect nutrients into the euphotic zone and little biological production will be stimulated (Cloern, 1991; Peeters et al., 2013). Finding the right balance will be key to deciding when planktonic aggregation can occur.

In this work, simulations of the LES model were run for a number of different values of U_* , e.g. in the range $(0.5 - 6) \times 10^{-3} \text{ ms}^{-1}$. These values correspond to wind speeds of about $(0.5 - 5) \text{ ms}^{-1}$, measured 10 metres above the surface (Brown and Wolf, 2009). It was established in Chapter 2 that turbulence in an oceanic boundary layer is primarily depth dependant and so logically, analysing the depth dependence of the flow statistics should enable us to quantify the mixing capabilities of the flow. Figure 4.1 shows horizontal averages of the velocity component fields ($\langle u \rangle$, $\langle v \rangle$, $\langle w \rangle$), how they vary with depth and with U_* . With increasing wind stress, the ($\langle u \rangle$, $\langle v \rangle$) profiles increase in magnitude, which is as expected. $\langle w \rangle$ is negligible with depth, due to the boundary condition prescribing no vertical velocity at the surface and base of the mixed layer i.e.

$$\langle w \rangle|_{z=0,ml} = 0. \quad (4.1)$$

Due to the fact that water is incompressible, the net flux of water at a particular depth will be, by definition, zero (Sullivan and Patton, 2011a). This implies that the upwellings and downwellings of velocity must balance out at each given depth (averaged over the $x - y$ plane).

Variance statistics are important in the flow analysis as they give an indication of the amount of energy in the boundary layer. The larger the variance, the more energy the flow will contain (Denman and Platt, 1976; Rippeth et al., 2002). Figure 4.2 shows

a selection of velocity variance profiles with depth including the sensitivity of velocity variance, $\langle \mathbf{u}^2 \rangle$, to wind stress. As the wind stress increases, two things are apparent. When the wind stress is larger, the variance magnitude is, for the most part, larger. Secondly, the profiles of $\langle w^2 \rangle$ show there is a deeper penetration of the boundary layer, which means there is more energy deeper in the boundary layer. Penetration in this context refers to vertical circulation of fluid, if the boundary layer is fully penetrated, the fluid would circulate through all depths. The latter effect is more noticeable in the $\langle u^2 \rangle$ and $\langle w^2 \rangle$ terms. In figure 4.2(c) a distinctive peak between the shallow and mid region of the water column is observed. This peak is pushed deeper as the wind stress is increased. This means that the boundary layer is being penetrated deeper by the mixing mechanisms associated with the large eddies which are being set up, which is to be expected (Skylingstad and Denbo, 1995; Smith, 1992). This vertical mixing will be a key component in plankton bloom formations and will be discussed in more detail later in this work.

The energy dissipation rate, ϵ , is a good measure of the extent of the turbulent characteristics of the flow, as it shows how much kinetic energy is lost to heat energy (a more turbulent flow would have more kinetic energy to convert). It is of primary interest here for categorising those values of ϵ which are associated with a ‘strongly mixed’ turbulent regime (relative to the perspective of plankton aggregation). With increasing wind stress comes a bigger injection of energy into the flow, this can be observed via the energy dissipation rate (figure 4.3). There is a vast amount of energy near the surface waters in comparison to energy levels deeper in the boundary layer, so we would not expect aggregations at the surface. When thinking about turbulent mixing, we are primarily interested in $\langle \epsilon(z) \rangle$, as this gives an idea of the magnitude of turbulent mixing in all directions. The vertical extent of this mixing is also of great interest, as this will give insight into how the boundary layer is partitioned into turbulent and laminar layers. We can use $\langle w^2(z) \rangle$ to parametrise the vertical mixing component (Hogan et al., 2009). The mixing components $\langle \epsilon(z) \rangle$ and $\langle w(z)^2 \rangle$ are quantified in

the simulations relatively easily, however, quantifying their effects on the biology is not so straight forward. This complex interaction will be studied in detail in subsequent sections and in particular, a study of the intricate pairings of biological and physical parameters which will allow phytoplankton to reside and flourish in a turbulent boundary layer is the main focus of this work.

In general, if there is a numerical instability in the solutions, higher order statistics will be more sensitive than lower order statistics, as the instability will be $o(\epsilon_1^n)$, where ϵ_1 is an error term e.g. $\langle u_a \rangle = \langle u \rangle + \epsilon_1$, $\langle u_a^2 \rangle = \langle u^2 \rangle + o(\epsilon_1^2)$ etc, where u_a is the actual solution and u is the approximate solution calculated in the model. Therefore, careful analysis of the second order statistics will be carried out to check for badly behaved solutions. This is important for two reasons. First, we have assumed statistical stability in the derivation of the predation rate, second, the flow itself subjected to static boundary conditions should reach statistical stability (as will be discussed later). Therefore, if statistical stability is not observed, then it is solely due to numerical errors building up and not a property of the flow field.

4.2 Statistical Stability

A convenient aspect of some boundary layers subjected to fixed boundary conditions is the statistical stability associated (Lesieur et al., 1997; Su and Clemens, 2003; Yakhot et al., 1988). This stability is observed in many theoretical models and in particular, has been observed in confined channel flows (such as the model in this work) (Kim et al., 1987; Moin and Kim, 1982). The importance of this is significant, as the depth dependant profile of ϵ has to be calculated before being fed into the biological model. By statistical stability, we mean that certain ensemble or spatial averages (under the conditions of homogeneity and isotropy, these coalesce to the same measure (Servidio et al., 2011)) denoted by $\langle \cdot \rangle$, will remain approximately constant provided the boundary conditions driving the flow remain static (Eswaran and Pope, 1988). As

resolving the flow is computationally expensive, calculating $\langle \epsilon(z) \rangle$ at each time step will be an unreasonable extra cost to the simulation. Fortunately, because the flow spins up into a state of quasi-equilibrium, the profile of $\langle \epsilon(z) \rangle$, like those shown in figure 4.3, should not change significantly with time. Hence, before each simulation one can estimate a stationary profile of $\langle \epsilon(z) \rangle$, which can then be used to couple together the biology into the flow dynamics. Essentially, that means that for flow statistics,

$$\begin{aligned} \langle u_i(z, t) \rangle &\simeq \langle u_i(z, t + T) \rangle \\ \langle u_i(z, t)u_j(z, t) \rangle &\simeq \langle u_i(z, t + T)u_j(z, t + T) \rangle, \end{aligned} \tag{4.2}$$

for all $T > 0$ provided $t \geq t_e$, where t_e is a time at which the flow has incurred a period of spin up and relaxation into statistical equilibrium.

The flow fields generated by the LES fall into two categories. First there are shear turbulence boundary layers, in which the flow field is generated by the level of wind stress alone. Second, there are the Langmuir turbulence (Stokes-Ekman) boundary layers, generated by both the level of wind stress and wave forcing. Analysis of the lower-order statistical moments of the flow will be carried out to check for stationarity in each flow regime for increasing levels of wind stress. It is worth pointing out that not much work has gone into analysing flow statistics on biological time scales (e.g. on a scale of weeks) using LES, and so work done in this section will be difficult to find comparisons from the current literature.

4.2.1 Shear Turbulence (Ekman boundary layers)

The LES code used in this work was developed for atmospheric applications whereby the time-scales used were far smaller and the levels of turbulence were far greater. Testing the statistical stability of different flow regimes under biological time-scales is therefore critical as it will put the dynamic time-stepping regime under rigorous diagnostics to see if the turbulent regimes in this work are suitable for such dynamic time resolution.

Figure 4.4 shows, for an Ekman boundary layer, first order statistics are relatively well behaved for the most part. However, when second order statistics are analysed (figure 4.5), it is clear that the system is not well behaved as the time-series should remain constant, this behaviour is accentuated for smaller values of U_* . When analysing the statistics it was observed that all statistical moments at all depths diverge at the same time, therefore it is reasonable to analyse just a select few second order statistical moments for instability at a few different depths. All curves in figure 4.5 are scaled by their own maximum for comparison i.e. the curves in figure 4.5 are of the form,

$$\frac{\langle u^2(z, t_i) \rangle}{\max_i[\langle u^2(z, t_i) \rangle]}.$$

This error in the model is due to the time stepping regime being based on the levels of advection and diffusion (see Chapter 2). If higher levels of advection (and hence turbulence) are detected, then the time step will be decreased to account for this and at lower levels of turbulence, a larger time-step is permitted to enhance the efficiency of the simulations. Due to the code being initially adapted for higher levels of turbulence such as planetary boundary layers (atmospheric modelling), the time-stepping for low turbulence levels has not been accounted for. Developing time-stepping dynamics to account for low turbulence levels will not be worth investing time in as a simple time-step cap can be implemented to stabilise solutions.

It is clear that all Ekman boundary layer simulations are unreliable with the current time-stepping regime and so a decision needs to be made as to whether Ekman boundary layers are worth investigating, when a maximum time-step needs to be implemented to each simulation. When making this decision, we analysed the energy dissipation rate with and without wave forcing. This will give an idea about the amount of turbulence generated in each case. Figure 4.6 shows this comparison and highlights the order of magnitude difference between the different regimes.

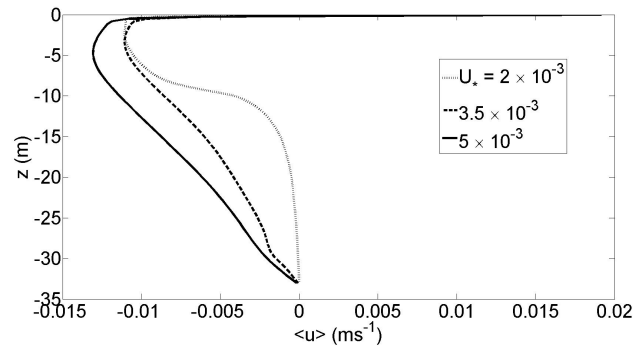
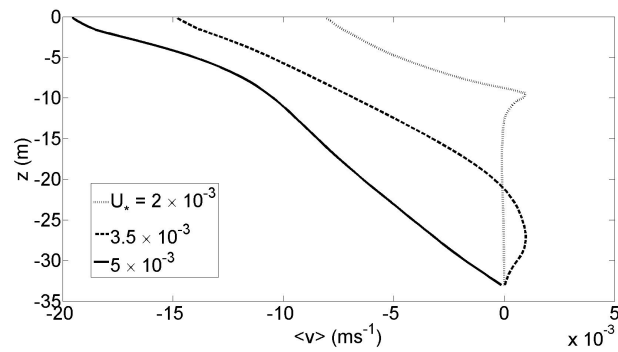
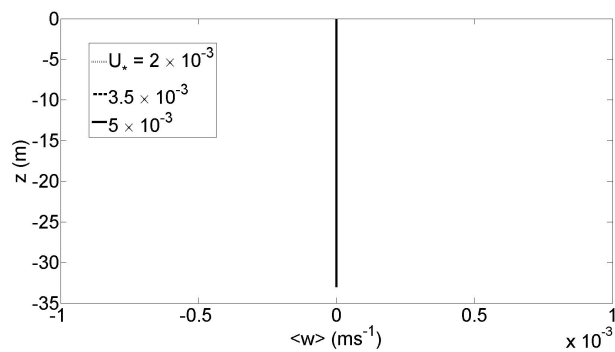
(a) $\langle u \rangle$ (b) $\langle v \rangle$ (c) $\langle w \rangle$

Figure 4.1: Graph of horizontally averaged velocity components, $\langle u \rangle$, $\langle v \rangle$ and $\langle w \rangle$ with depth. The dotted (fainter) line is the low wind stress ($U_* = 2 \times 10^{-3} \text{ ms}^{-1}$) case, the dashed line is for a moderate wind stress ($U_* = 3.5 \times 10^{-3} \text{ ms}^{-1}$) and the solid line is for a high wind stress ($U_* = 5 \times 10^{-3} \text{ ms}^{-1}$). All profiles are taken after the LES has incurred a spin-up and relaxation period so that solutions of statistical moments of the velocity components are statistically stable. These solutions were calculated from a Langmuir turbulence regime (i.e. include wave forcing).

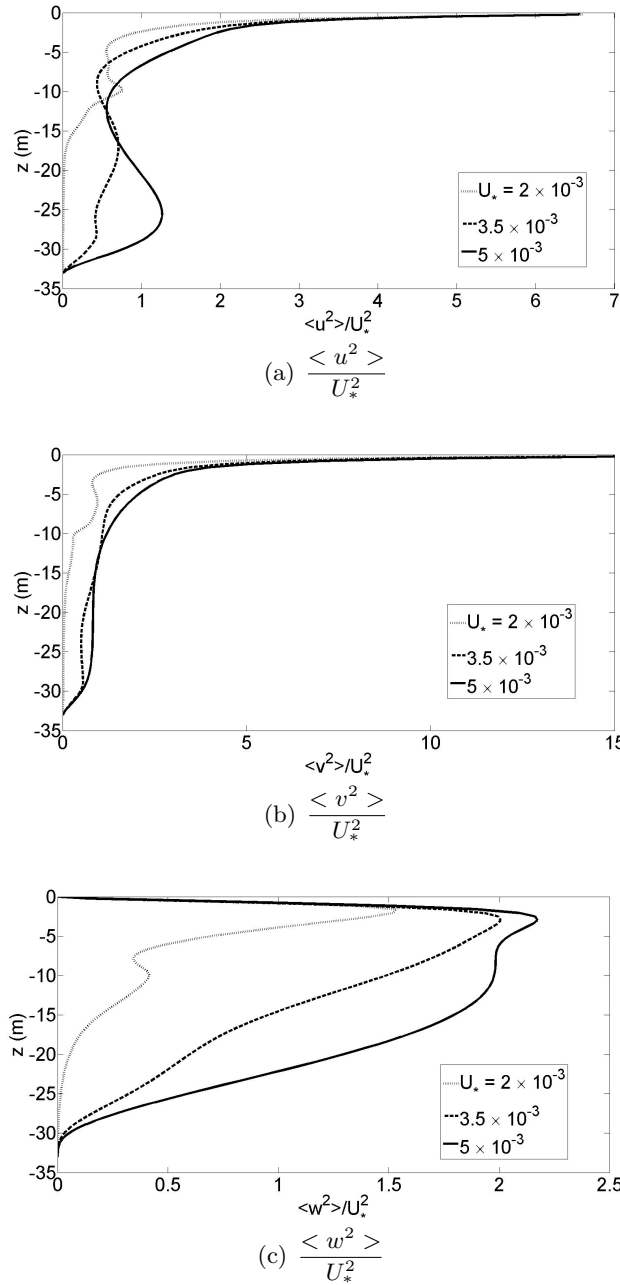


Figure 4.2: Graph of horizontally averaged velocity variance components (normalised by their respective wind stress value), $\frac{\langle u^2 \rangle}{U_*^2}$, $\frac{\langle v^2 \rangle}{U_*^2}$ and $\frac{\langle w^2 \rangle}{U_*^2}$ with depth. The dotted (fainter) line is the low wind stress ($U_* = 2 \times 10^{-3} \text{ ms}^{-1}$) case, the dashed line is for a moderate wind stress ($U_* = 3.5 \times 10^{-3} \text{ ms}^{-1}$) and the solid line is for a high wind stress ($U_* = 5 \times 10^{-3} \text{ ms}^{-1}$). These solutions were calculated from a Langmuir turbulence regime.

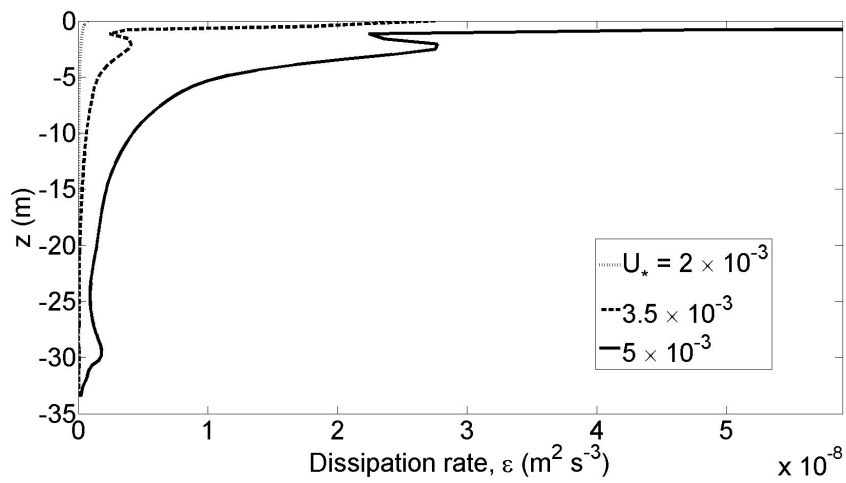


Figure 4.3: Depth profiles of the (horizontally averaged) energy dissipation rate, $\langle \epsilon \rangle$. The dotted (fainter) line is the low wind stress ($U_* = 2 \times 10^{-3} \text{ ms}^{-1}$) case, the dashed line is for a moderate wind stress ($U_* = 3.5 \times 10^{-3} \text{ ms}^{-1}$) and the solid line is for a high wind stress ($U_* = 5 \times 10^{-3} \text{ ms}^{-1}$). These solutions were calculated from a Langmuir turbulence regime.

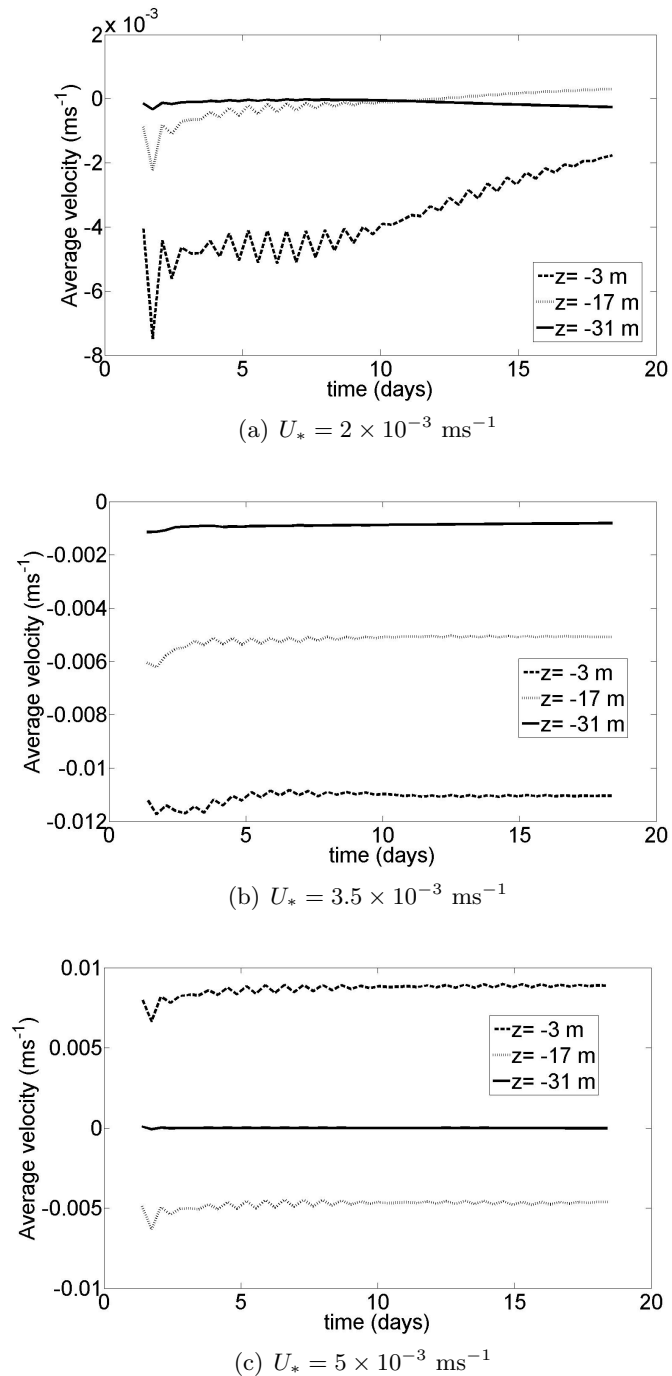


Figure 4.4: Graph of the average velocity, $\langle u \rangle$ and how it evolves in time to see if (first order) statistical stationarity is maintained. The dashed line is the velocity measured at 3 metres below the surface, the dotted (fainter) line is 17 metres below the surface and the solid line, 31 metres below the surface. A comparison was made between a low wind stress ($U_* = 2 \times 10^{-3} \text{ ms}^{-1}$), a moderate wind stress ($U_* = 3.5 \times 10^{-3} \text{ ms}^{-1}$) and a high wind stress ($U_* = 5 \times 10^{-3} \text{ ms}^{-1}$). These solutions were calculated from a shear turbulence regime (no wave forcing present).

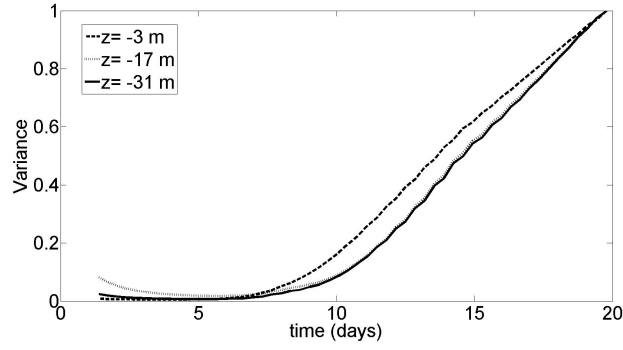
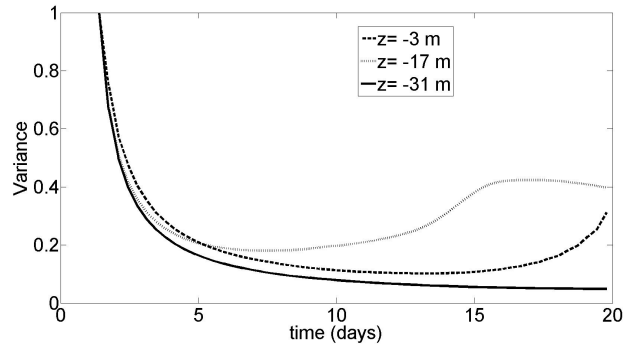
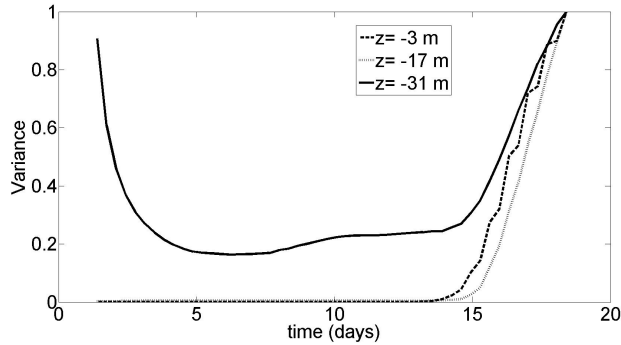
(a) $U_* = 2 \times 10^{-3} \text{ ms}^{-1}$ (b) $U_* = 3.5 \times 10^{-3} \text{ ms}^{-1}$ (c) $U_* = 5 \times 10^{-3} \text{ ms}^{-1}$

Figure 4.5: Graph of the average velocity variance, $\langle u^2(z, t_i) \rangle$ (normalised by its maximum $\max_i [\langle u^2(z, t_i) \rangle]$) and how it evolves in time to test if (second order) statistical stationarity is maintained. The dashed line is the velocity measured at 3 metres below the surface, the dotted (fainter) line is 17 metres below the surface and the solid line, 31 metres below the surface. A comparison was made between a low wind stress ($U_* = 2 \times 10^{-3} \text{ ms}^{-1}$), a moderate wind stress ($U_* = 3.5 \times 10^{-3} \text{ ms}^{-1}$) and a high wind stress ($U_* = 5 \times 10^{-3} \text{ ms}^{-1}$). These solutions were calculated from a shear turbulence regime.

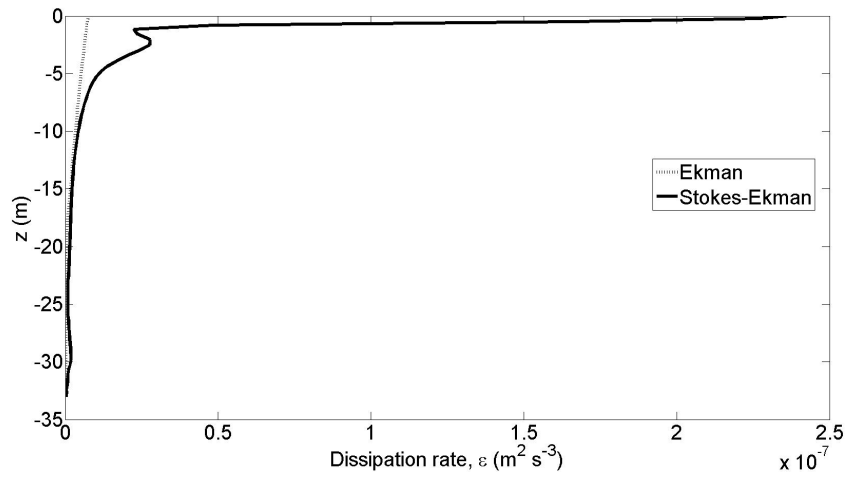


Figure 4.6: Depth profiles of the (horizontally averaged) energy dissipation rate for a fixed wind stress value of $U_* = 5 \times 10^{-3} \text{ ms}^{-1}$. This graph shows a comparison between energy associated with a boundary layer with wave forcing (solid line) and without (dotted line).

4.2.2 Langmuir Turbulence (Stokes-Ekman boundary layers)

Stokes-Ekman boundary layers are more turbulent than their Ekman counterpart and also penetrate in the boundary layer more effectively. This penetrating behaviour is widely observable in the Oceans and Seas (Weller, 1982). Therefore the time-stepping dynamics are more suited to these types of boundary layers as the LES is more suited to higher turbulence levels.

First order statistics reflect the increased suitability of the dynamical time-step as they all display a good level of stability, see figure 4.7. However, even with this increased stability, not all second-order statistics remain stationary. Figure 4.8 shows that most statistics are well behaved, but for the lower wind stress value (figure 4.8(a)), stability breaks down towards the end of the time scale. This demonstrates the reliability of this flow regime, but it also illustrates that it is not exempt from statistical instability at the lower levels of turbulence. Further testing of this lower wind stress was investigated with a time-step cap of $dt = 1s$ being implemented. Figure 4.9 shows the second order statistics of the flow with this increased time resolution. It displays a settling down period which is greater than what has been previously observed, but stability ensues in the simulation. This justifies the argument that the time-step alone is the reason for instability. Subsequent simulations incorporated a maximum time step of $dt = 1.5s$, a compromise value small enough to keep numerical instability to a minimum over biological time scales, but large enough to allow simulations to be completed in a reasonable time frame.

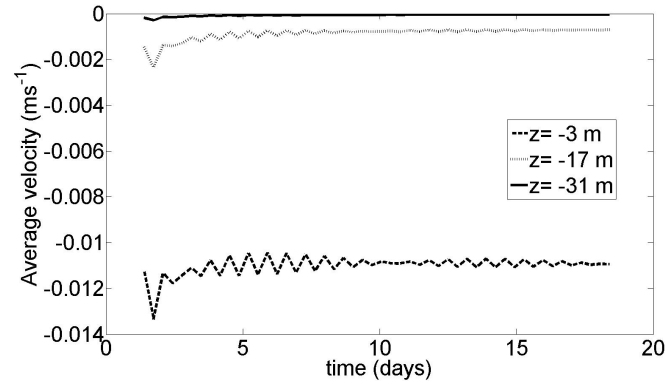
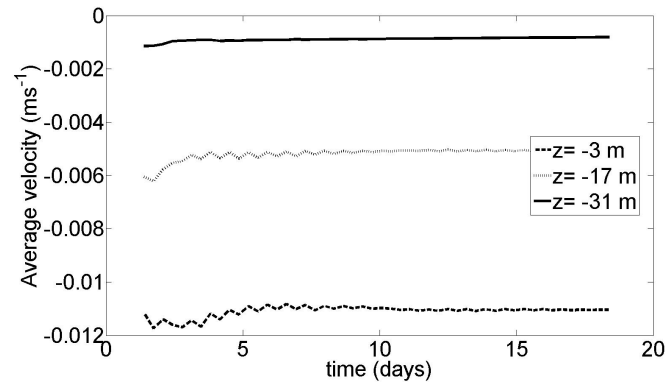
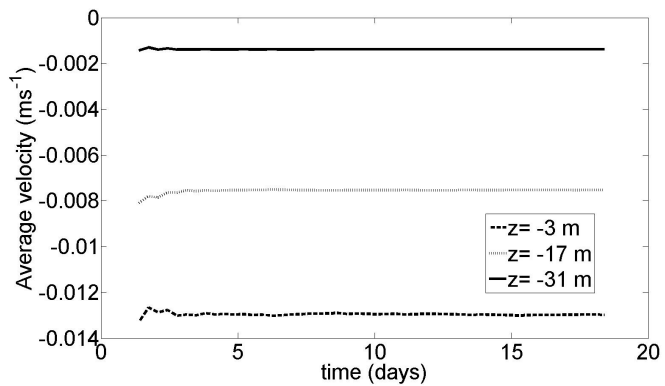
(a) $U_* = 2 \times 10^{-3} \text{ ms}^{-1}$ (b) $U_* = 3.5 \times 10^{-3} \text{ ms}^{-1}$ (c) $U_* = 5 \times 10^{-3} \text{ ms}^{-1}$

Figure 4.7: Graph of the average velocity, $\langle u \rangle$ and how it evolves in time to see if (first order) statistical stationarity is maintained. The dashed line is the velocity measured at 3 metres below the surface, the dotted (fainter) line is 17 metres below the surface and the solid line, 31 metres below the surface. A comparison was made between a low wind stress ($U_* = 2 \times 10^{-3} \text{ ms}^{-1}$), a moderate wind stress ($U_* = 3.5 \times 10^{-3} \text{ ms}^{-1}$) and a high wind stress ($U_* = 5 \times 10^{-3} \text{ ms}^{-1}$). These solutions were calculated from a Langmuir turbulence regime (wave forcing present).

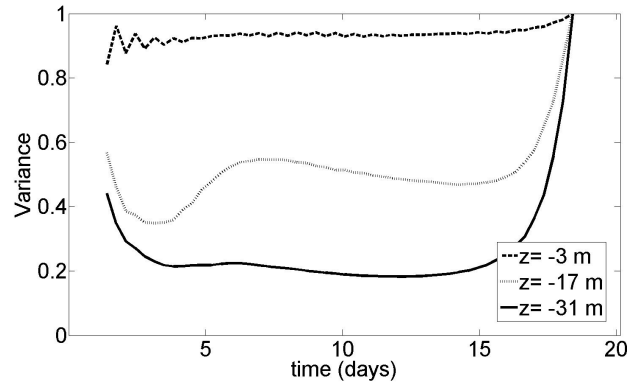
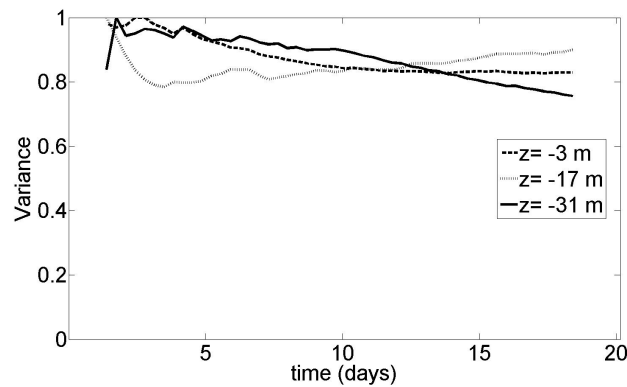
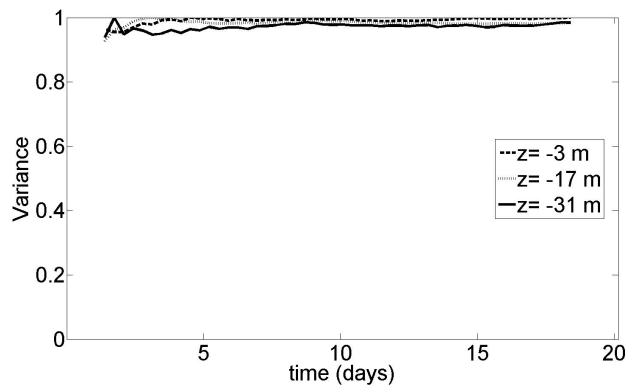
(a) $U_* = 2 \times 10^{-3} \text{ ms}^{-1}$ (b) $U_* = 3.5 \times 10^{-3} \text{ ms}^{-1}$ (c) $U_* = 5 \times 10^{-3} \text{ ms}^{-1}$

Figure 4.8: Graph of the average velocity variance, $\langle u^2(z, t_i) \rangle$ (normalised by its maximum $\max_i [\langle u^2(z, t_i) \rangle]$) and how it evolves in time, to see if (second order) statistical stationarity is maintained. The dashed line is the velocity measured at 3 metres below the surface, the dotted (fainter) line is 17 metres below the surface and the solid line, 31 metres below the surface. A comparison was made between a low wind stress ($U_* = 2 \times 10^{-3} \text{ ms}^{-1}$), a moderate wind stress ($U_* = 3.5 \times 10^{-3} \text{ ms}^{-1}$) and a high wind stress ($U_* = 5 \times 10^{-3} \text{ ms}^{-1}$). These solutions were calculated from a Langmuir turbulence regime.

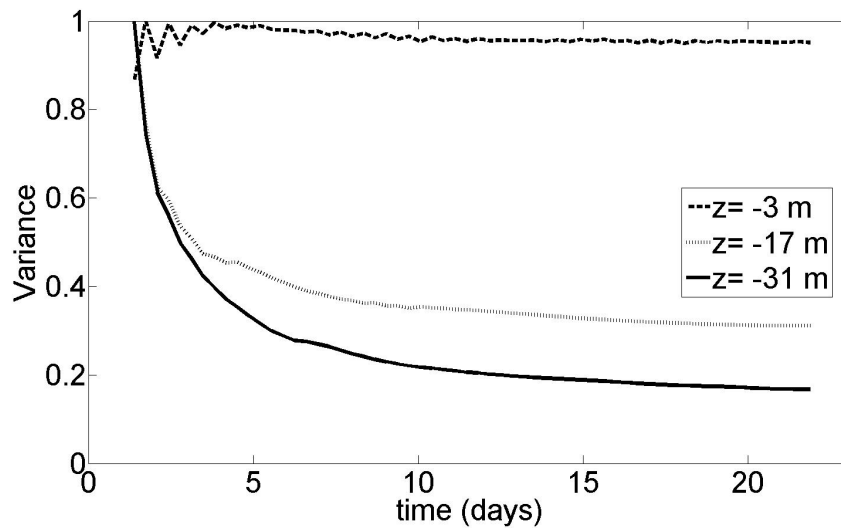


Figure 4.9: Graph of the average velocity variance, $\langle u^2(z, t_i) \rangle$ (normalised by its maximum $\max_i [\langle u^2(z, t_i) \rangle]$) and how it evolves in time to see if (second order) statistical stationarity is maintained. The dashed line is the velocity measured at 3 metres below the surface, the dotted (fainter) line is 17 metres below the surface and the solid line, 31 metres below the surface. This employs a timestep maximum of $dt_{max} = 1$ s for the low wind stress case of $U_* = 2 \times 10^{-3} \text{ ms}^{-1}$.

4.3 Effect of Wind on the Mixed Layer

As discussed in chapter 2, when wind blows over the surface of water, surface waves are produced. Naturally, water waves are complicated and so simplifications must be made if one wants to make use of analytical models.

4.3.1 Relationship Between Stokes Drift and Wind Speed

In this work, finding a relationship between the friction velocity, U_* and the stretching capabilities associated with the Stokes drift, U_s , is a crucial component as it is an integral part of the model and so previous work in the literature will be examined. There are many aspects to finding the relationship between U_s and U_* . For example, how far from the shore the water in question is and how developed the waves are. Here, we have a constant wind blowing over the surface with no deviation from this condition and so it is a good assumption to say that the surface waves will be fully developed. We also base our simulations out in the deep ocean, i.e. the distance to the shore will not play a significant role. With this criteria in mind, Komen (1994) suggest that for fully developed ocean waves, the relationship between the Stokes drift and the friction velocity is linear, i.e.,

$$U_* = A^2 U_s, \quad (4.3)$$

where $A \approx 0.21$ (Komen, 1994). However, subsequent papers (McWilliams et al., 1997; Li et al., 2005; Harcourt and D'Asaro, 2008; Sullivan et al., 2012) suggest $A = 0.3$ for fully developed ocean waves. It is usual that A is defined to be the turbulent Langmuir number, La_t and it is defined as

$$La_t = \sqrt{\frac{U_*}{U_s}}. \quad (4.4)$$

The Langmuir number is variable however in a fixed turbulent regime it will be approximately fixed. $La_t = 0.3$ will be kept for all subsequent simulations. Now that a relationship between U_s and U_* has been established, it is vital to explore the effect

what effect the wind stress has on the boundary layer.

4.3.2 Wind Penetration

The mixed layer refers to the upper ocean where temperature and density are homogeneous (Sanford et al., 2011). Wind drives the mixed layer (Martinez et al., 2011), so it is logical that a mixed layer depth would correspond to a certain wind speed and so with a constant wind stress, we would expect to see no mixed layer deepening or retreating. For this reason, a fixed mixed layer depth z_{ML} is employed. Without prior knowledge to the relationship between U_* and z_{ML} , we will simply choose a reasonable fixed value of $z_{\text{ML}} = 33$ m for all U_* (McWilliams et al., 1997). A fixed mixed layer depth is reasonable as the model still allows for localised wind driven mixing near the surface and laminar flow underneath, which is similar in construct to the partition between the mixed layer and the pycnocline (Jenkinson and Sun, 2011; Voropayeva and Chernykh, 2010), although density and temperature remain constant in this model.

A series of simulations were carried out to quantify how vertical mixing levels depend on local wind stress levels and to find how penetrative each wind regime is. By penetration, we are referring to the range of depths in which vertical mixing are significant. It is difficult to quantify this vertical mixing, so a simple measurement will be taken. This will analyse the average vertical velocity variance $\langle w^2 \rangle$ as this gives an approximate scale of the vertical mixing energy at each depth (Harcourt and D'Asaro, 2008). Finding the depth at which this energy is approximately half of the total energy will give a rough idea of how the energy is distribution across the mixed layer. This mid-energy depth \hat{z} can therefore be defined to satisfy

$$\int_{\hat{z}}^0 \langle w^2 \rangle dz = \int_{z_{\text{ML}}}^{\hat{z}} \langle w^2 \rangle dz, \quad (4.5)$$

and an approximate penetration depth z_{pen} can be defined to be twice this mid-energy depth i.e. $z_{\text{pen}} = 2\hat{z}$. This penetration depth is based on the assumption that $\langle w^2 \rangle$ is unimodal and so this needs to be checked before z_{pen} can be used. Figure 4.10 shows

a typical vertical velocity variance distribution, all profiles are approximately unimodal and skewed toward the surface as there is more energy near the surface and it is zero at the boundaries due to the no slip boundary conditions imposed.

Simulations were taken for a mixed layer of 33 metres and figure 4.11 shows the penetration depth and how it varies with wind stress. It was observed that for this value of z_{ML} , the penetration stops deepening once $U_* \approx 4 \times 10^{-3} \text{ ms}^{-1}$. This indicates that at this wind stress, the flow has become more or less fully developed. This means that vertical mixing is such that full circulation of the boundary layer water will be permitted. In the case where $U_* < 4 \times 10^{-3} \text{ ms}^{-1}$, a partition between the turbulent upper layer and the laminar lower layer will be more apparent. This partitioning behaviour will be preferential for planktonic aggregation for two reasons. First, plankton are going to be more likely to aggregate in regions where turbulent mixing is low as they will not be dispersed by the flow. Second, for thinner distinct bands of laminar flow, thin (depth-wise) layers of biological aggregations will be likely to manifest themselves.

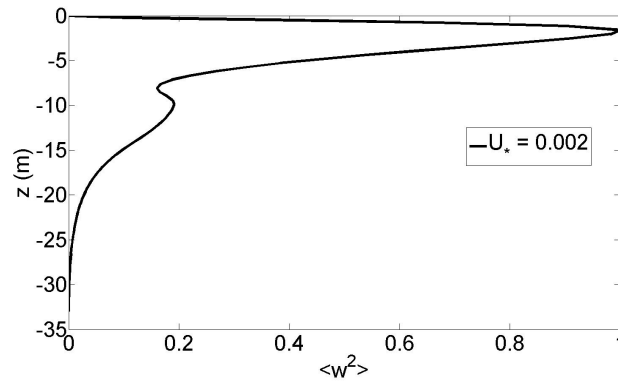
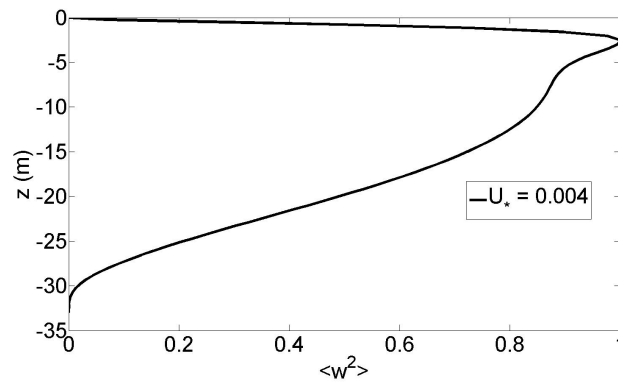
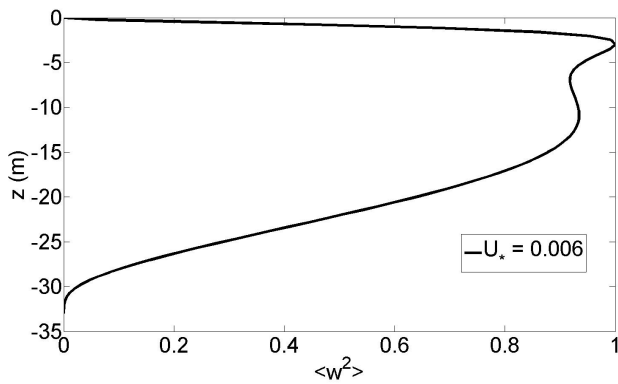
(a) $U_* = 2 \times 10^{-3} \text{ ms}^{-1}$ (b) $U_* = 4 \times 10^{-3} \text{ ms}^{-1}$ (c) $U_* = 6 \times 10^{-3} \text{ ms}^{-1}$

Figure 4.10: Profile of the average vertical velocity variance $\langle w^2(z) \rangle$ with depth (normalised by its maximum $\max[\langle w^2(z) \rangle]$). A comparison was made between a low wind stress ($U_* = 2 \times 10^{-3} \text{ ms}^{-1}$), a moderate wind stress ($U_* = 4 \times 10^{-3} \text{ ms}^{-1}$) and a high wind stress ($U_* = 6 \times 10^{-3} \text{ ms}^{-1}$) to examine profiles for unimodality.

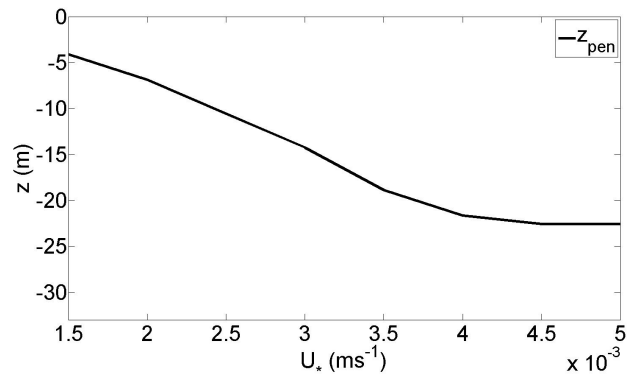


Figure 4.11: Relationship between the levels of wind stress, U_* , subjected to the boundary and the penetration depth, z_{pen} , associated.

4.4 Analysing the NPZ Equations

The LES-NPZ model proposed in this work is a robust model in that it captures the fluid motion in the flow reasonably well. It also captures the turbulent effects on the biology. Modelling with this amount of complexity however, does have its drawbacks. The complicated set of equations that are being utilised do not (as of yet) yield any analytical solutions and any (linear) stability analysis cannot be performed due to the non-linear nature of the model. However, as in most analysis, if a solution cannot be found, then one must strip layers of complexity from the model equations until analysis can be carried out (with reasonable trepidation). This method can give insight, at least on a qualitative level, to the nature of the more complex model. This technique of simplification also has the advantage of being computationally inexpensive (and hence less time for simulations to complete) for numerical solutions to be found and so can make analysis of the LES-NPZ model much more efficient.

4.4.1 Reducing the LES-NPZ Model for Simple Analysis

When thinking about simplifying the LES-NPZ model, thought must go into the obstacles that stand in the way of analysing the model. The first thing that is abundantly clear is that stability analysis of the full Navier-Stokes equations will be fruitless due to the non-linear behaviour of the system and so the first systematic approach will be to remove the physical aspects of the flow i.e. \mathbf{u} and ϵ . This process of elimination removes the large, spatially dependant term $\mathbf{u} \cdot \nabla \Gamma$ and so analysing the diffusion term (the small spatially dependant term) will be pointless in this analysis. This then leaves a simple set of equations which vary only in time and so will be relatively simple to

analyse. These equations are as follows,

$$\begin{aligned}\frac{dN}{dt} &= fP - gNP, \\ \frac{dP}{dt} &= aPN - bPZ, \\ \frac{dZ}{dt} &= cPZ - eZ,\end{aligned}\tag{4.6}$$

where a - Phytoplankton growth from Nitrate, b - Grazing loss from Zooplankton, c - Zooplankton growth from Phytoplankton, e - Zooplankton death rate, f - Nitrate loss from Phytoplankton, g - Nitrate recycled from Phytoplankton. Note, although in the model the equation for $\frac{dN}{dt}$ has a quadratic dependence on N in the nitrate recycled term, f and g are relatively small and so this simplification is reasonable and will not change any results drastically, although the analysis for the quadratic case is given in Lewis and Brereton (2013). These equations are now in a preferential form for analysing their stability properties. This analysis will not give actual solutions to the given problem, however it will give good approximations to the general dynamics. As solutions take weeks to produce in the LES-NPZ model, parameter searches are cumbersome and inefficient, whereas parameter searches in the simple model can be completed in seconds. Although this system can be non-dimensionalised to yield a more efficient scan of the parameter space, results from this exercise will be used for qualitative purposes only and a small selection of parameters will be subject to analysis.

4.4.2 Stability Analysis

The following stability analysis is taken from the simple model analysis explored by Lotka (1920) and Volterra (1926) and countless others (for example Harrison (1979); Ikeda and Šiljak (1980); Sih (1987)). To analyse stability of a particular system, one must first find points of equilibrium. These points will then be analysed to see if they attract or repel solutions. An equilibrium point is defined as a solution that does not change with time, this can be thought of simply as a system where all time derivatives

are zero at the equilibrium value i.e.,

$$\left. \frac{d\Gamma}{dt} \right|_{\Gamma=\Gamma^*} = 0, \quad (4.7)$$

where $\Gamma^* = (P^*, Z^*, N^*)$ and $(\cdot)^*$ indicates an equilibrium point. Finding equilibrium values of the simple model is straight forward. The system in equilibrium satisfies the (steady-state) set of equations,

$$\begin{aligned} aP^*N^* - bP^*Z^* &= 0 \\ cP^*Z^* - eZ^* &= 0 \end{aligned} \quad (4.8)$$

$$fP^* - gP^*N^* = 0,$$

which yields the following equilibrium points

$$\Gamma_{ce}^* = (P_{ce}^*, Z_{ce}^*, N_{ce}^*) = \left(\frac{e}{c}, \frac{af}{bg}, \frac{f}{g} \right) \quad (4.9)$$

and

$$\Gamma_{ex}^* = (P_{ex}^*, Z_{ex}^*, N_{ex}^*) = (0, 0, N^*), \quad (4.10)$$

where Γ_{ce}^* is the co-existence equilibrium, and Γ_{ex}^* in the extinction equilibrium. Now that equilibrium points have been found, their stability properties can be analysed. To do this, the Jacobian matrix of the system must be found (this matrix is a system of first order partial derivatives which represent the first order (linear) terms of the Taylor expansions), this is defined as $J_{ij} = \frac{\partial f_i}{\partial \Gamma_j}$ where $f_i = \frac{d\Gamma_i}{dt}$. This is explicitly represented by

$$J(P, Z, N) = \begin{pmatrix} aN - bZ & -bP & aP \\ cZ & cP - e & 0 \\ f - gN & 0 & -gP \end{pmatrix}. \quad (4.11)$$

We now need to use this to analyse each equilibrium point as it is possible that each equilibrium point has an effect on the trajectories of the biological fields. For each equilibrium point, we have associated Jacobian matrices

$$J_{ce}^*(P_{ce}^*, Z_{ce}^*, N_{ce}^*) = \begin{pmatrix} 0 & -\frac{be}{c} & \frac{ae}{c} \\ \frac{acf}{bg} & 0 & 0 \\ 0 & 0 & -\frac{eg}{c} \end{pmatrix} \quad (4.12)$$

and

$$J_{ex}^*(P_{ex}^*, Z_{ex}^*, N_{ex}^*) = \begin{pmatrix} aN_{ex}^* & 0 & 0 \\ 0 & -e & 0 \\ f - gN_{ex}^* & 0 & 0 \end{pmatrix}. \quad (4.13)$$

By solving the associated characteristic equation for each equilibrium state,

$$\det(J^* - \lambda I) = 0$$

where λ is the eigenvalue of the system, we find the following eigenvalue solutions,

$$J_{ce}^* : \lambda = -\frac{eg}{c}, \pm i \sqrt{\frac{aef}{g}} \quad (4.14)$$

and

$$J_{ex}^* : \lambda = 0, -e, aN_{ex}^*. \quad (4.15)$$

Taking into account that all parameters are positive, this implies that Γ_{ce}^* is oscillatory. One mode attenuates over a time period proportional to that of $\frac{c}{eg}$. The other modes are oscillatory with angular frequency $\sqrt{\frac{aef}{g}}$. Γ_{ex}^* is unstable. This not to say that dynamics can be determined by examining the stability of each equilibrium point separately, emphasis instead should lie on the fact that if the system is oscillatory, then the trajectories have the possibility of going between each point and so an interplay between the two stability regions may take place.

This is a complex system and changing most parameters will have an effect on both the equilibrium state and the stability and so making a choice about which parameters should be explored in the system must come under careful consideration. For this work, the trajectories of the phytoplankton field is of greatest interest and so the eigenvectors for each equilibrium region must be examined. By solving

$$(J_{ce}^* - \lambda_i I) \mathbf{v}_{ce, i}^* = \mathbf{0} \quad (4.16)$$

and

$$(J_{ex}^* - \lambda_i I) \mathbf{v}_{ex, i}^* = \mathbf{0}, \quad (4.17)$$

where \mathbf{v}_i is an eigenvector corresponding to λ_i for $i = 1, 2, 3$, we can generate linearised trajectories around each equilibrium point (the algebra of finding each eigenvector associated with P is omitted due to it being untidy, but see table below for approximate parameter values).

| Parameter | Numeric Values | Units |
|--|----------------|--------------------|
| $P_0 = P(0)$ | 0.5 | |
| $Z_0 = Z(0)$ | 0.5 | |
| $N_0 = N(0)$ | 1 | |
| a | 0.51 | days ⁻¹ |
| b | 1.2 | days ⁻¹ |
| c | 0.9 | days ⁻¹ |
| e | 0.34 | days ⁻¹ |
| f | 0.008 | days ⁻¹ |
| g | 0.016 | days ⁻¹ |
| m | 0.19 | days ⁻¹ |
| Approximate values calculated from table 3.5 | | |

Neglecting small parameter values, phytoplankton concentration trajectories are given by

$$\begin{aligned} \text{at } : \Gamma_{ce}^* \quad P(t) = P_{ce}^* - \frac{N_0 e g^2}{c^2 f} e^{-\frac{egt}{c}} + \left[(P_0 - P_{ce}^*) + \frac{N_0 e g^2}{c^2 f} \right] \cos(mt) \\ + \left[\frac{be}{cm} \left(\frac{aN_0}{b} - Z_0 \right) \right] \sin(mt) \end{aligned} \quad (4.18)$$

and

$$\text{at } \Gamma_{ex}^* : \quad P(t) = P_0 e^{aN_{ex}^* t} \quad (4.19)$$

where P_0 , Z_0 and N_0 are initial conditions and $m = \sqrt{\frac{aef}{g}}$. Note that the “extinction” equilibrium point is unstable and the phytoplankton population will always bounce back. In the short term $e^{-\frac{egt}{c}} \approx \cos(mt) \approx 1$, which reduces equation 4.18 to

$$\text{at } : \Gamma_{ce}^* \quad P(t) = P_{ce}^* + [P_0 - P_{ce}^*] \cos(mt) + \left[\frac{be}{cm} \left(\frac{aN_0}{b} - Z_0 \right) \right] \sin(mt). \quad (4.20)$$

Equation 4.20 gives some insight into how the phytoplankton population will develop. The magnitude of the fluctuations can be analysed by the factors in front of the sin and cos terms. As we cannot feasibly analyse the full parameter space, we will pick a select couple of parameters to examine which will give the most influence in the system. Arguably, a and N ($\approx N_0$ and N_{ex}^*) will give the most interesting information as they influence both of the equilibrium points. Analysis of the initial conditions will also be carried out to find the sensitivity of the system to these.

To begin analysing the trajectories of the biological fields, a base case, using parameters from experimental data will be used as a guide (approximated from the table of parameters in section 3.5). Figure 4.12 shows the dynamics of all 3 biological fields. The zooplankton field has a similar oscillation pattern as that of the phytoplankton field but with an added time lag which is to be expected. The nutrient field declines slowly in the time frame. This can give us some expectation as to what we might expect in the LES-NPZ model dynamics.

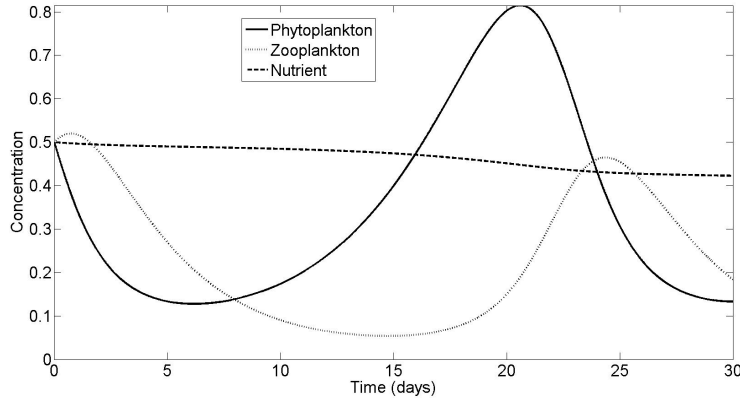


Figure 4.12: Dynamics of the simplified NPZ model using a base case parameter set in the table of parameters above. The solid line shows the concentration of phytoplankton, the dotted (fainter) line shows the zooplankton concentration and the dashed line shows the nutrient concentration.

4.4.3 Near Extinction Behaviour

Near extinction behaviour in planktonic species is very common, for example the north Atlantic spring bloom (Lancelot and Billen, 1984; Mahadevan et al., 2012; Song et al., 2010) which lasts for around 1 month and then the population seemingly dies and then re-emerges a year later to repeat the cycle. If we are to simulate reasonable dynamics of a plankton bloom, then this (near) extinction behaviour should be apparent. One of the limiting factors to picking up annual blooms in our model is time constraints imposed due to limitations in computing power. Annual blooms can simply not be modelled at the expense of the resolution of the flow field and so blooms will be modelled on a time scale of weeks. Note, however, that the annual variability will not be modelled in this work, as this is far too unrealistic to capture.

At a near extinction phase, the population falls to a minimum value $P_{\text{nex}} > 0$. Now as a (or N_0) increases, the amplitude of the oscillations increase which drives $P_{\text{nex}} \rightarrow 0$ as $a \rightarrow \infty$. At this time, the solutions are very close to the extinction equilibrium point, in which case the analysis looked at earlier will apply. So we have seen that the

P population recovers from P_{nex} following the equation $P \approx P_{\text{nex}} e^{aP_{\text{ex}}^* t}$. So now the recovery phase is driven faster by larger values of a . It is the complex interaction of the decay and recovery phases that determine how long the P population remains close to zero. Numerical simulations, figures 4.13 and 4.14 show that the near extinction phase is extended for large a and N_0 .

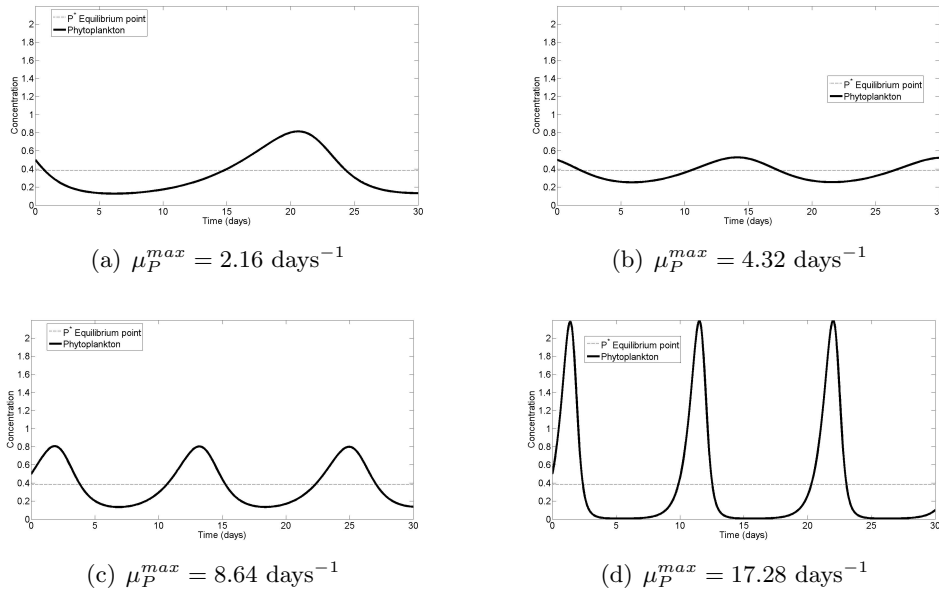


Figure 4.13: Dynamics of the (normalised) phytoplankton concentration (solid line) in a time period of a month. The dotted line shows the phytoplankton co-existence equilibrium value P_{ce} . The dynamics were compared for maximum phytoplankton growth rates of $\mu_P^{max} = (2.16, 4.32, 8.64, 17.28) \text{ days}^{-1}$.

Initial conditions in this system must be chosen carefully as we do not want to influence the system too much by choosing some unrealistic values which are far away from equilibrium. The influence of P_0 is shown in figure 4.15. As P_0 is increasing, extinction time is massively increasing, quickly rendering results useless in the time frame. Therefore, the initial condition of the P concentration will be chosen such that it is within 50% of P_{ce}^* . Therefore, a value of $P_0 = 0.5$ will be chosen for all subsequent simulations. Choosing a value close to equilibrium will also give an untarnished view

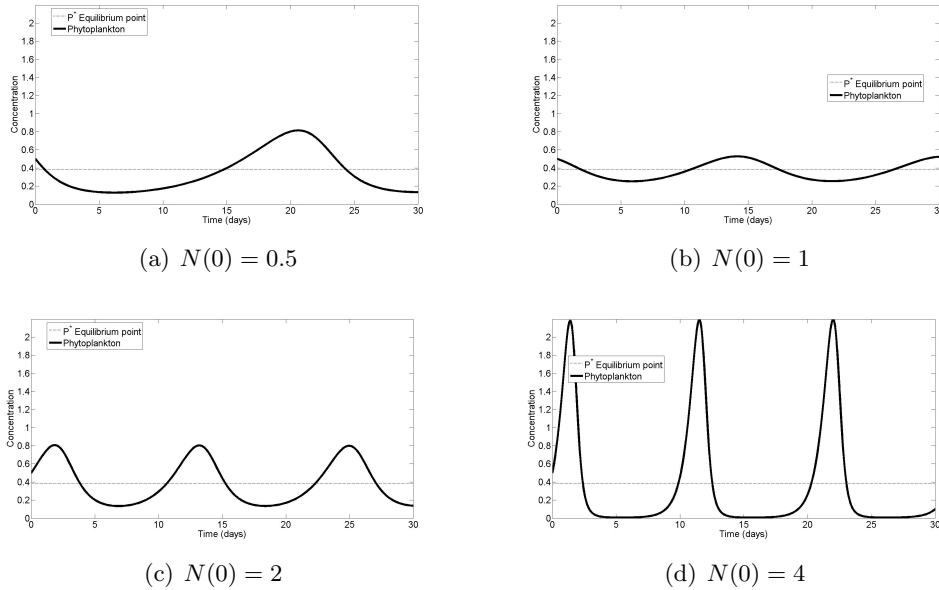


Figure 4.14: Dynamics of the (normalised) phytoplankton concentration (solid line) in a time period of a month. The dotted line shows the phytoplankton co-existence equilibrium value P_{ce} . The dynamics were compared for initial (normalised) nutrient concentrations of $N_0 = (0.5, 1, 2, 4)$.

on how the biological parameters effect the system. $P_0 = 0.5$ is also a realistic concentration as it is well within an order of magnitude of the background concentration value, which was used to normalise P^* (i.e. $P = 1$ gives a reasonable background concentration). The actual choice of the initial condition has no biological significance; all that is required is regular oscillations with a frequency of at least 2 cycles within a feasible simulation time (≈ 3 weeks).

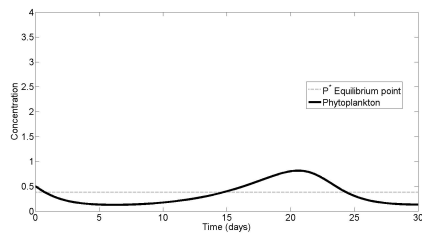
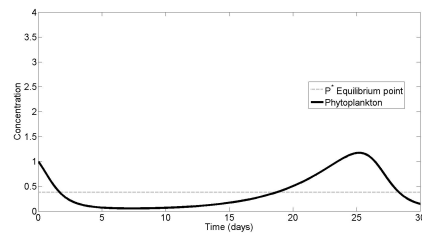
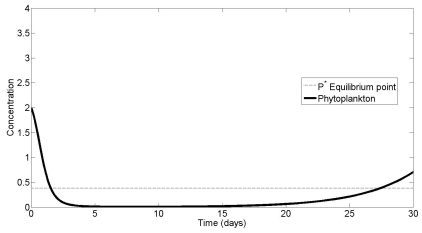
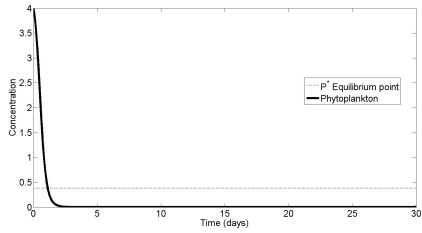
(a) $P(0) = 0.5$ (b) $P(0) = 1$ (c) $P(0) = 2$ (d) $P(0) = 4$

Figure 4.15: Dynamics of the (normalised) phytoplankton concentration (solid line) in a time period of a month. The dotted line shows the phytoplankton co-existence equilibrium value P_{ce} . The dynamics were compared for initial (normalised) phytoplankton concentrations of $P_0 = (0.5, 1, 2, 4)$.

4.5 Wind Stress Effect on Biology

Previously, we found that increasing wind stress results in an increase in energy dissipation, vertical mixing and deeper penetration of the boundary layer. How this increase in energy into the flow effects biological concentrations is crucial in the understanding of aggregate formations.

Turbulent mixing is a depth dependant process, so investigating how different levels of turbulence effect the biological concentration in terms of depth will be the first step in this analysis. The effect on biological concentrations can also aid in understanding the fluid dynamics of the boundary layer, because the biological concentrations are essentially passive tracers (discussed in this section).

4.5.1 Phase Locking

The biological concentrations used in this model are biologically active passive tracers. This means they can grow (in-situ), but never move in space on their own accord (except through slow diffusion). This is convenient for flow analysis, as it will give information about the level of mixing. For example, if the average concentration of phytoplankton was approximately the same as the phytoplankton concentration at all other depths and stayed that way over the time period, then we could infer mixing was strong as everything looks the same across all depths. This ‘phase locking’ is also important as it will give an indication to levels of wind stress which will completely mix biological concentrations, which will enable us to refine the parameter space for wind stress, as we will know not to analyse wind stress values that are certain to fully mix the biology.

Inferring that lateral aggregations cannot form when the biology is phase locked (depth-wise) is a fair assumption, but one which will be pressed upon in the next chapter. Figure 4.16 demonstrates the process of phase locking when levels of wind stress are

increased. The sudden change from (depth-dependant) heterogeneity to homogeneity indicates that there is a critical value of wind stress which causes this to happen. To try to quantify this level heterogeneity, we will use the following metric,

$$I_z(U_*) = \frac{1}{MN} \sum_{j=1}^N \sum_{i=1}^M \frac{(\langle P(z_i, t_j) \rangle - \bar{P}(t_j))^2}{(\bar{P}(t_j))^2}, \quad (4.21)$$

where $\bar{P}(t_j) = \frac{1}{M} \sum_{i=1}^M \langle P(z_i, t_j) \rangle$, $\langle \rangle$ denotes an average taken over the lateral domain, t_N is the total simulation time and $z_M = z_{ML}$. This metric I_z , will give an indication of the (normalised) variance between concentrations over all depths for a given wind stress value. Although I_z may change with different biological parameters, it is most likely to be primarily governed by the physical forcing. Figure 4.17 shows that when the wind stress is increased, I_z plummets after a particular value between $U_* = (3.5, 4) \times 10^{-3} \text{ ms}^{-1}$, which indicates that the boundary layer is being fully penetrated between these value. This is consistent with the hypothesis that the boundary layer is being penetrated when the penetration depth z_{pen} (figure 4.11), stops decreasing (significantly) and appears to approach a stationary value. As the wind stress is increased, phytoplankton concentration appears to be averaged out across all depths, i.e. $\sum_{i=1}^N P(z_i, t, U_*)$ is the same for all U_* (note however that the dynamics will change slightly as some biological parameters are directly related to U_*).

This is however only half of the argument as the lateral fields have not yet been analysed for heterogeneity, but it would be logical that if the boundary layer is being well mixed throughout all depths, then it would also be well mixed throughout the lateral domain. We will explore the dynamics of the lateral heterogeneity in the next chapter.

4.5.2 Thin Phytoplankton Layers

Phytoplankton aggregations have been observed and modelled for decades, however, in light of recent improvements in experimental apparatus, which can measure fine scale features of phytoplankton blooms very accurately, it has come to light that

a common characteristic of blooms is the small depth span. They can span a vast distance (km's) and yet their vertical extent may be $O(10\text{ cm})$ (Sullivan et al., 2010b). They also appear deeper in the boundary layer, ($< 5\text{ m}$) (Cheriton et al., 2009).

For aggregations to be permitted, they must avoid the high levels of vertical mixing near the surface, but there must be enough vertical mixing that nutrients can be brought up to the region they are in (Hu et al., 2011; Cloern, 1991). This middle ground seems a reasonable mechanism for thin layers of phytoplankton aggregations to form and will be the main mechanism to be examined in this work. We have found that there is a particular wind stress value which mixes the entire phytoplankton population in the model. Further to this, we will examine how wind stress values below this critical wind stress impact the depth dependence of the biology. Figure 4.18 shows how $\langle P(z, t) \rangle$ varies with depth at a select number of times. For $U_* = 2 \times 10^{-3}\text{ ms}^{-1}$ (figure 4.18(a)) phytoplankton concentrations are out of phase at most depths, with only the top 5 metres in phase. For a moderate wind speed of $U_* = 3.5 \times 10^{-3}\text{ ms}^{-1}$ (figure 4.18(b)), the majority of depths are phase locked and biological concentrations are only permitted to be out of phase at the bottom 10-15 metres. Figure 4.18(c) indicates that for a wind stress above the critical value, the whole concentration field is phase locked as all concentrations are the same at all depths. As a postulation, it will be likely that in the phase locked regions of the boundary layer, biological concentrations will be well mixed and so no aggregations are likely to occur in these regions. This means that aggregations will occur below the phase locked region and as the wind stress is increased, aggregations will occur deeper in the boundary layer.

Thought now needs to be given in the quantification of these thin layers within the model set-up. There are many definitions in the literature for thin layers, one for example is that the average concentration in the layer should be 3 times the background and the vertical extent must not exceed 5 metres (Durham and Stocker, 2012). Using average $\langle P \rangle$ concentrations is tempting to feed into the criteria, however this should

not be used for the following reasons. Firstly, thin layers are not likely to be a result of the biology being out of phase, as thin layers usually reside at a fixed depth (Rines et al., 2010) and an out of phase concentration will give thin layers over a number of depths e.g. figure 4.18(a). Secondly, it doesn't use the laterally heterogeneous distributions of phytoplankton, which will give a more detailed description of the aggregation and how intense the aggregation is.

Average concentrations of phytoplankton give great insight into the aggregation mechanism, however more information is needed if one wants to give an accurate description of the mechanics and dynamics of these aggregations. Next, we will examine how the lateral domain of concentrations is affected with different levels of wind stress and how this extra information can improve the picture of what is permitting phytoplankton to aggregate.

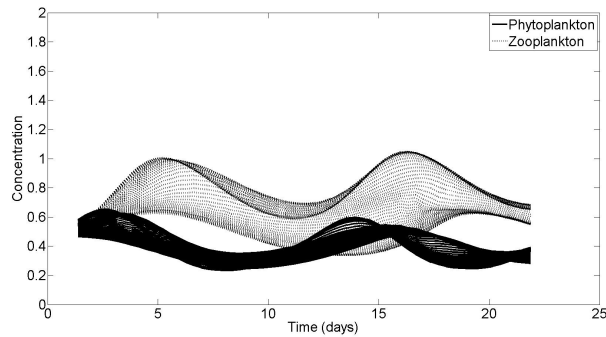
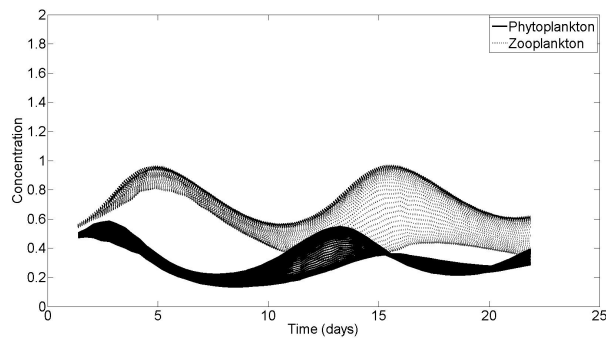
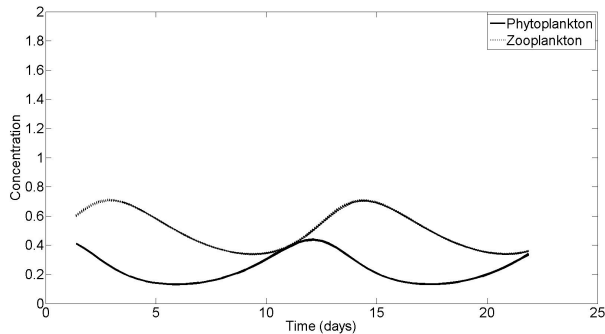
(a) $U_* = 2 \times 10^{-3} \text{ ms}^{-1}$ (b) $U_* = 3.5 \times 10^{-3} \text{ ms}^{-1}$ (c) $U_* = 5 \times 10^{-3} \text{ ms}^{-1}$

Figure 4.16: Dynamics of the phytoplankton and zooplankton concentration calculated from the LES-NPZ model at every depth. The solid lines shows the phytoplankton concentrations at all depths and the dotted (fainter) lines show the zooplankton concentrations at all depths (note that zooplankton concentrations are the larger of the two). A comparison was made between a low wind stress ($U_* = 2 \times 10^{-3} \text{ ms}^{-1}$), a moderate wind stress ($U_* = 3.5 \times 10^{-3} \text{ ms}^{-1}$) and a high wind stress ($U_* = 5 \times 10^{-3} \text{ ms}^{-1}$), which serves to illustrate the ‘phase locking effect’. Parameter values are analogous to those used generate figure 4.12.

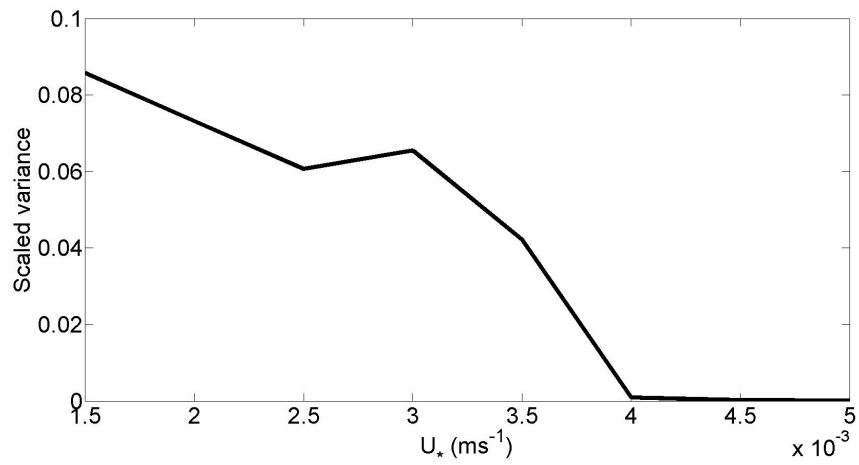


Figure 4.17: Relationship between the levels of wind stress subjected to the boundary layer and the levels of (normalised) variance between phytoplankton concentrations at each depth, averaged over time (I_z).

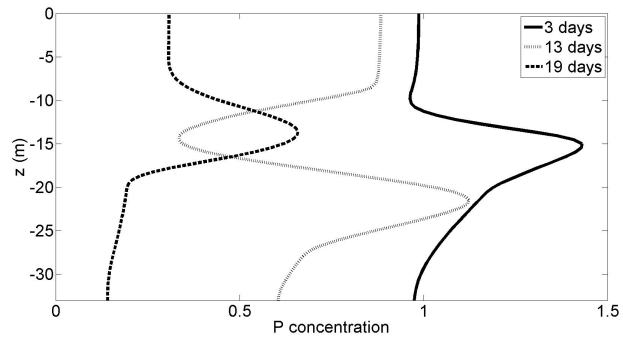
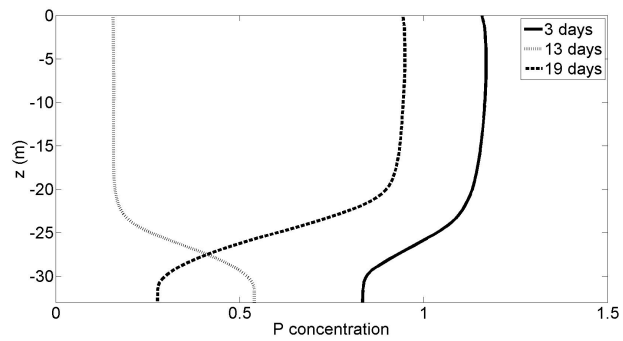
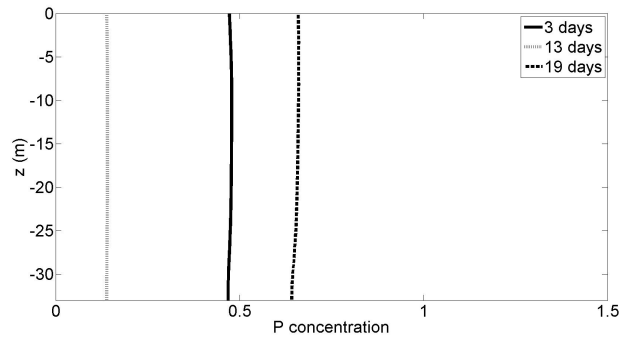
(a) $U_* = 2 \times 10^{-3} \text{ ms}^{-1}$ (b) $U_* = 3.5 \times 10^{-3} \text{ ms}^{-1}$ (c) $U_* = 5 \times 10^{-3} \text{ ms}^{-1}$

Figure 4.18: Profiles of average phytoplankton concentrations over all depths. The solid line shows the profile after 3 days, the dotted (fainter) line shows the profile at 13 days and the dashed line shows the profile at 19 days. A comparison was made between a low wind stress ($U_* = 2 \times 10^{-3} \text{ ms}^{-1}$), a moderate wind stress ($U_* = 3.5 \times 10^{-3} \text{ ms}^{-1}$) and a high wind stress ($U_* = 5 \times 10^{-3} \text{ ms}^{-1}$).

Chapter 5

Aggregation Intensity Analysis

5.1 Plankton Aggregation Definitions

Plankton blooms are common place in the ocean (Pinckney et al., 1998). However, the spatial distribution of a bloom is irregular and does not take a specific form. Quantifying such patterns is therefore not such a simple task, so we will explore possible measures quantifying aggregations currently in the literature and make a choice as to which method may be most effective for this work. This chapter will contain the bulk of the novel techniques and new results in this thesis.

5.1.1 Aggregation Measures

The type of boundary layer modelled in this work is driven by shear and so it is likely that the type of aggregation that will be observed will be thin layer planktonic aggregations (via straining). Thin layers usually have thickness of between a few centimetres and a few metres. Certain criteria need to be met before a aggregation can be classed as a thin layer (Durham and Stocker, 2012), these include;

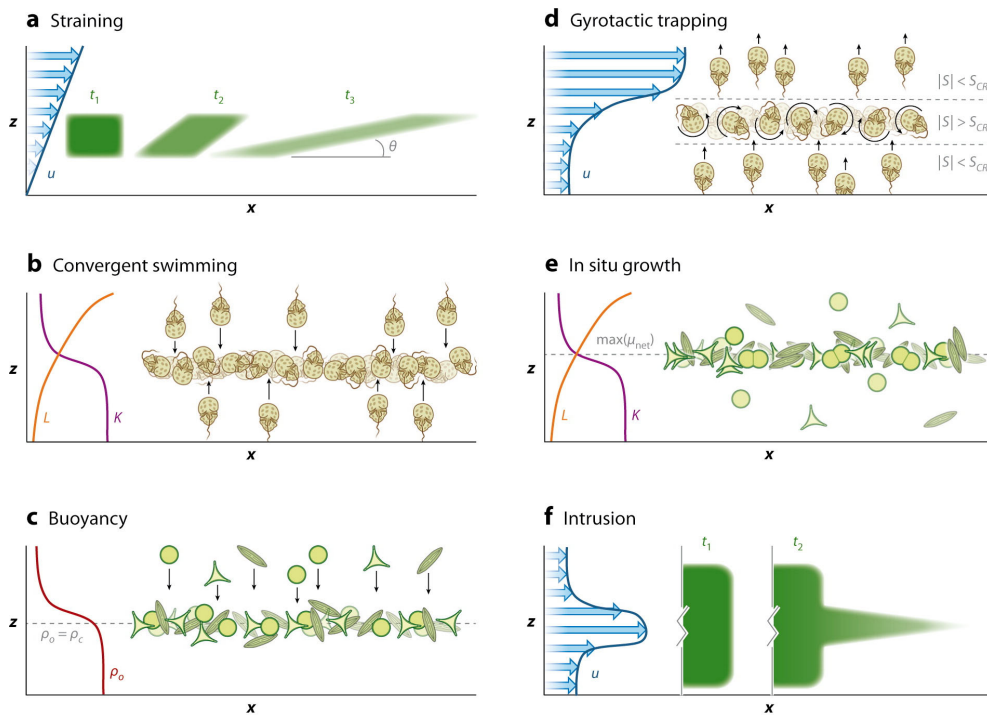
1. The aggregation must be spatially and temporally persistent.
2. For a ‘thin’ layer, the vertical extent must not exceed a certain value.
3. The maximum concentration must exceed a threshold.

This raises the question as to what constitutes a concentration threshold? There is no consistent definition in the literature and so a plankton aggregation may be present according to one author and not the other, therefore an alternative approach will be sought.

In the field, thin layers have been found with ratios of maximum concentration to background concentration much higher than 1 order of magnitude with one study finding this ratio to be a maximum of 55 (Ryan et al., 2008). Maximum concentrations, as a statistic however, are not very reliable and may be misleading. Results like this are rare, but it's an indicator that there are likely to be many other physical and biological effects which can enhance aggregations over and beyond the effects of shear (which is illustrated in figure 5.1(a)).

Figure 5.1 illustrates some other mechanisms that can lead to aggregations in thin layers. Sensing and signalling capable organisms can swim towards high nutrient concentrations or light levels 5.1(b). The most observed case is that of diel vertical migration (DVM) in which zooplankton swim towards the surface of a night and deeper during the day to avoid predation themselves (McManus et al., 2005; Sullivan et al., 2010a). Cells can form at pycnoclines, where there is a sharp change in water density (and usually temperature), known as density stratification (see figure 5.1(c) (Alldredge et al., 2002; McManus et al., 2008). This happens because at the pycnocline, there is a small depth interval with a huge range of water densities, which makes it more likely that phytoplankton will be neutrally buoyant in this interval, if they are neutrally buoyant at this region then they will naturally be pulled towards the pycnocline. Gyrotactic trapping, in which motile, bottom heavy cells enter a region of high shear. This level of shear is enough to rotate the cells enough that they start tumbling in the (small) region of high shear (Figure 5.1(d)) (Pedley and Kessler, 1990). Enhanced growth rates at mid-depth levels, where the nutrient stimulus from the base of the mixed layer, coincides with adequate light levels giving a comfortable depth at which

to feed and reproduce. Alternatively, this can happen when there is a locally high concentration of nutrients, see figure 5.1(e) (Cullen and Eppley, 1981; Ryan et al., 2008). Finally, intrusion, where phytoplankton are spread out at peaks in horizontal velocity (occurring at small depth intervals) 5.1(f) (Ryan et al., 2010). All these mechanisms have the potential to generate phytoplankton aggregations and high correlations have been made to thin layers and each of these mechanisms in the literature.




 Durham WM, Stocker R. 2012.
Annu. Rev. Mar. Sci. 4:177–207

Figure 5.1: Different mechanisms behind planktonic thin layers. Used with permission from Durham and Stocker (2012).

The current work in the literature involving generation of thin layers via shear have been previously done in 2D simulations e.g. Birch et al. (2008), which have demonstrated very successfully that shearing promotes thin dense layers of passive tracers. However, this is just the first part in studying this phenomenon via straining. It is

important, particularly in turbulent flows, to assess the 3-dimensional aspect of this shearing mechanism as turbulence is inherently 3-dimensional. This study will include delving into three dimensions and assessing the role of Langmuir cells in these thin aggregations and how this may enhance thin layer formation. Langmuir cells produce convergent zones in the ocean and the enhancement this could have to phytoplankton aggregations could be a crucial component not yet explored in great detail.

Experimental work using fluorescent imaging has advanced rapidly in the last couple of decades and detailed maps of phytoplankton aggregations can be extracted from the ocean giving a very precise picture of thin layers (Cowles and Desiderio, 1993; Benoit-Bird et al., 2010; Moline et al., 2010). These experiments include locating high density chlorophyll concentrations and then analysing the aggregation formation. However, as this work is a mathematical study, certain constraints naturally form part of the model. One large constraint is the horizontal span of the domain. If, for instance, a thin patch occurs in the model, greater than 3 times the background concentration, but spans a fraction of the horizontal domain, locating that patch via average data will not prove effective, as the signal will be averaged out by the relatively large domain size. In other words, the luxury of locating the aggregation first and then analysing the horizontal span that it occurs in, is not at our disposal. This motivates the idea that, what is needed is a quantitative measure of the horizontal heterogeneity.

As discussed in chapter 4, average phytoplankton dynamics only have high concentration differentials with depth when they become completely out of phase (due to varying growth rates with depth). These large differentials are short lived and usually only occur on the way to a near extinction event or a rapid growth event (typically from near extinction). If it was assumed that P did not vary with depth, then the level of horizontal heterogeneity would be the indicator of where the aggregation was occurring and how thick the layer was. For example, if the average concentration of phytoplankton had a value of 1 at all depths, then the depths at which the phytoplank-

ton were well mixed and homogeneous, would be 1 at all $x - y$ points at those depths. Now consider a small depth interval, where concentrations were not well mixed and phytoplankton were aggregating in one third of the horizontal domain and nowhere else, so that the concentration has a value of 3 in one third of that domain and 0 elsewhere. This would still give an average value of 1 at that depth, but would be considered to be a thin layer only if those $x - y$ points where concentrations are at $P = 3$ were analysed in isolation. This is an illustration that average phytoplankton concentration with depth should not be used to determine if there is a thin layer present.

Reigada et al. (2003) suggested that horizontal heterogeneity can be quantified by the following statistic,

$$\Pi_P = \frac{\langle P \rangle^2}{\langle P^2 \rangle}. \quad (5.1)$$

This gives a value of $\Pi_P = 1$ when the horizontal field is perfectly homogeneous and $\Pi_P = \frac{1}{N^2}$ when all concentrations are in one node on the grid (N represents the total amount of lateral grid points). This attempts to encapsulate heterogeneity by the lower the number is, the more heterogeneous the distribution is.

A novel solution to this problem, proposed by Fessler et al. (1994) and used in Durham et al. (2011c), is to split the lateral domain up into boxes of a prescribed size and compute the capacity of each box, relative to the capacity expected if the concentrations are distributed randomly. Essentially this measure is a ratio between standard deviation and mean concentration. This method has an extra complication of choosing a particular box size and so prior knowledge of the size of the aggregation expected must be estimated. This is an ideal solution for measuring micro-scale type aggregations. This method is also geared towards discrete data which does not apply for results derived from the LES-NPZ model.

An alternative measure of quantitative heterogeneity was suggested by Lewis (2005),

given by

$$I = \frac{\langle (P - \langle P \rangle)^2 \rangle}{\langle P \rangle^2}, \quad (5.2)$$

where I is the aggregation intensity. This is very similar to that of Reigada et al. (2003) (in fact $I = \frac{1}{\Pi_P} - 1$), and an analogous continuum form of the measure suggested by Fessler et al. (1994). If the concentration is homogeneous, $I = 0$ and the more heterogeneous the field is, the higher the value. To put some common perspective to this statistic, if half of the concentration field was 3 times that of the other half of the concentration field, then this statistic would give a value of $\frac{1}{4}$. Although there is no discernible difference between I and Π_P , I increases with levels of heterogeneity and perhaps gives a more intuitive meaning with regards to this study and so will be utilised for the rest of this work.

It is important to understand that high levels of heterogeneity may not imply that there is a phytoplankton bloom (e.g. where there is high heterogeneity but low concentration relative to the rest of the biological field), instead it will indicate places where the biology is able to overcome the turbulent mixing. Therefore the reader should note the distinction between planktonic aggregations and planktonic blooms, with emphasis on the former in this work.

5.2 Aggregation Intensity Dynamics

The aggregation intensity measure, I , is a robust measure of the heterogeneity of a concentration field as the statistic is low order and hence will not be subjected to sharp fluctuation. The next step is to analyse the evolution of I as the phytoplankton population passes through a typical cycle of growth and decay. Figure 5.2 shows a typical biology mean concentration evolving in time with its corresponding aggregation intensity. During this phytoplankton cycle, we see a surge in aggregation intensity at the very beginning of the cycle, followed by a slow decline to homogeneity, corresponding approximately to the maximum of $\langle P \rangle$. As $\langle P \rangle$ declines, there is a secondary

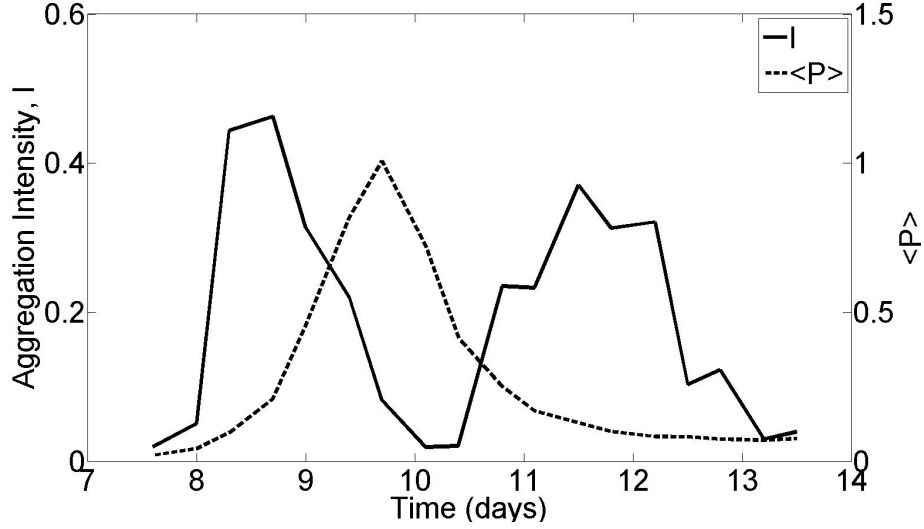


Figure 5.2: Typical aggregation intensity dynamics during a phytoplankton life cycle for $\mu_P^{max} = 8.64 \text{ days}^{-1}$. The dashed line shows the evolution of the mean phytoplankton concentration (RHS scale) and the solid line shows the evolution of the aggregation intensity, I (LHS scale). This was taken at $z = 25.6\text{m}$ which was the optimum aggregation depth for this simulation (see later for definition of optimum aggregation depth).

surge in aggregation intensity. This behaviour is typical of the model at those boundary layer depths at which I is appreciable. In order to shed light on this phenomenon, one needs to examine the mathematical equations governing the evolution of I .

5.2.1 Aggregation Intensity Dynamical Decomposition

Firstly, to do any analysis on this heterogeneity measure, one must first simplify the LES-NPZ model equations following similar procedures used for the stability analysis of chapter 4 (we can take away depth dependence in the biological parameters as I is depth independent). This gives one the following equation for P (note we are only interested in the dynamics of the phytoplankton field and so analysis will only be on the equation for the dynamics on P),

$$\frac{\partial P}{\partial t} + \mathbf{u} \cdot \nabla P = D_P \nabla^2 P + aPN - bPZ \quad (5.3)$$

where again, a and b are growth and predation rates respectively. Following an analogous method to deriving the equation for the energy dissipation rate, we split all the variables into their mean and fluctuating parts, i.e.

$$\begin{aligned}\mathbf{u} &= \langle \mathbf{u} \rangle + \mathbf{u}' \\ P &= \langle P \rangle + P' \\ Z &= \langle Z \rangle + Z' \\ N &= \langle N \rangle + N'\end{aligned}$$

where $\langle \cdot \rangle$ denotes horizontal averaging and $(\cdot)'$ denotes a fluctuation term around the mean (at a particular depth). Substituting these terms into equation 5.3, multiplying through by $2(\langle P \rangle + P')$, averaging horizontally and throwing away small horizontal gradients, we arrive at the equation

$$\begin{aligned}& \frac{\partial \langle P'^2 \rangle}{\partial t} + \frac{\partial \langle P \rangle^2}{\partial t} + \frac{\partial \langle w \rangle \langle P \rangle^2}{\partial z} + 2 \langle P \rangle \frac{\partial \langle P' w' \rangle}{\partial z} \\ & + \frac{\partial \langle w \rangle \langle P'^2 \rangle}{\partial z} + 2 \langle P' w' \rangle \frac{\partial \langle P \rangle}{\partial z} + \frac{\partial \langle P'^2 w' \rangle}{\partial z} \\ & = D_P \left(\frac{\partial^2 \langle P \rangle^2}{\partial z^2} + \frac{\partial^2 \langle P'^2 \rangle}{\partial z^2} - 2 \left(\frac{\partial \langle P \rangle}{\partial z} \right)^2 - 2 \left\langle \left(\frac{\partial P'}{\partial z} \right)^2 \right\rangle \right) \quad (5.4) \\ & + 2a (\langle P \rangle^2 \langle N \rangle + 2 \langle P \rangle \langle P' N' \rangle + \langle P'^2 \rangle \langle N \rangle + \langle P'^2 N' \rangle) \\ & - 2b (\langle P \rangle^2 \langle Z \rangle + 2 \langle P \rangle \langle P' Z' \rangle + \langle P'^2 \rangle \langle Z \rangle + \langle P'^2 Z' \rangle).\end{aligned}$$

We also need to find the term $\frac{\partial \langle P \rangle^2}{\partial t}$, which can be found more simply by averaging equation 5.3 and multiplying by $2 \langle P \rangle$ i.e.,

$$\begin{aligned}
& \frac{\partial \langle P \rangle^2}{\partial t} + \frac{\langle P \rangle^2 \langle w \rangle}{\partial z} + 2 \langle P \rangle \frac{\partial \langle w' P' \rangle}{\partial z} \\
&= D_P \left(\frac{\partial^2 \langle P \rangle^2}{\partial z^2} - 2 \left(\frac{\partial \langle P \rangle}{\partial z} \right)^2 \right) \\
&+ 2a (\langle P \rangle^2 \langle N \rangle + \langle P \rangle \langle P' N' \rangle) \\
&- 2b (\langle P \rangle^2 \langle Z \rangle + \langle P \rangle \langle P' Z' \rangle).
\end{aligned} \tag{5.5}$$

These two equations essentially govern the evolution of the aggregation intensity, since

$$\frac{\partial I}{\partial t} = \frac{\partial}{\partial t} \left(\frac{\langle P'^2 \rangle}{\langle P \rangle^2} \right) = \frac{1}{\langle P \rangle^2} \left(\frac{\partial \langle P'^2 \rangle}{\partial t} - I \frac{\partial \langle P \rangle^2}{\partial t} \right). \tag{5.6}$$

It is then a simple matter of taking a combination of equations 5.4 and 5.5 to arrive at the final equation for the aggregation intensity dynamics,

$$\begin{aligned}
& \frac{\partial I}{\partial t} + \frac{1}{\langle P \rangle^2} \frac{\partial \langle w' P'^2 \rangle}{\partial z} + 2 \frac{\langle w' P' \rangle}{\langle P \rangle^2} \frac{\partial \langle P \rangle}{\partial z} - \frac{2I}{\langle P \rangle} \frac{\partial \langle w' P' \rangle}{\partial z} \\
&= \frac{D_P}{\langle P \rangle^2} \left(\frac{\partial^2 \langle P'^2 \rangle}{\partial z^2} - 2 \left\langle \left(\frac{\partial P'}{\partial z} \right)^2 \right\rangle + I \left(2 \left(\frac{\partial \langle P \rangle}{\partial z} \right)^2 - \frac{\partial^2 \langle P \rangle^2}{\partial z^2} \right) \right) \\
&+ \frac{2(1-I)}{\langle P \rangle} (a \langle P' N' \rangle - b \langle P' Z' \rangle) \\
&+ \frac{2}{\langle P \rangle^2} (a \langle P'^2 N' \rangle - b \langle P'^2 Z' \rangle).
\end{aligned} \tag{5.7}$$

The first line in equation 5.7 (not including $\frac{\partial I}{\partial t}$) are the mixing and transport terms, which will be referred to as the “flow terms”. The second line comprises the diffusion terms. The third line is made up of biological covariances, which will be referred to

as “biological doubles” and the fourth line will be referred to as the “biological triples”.

The equation derived for the aggregation intensity dynamics is very complex and needs careful analysis as to the key features which stimulate heterogeneity in the concentration field. First of all, there is the interplay between the biological terms and the flow terms. If the flow terms are larger than the biological terms, then any potential aggregations stimulated by the biological growth, will be dissipated by the fluid dynamics before their existence can manifest itself by a spike in the level of I . The intricate interplay between these processes will be investigated in this section.

5.2.2 Biology vs. Flow

One of the problems associated with simplifying the model is that some important complexity has been taken away. One of the main concerns is that the nutrient satiation effect on P has been removed. The parameters used in the LES-NPZ model suggest that a phytoplankton cell reaches a satiated state if it resides in a nitrate concentration of $N \approx 3$. In such a concentration, growth will reach its maximum efficiency. With the nitrate flux condition set to $Q = 130$, the ambient nutrient concentration hits this concentration after 6-7 days. This means that any comparisons between the correlations must be made in the first week of simulation time if one wants to use the aggregation dynamic equation. When the $\langle P \rangle$ field is completely satiated with nutrients, the phytoplankton will essentially see the entire nutrient field as homogeneous. However, this does not mean that the correlations will be useless at these times. As the correlations have the same period as the population cycles themselves, it will give historical information about which quantities are stimulated by the aggregations, and so can be used as a guide for what the mechanisms are behind the said aggregations.

The analysis of these correlation terms must be treated with a certain degree of caution as data is only recorded at certain specific sampling times. Monitoring these correlations continuously during a simulation would exceed computational storage capacity

limits. The correlation statistics exhibit rapid fluctuations, on time scales much faster than the sampling time. Consequently the sampled data gives a smoother impression of the evolution of the correlation statistics than is actually the case. Therefore, we can apply certain smoothing techniques to the correlation data to get a general view of the dynamics of each term without any great loss of information. This smoothing will be a 5-point moving average of the form,

$$f_i^S = \frac{1}{5} \sum_{j=i-2}^{i+2} f_j$$

where f_j is the data and f_i^S is the smoothed data, around $t = t_i$.

When the mean phytoplankton concentration falls to a very low level i.e. $\langle P \rangle \approx 0$, the aggregation intensity measure behaves erratically. We are not interested in population fluctuations about a very low background level, rather we are looking for evidence of concentration aggregations against a backdrop of medium to high $\langle P \rangle$ levels. Hence in this investigation we will focus on behaviour when $\langle P \rangle \gg 0$. We can apply a simple filter, which effectively disregards all the terms in equations (5.4 - 5.7) at times when $\langle P \rangle \approx 0$. For example, take the aggregation intensity, I , we can apply the following

$$I = I \times \min \left(1, \left(\frac{\langle P \rangle}{0.1} \right)^2 \right), \quad (5.8)$$

which means that if $\langle P \rangle$ goes below a value of 0.1, then the aggregation intensity will be penalised. The same process will be applied to the biological doubles and triples, as well as the flow terms.

Figure 5.3 shows the evolution of the aggregation intensity taken from three different simulations associated with $\mu_P^{\max} = (4.32, 8.64, 17.28) \text{ days}^{-1}$. Each simulation was driven by the same wind stress value, $U_* = 3.5 \times 10^{-3} \text{ ms}^{-1}$. One can see in figure 5.3 the same characteristic bimodal structure (for each period) to the aggregation

intensity evolution, as highlighted in figure 5.2. The key question is, what is driving these sudden surges in aggregation intensity during the growth and decay phases of the mean concentration field $\langle P \rangle$? From the analysis of equation 5.7, one would expect aggregation intensity growth to be promoted when the biological doubles and triples are large compared with the flow terms. This ratio between the biological terms and the physical terms can be expressed by

$$\frac{\text{Biology}}{\text{Flow}} = \left| \frac{\frac{2(1-I)}{\langle P \rangle} (a \langle P'N' \rangle - b \langle P'Z' \rangle) + \frac{2}{\langle P \rangle^2} (a \langle P'^2N' \rangle - b \langle P'^2Z' \rangle)}{\frac{1}{\langle P \rangle^2} \frac{\partial \langle w'P'^2 \rangle}{\partial z} + 2 \frac{\langle w'P' \rangle}{\langle P \rangle^2} \frac{\partial \langle P \rangle}{\partial z} - \frac{2I}{\langle P \rangle} \frac{\partial \langle w'P' \rangle}{\partial z}} \right|. \quad (5.9)$$

Figure 5.4 shows a plot of the evolution of the ratio of biological double and triple terms to the flow terms (equation 5.9), taken at the initial few days of the simulation to avoid analysing satiated $\langle P \rangle$ fields. This equation assumes there is no significant contribution from biological diffusion, this is fair as diffusion is a very weak process relatively and particularly within the time frame of the biological population cycles (\approx a couple of days), will most likely yield negligible contribution towards spatial formation. The filtering mechanism was also in operation so the P concentration was also taken when $\langle P \rangle \gg 0.1$. There is a distinct increase in the scale of ratio 5.9 with increasing μ_P^{\max} , with the highest value of μ_P^{\max} giving a ratio an order of magnitude larger at some times in figure 5.4(a) compared to figure 5.4(c). This suggests that with increasing μ_P^{\max} , biological processes become more dominant, which is what might be expected.

The lower growth rate case (figure 5.4(a)), corresponds to a regime in which the biological correlations are comparable in magnitude to the mixing terms associated with the flow. So for growth rates at or above $\mu_P^{\max} \geq 4.32 \text{ days}^{-1}$, one would expect significant fluctuations in the P field to become apparent. This is a very important aspect in aggregation formation as it is quite obvious that once the physical mixing dominates, the chance of a strong heterogeneous large scale patch being formed are small. It is therefore an assertion that any maximum growth rates larger than $\mu_P^{\max} = 4.32 \text{ days}^{-1}$

are very likely to induce aggregations and anything below will not be strong enough for aggregations to manifest themselves.

The ratios in this section are based on one particular wind stress value of $3.5 \times 10^{-3} \text{ ms}^{-1}$, and the depth from which the statistics in figure 5.4 were derived is below the penetration depth calculated in chapter 4. This was calculated from

$$\int_{\hat{z}}^0 \langle w^2 \rangle dz = \int_{z_{\text{ML}}}^{\hat{z}} \langle w^2 \rangle dz, \quad (5.10)$$

where the penetration depth z_{pen} was defined to be twice the mid-energy depth \hat{z} , i.e. $z_{\text{pen}} = 2\hat{z}$ (z_{ML} is the mixed layer depth). It seems highly likely that biological aggregations will start to manifest themselves below the penetration depth provided $\mu_P^{\text{max}} > 4 \text{ days}^{-1}$ and the mixed layer is not fully penetrated, which was the reason for the choice of wind stress used in this section. The correlations between z_{pen} and optimum aggregation depth will be examined later in the chapter.

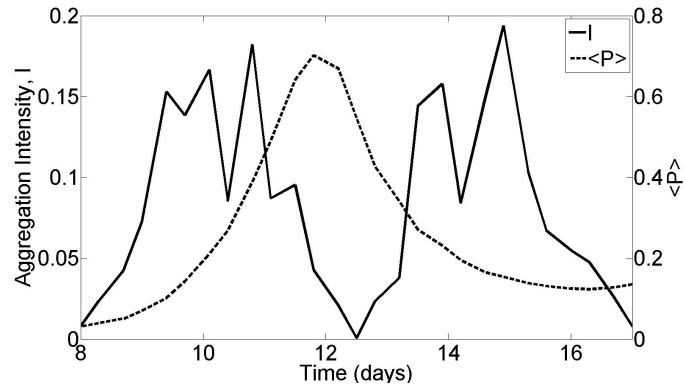
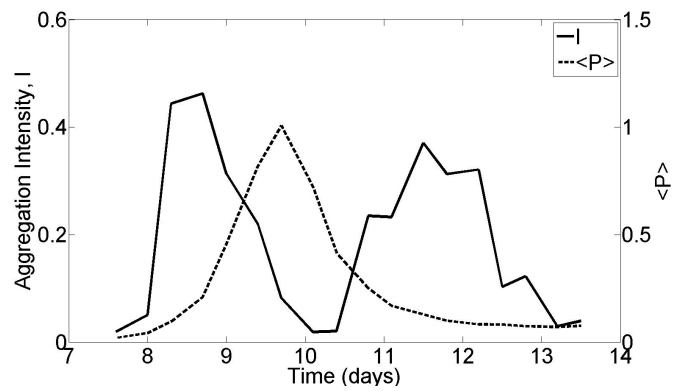
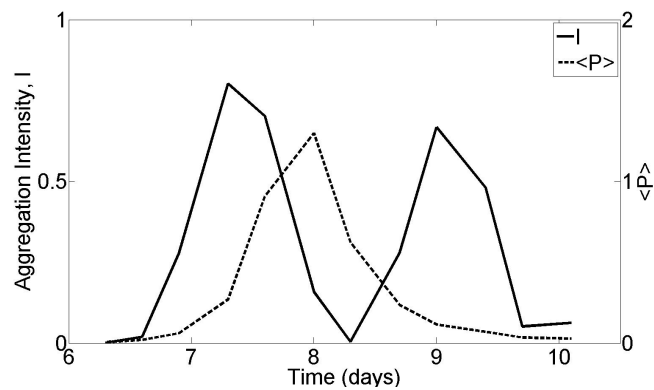
(a) $\mu_P^{\max} = 4.32 \text{ days}^{-1}$ (b) $\mu_P^{\max} = 8.64 \text{ days}^{-1}$ (c) $\mu_P^{\max} = 17.28 \text{ days}^{-1}$

Figure 5.3: Aggregation intensity vs. mean phytoplankton concentration for varying μ_P^{\max} . The dashed line shows the evolution of the mean phytoplankton concentration (RHS scale) and the solid line shows the evolution of the aggregation intensity, I (LHS scale). This was taken at $z \approx 26\text{m}$ which was the optimum aggregation depth for this simulation.

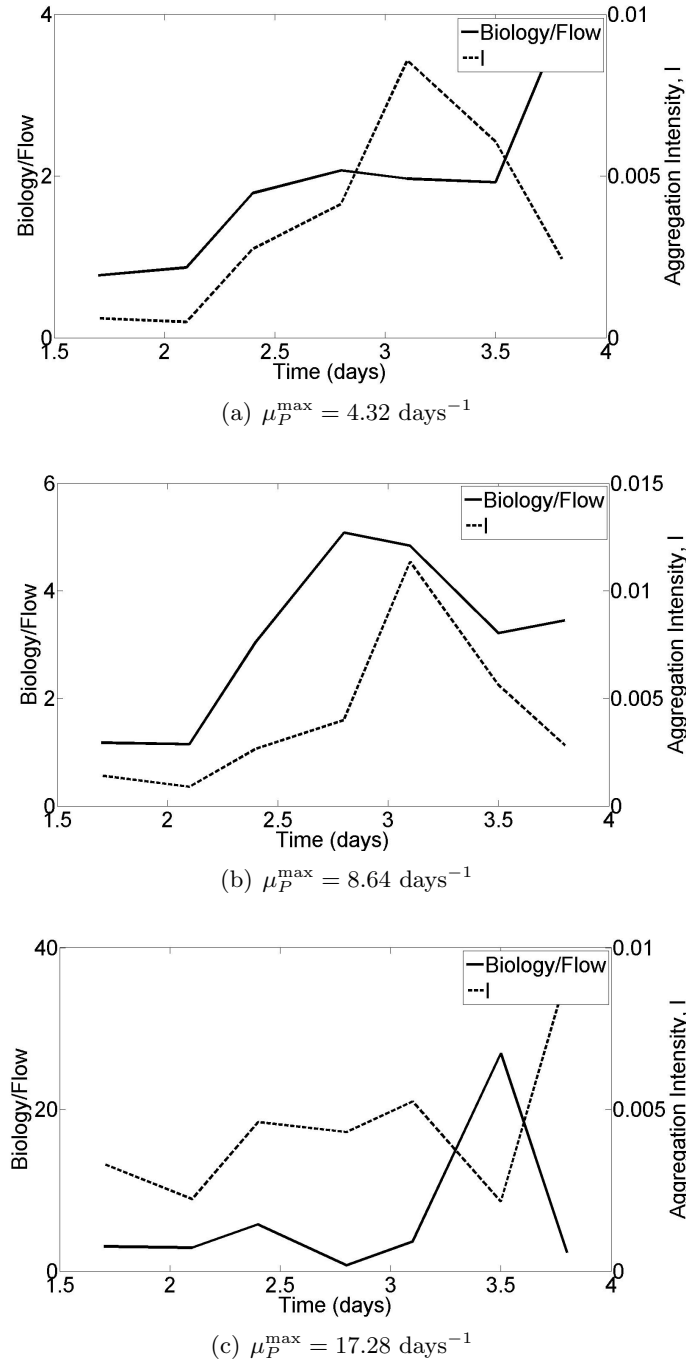


Figure 5.4: Ratio of biological dependant correlations and flow dependant correlations taken at a the first week in simulation time (before phytoplankton are satiated with nutrient) with varying μ_P^{\max} . The dashed line shows the evolution of the mean phytoplankton concentration (RHS scale) and the solid line shows the evolution of the aggregation intensity, I (LHS scale). This was taken at $z \approx 26\text{m}$ which was the optimum aggregation depth for this simulation.

5.2.3 Biological Correlations

Now that it has been established that physical mixing plays only a relatively small role in comparison with the biological processes (at certain depths and wind stress values), above a certain threshold of phytoplankton growth rate, analysis of the aggregation intensity dynamics can be directed toward the biological terms alone. Each of the biological correlations in equation 5.7 influences the dynamics of the aggregation intensity. To understand this, consider the following thought experiment. Suppose we have two regions (in the $x - y$ domain at a given depth), region I, containing a small but significant concentration of P , and region II, almost devoid of P . Now a growth surge in the aggregation intensity will occur when the P concentration rises in region I, but remains relatively small in region II. This would manifest itself as an increase in magnitude (negative or positive) in the ‘doubles’ correlation terms. This is because if there is already a small correlation (negative or positive), then as the concentration of P in region I grows rapidly, the small correlation will become exaggerated. Therefore, one could expect to see significant aggregation intensity value when the absolute value of the combined biological doubles reaches a local maximum.

The biological triples play a different role. Consider the case when the $\langle P \rangle$ concentration is ‘skewed’. A concentration field will be said to be ‘skewed’ if,

- (a) the frequency of low concentration values (below the mean) significantly exceeds the frequency of high concentrations (above the mean) (positive skewness),
- (b) the frequency of high concentration values (above the mean) significantly exceeds the frequency of low concentrations (below the mean) (negative skewness).

This skewness will manifest itself in the biological triples. The more skewed (negative or positive) the phytoplankton concentration field is, the higher the aggregation intensity will become. Therefore, the higher the absolute value of the combined biological triples, the higher the aggregation intensity will be.

It is observed in figure 5.5 that during the $\langle P \rangle$ population cycle, local peaks (and troughs) in the biological triples occur at the same times as peaks in aggregation intensity (see also figure 5.3(b)). This reinforces the point made earlier that when activity in the biological correlations is at a local maximum, so is the intensity of aggregations. It is important to note that there is no horizontally spatial dynamics in the biology (our plankton fields cannot swim for instance) and so only the flow can instigate this heterogeneity initially (regions in the $x - y$ plane having the characteristics of regions I and II), before the biological dynamics promotes further aggregations. This means the flow is actually vital in instigating aggregations, even if their subsequent evolution is driven by the biological dynamics. This is intuitively the case as, not only does the flow bring up nutrients from the base of the boundary layer, but it does so in select regions, as the lateral domain is split up into equal amount of downwelling and upwelling, where the latter is nutrient rich in comparison to the former. This will then locally enhance growth P growth rates and hence enhance heterogeneity.

There is a simple way to find which terms are promoting heterogeneity. Firstly, by taking ratios of the two biological doubles to see which dominates and secondly, taking the ratio of the two biological triples (we will only take $\mu_P^{\max} = (4.32, 17.28) \text{ days}^{-1}$ for illustration and again within the first week of simulation time, see figure 5.6). It is clear that there is rather a large difference between the correlations involving N and the correlations involving Z with around 1 order of magnitude difference in favour of the nitrate. This shows that in this system, the heterogeneity is being influenced mainly by the nitrate concentration, which is being driven by the flow. This implies that it is the flow which is stimulating heterogeneity and it is the biology which enhances it. Although the nitrate will soon become homogeneous from the perspective of the phytoplankton due to satiation, it has brought the lateral biological concentrations out of phase enough so that region I and region II are (dynamically) distinct from one another. This means that if an extinction phase was to occur, then region I would grow rapidly in the region of high nitrate concentration (irrespective of satiation due

to periodicity). If the time phase of region I and II was such that $\langle P \rangle$ reaches a high concentration in region I and still ≈ 0 in region II, then the concentration will appear to be very aggregated in region I.

Now that we have established what biological processes are driving the biological heterogeneity (when physical conditions are right), attention must now turn to the effect physical conditions have on phytoplankton aggregation and what is the 'ideal' level of wind forcing for such aggregation to form?

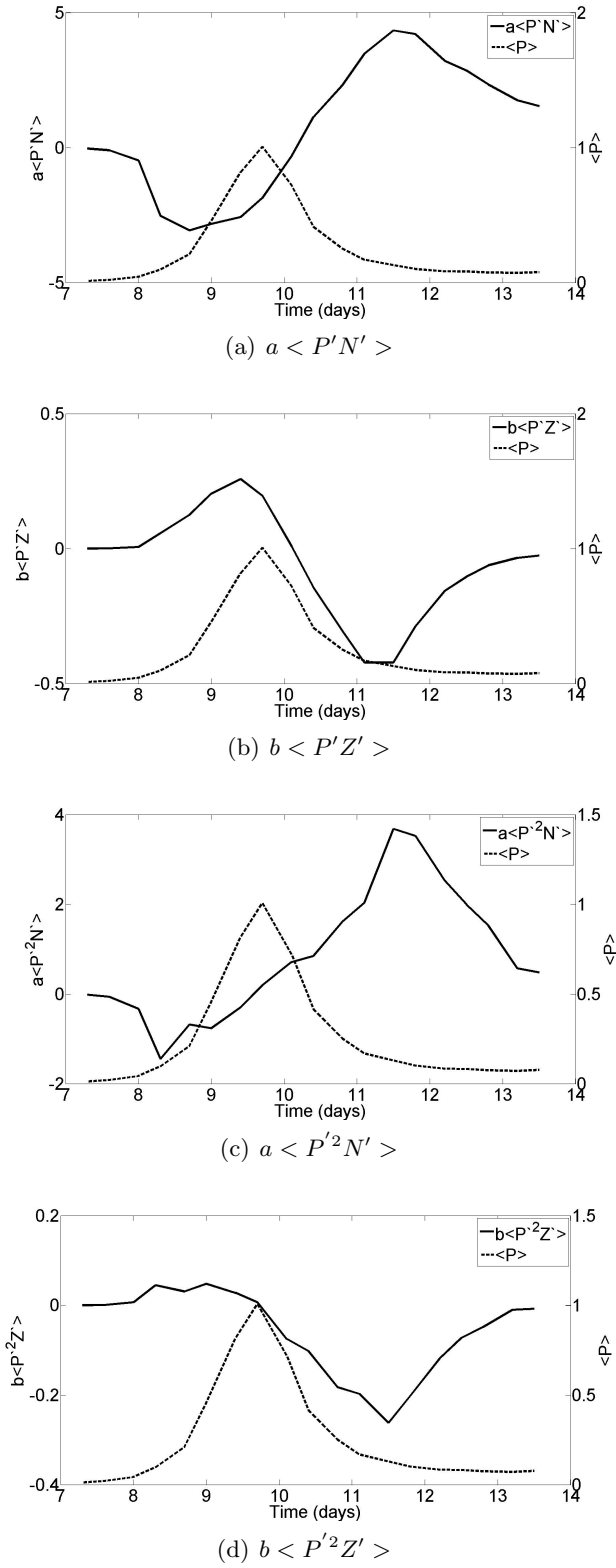
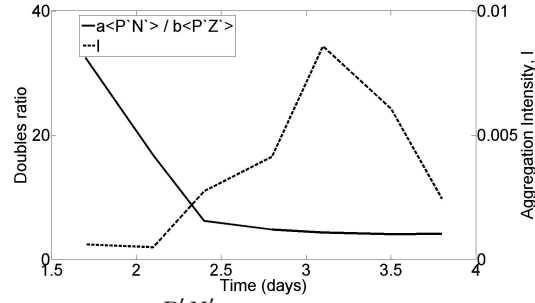
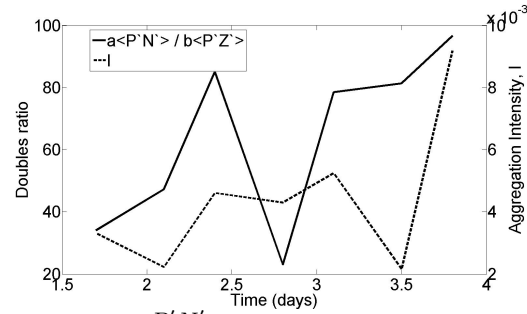


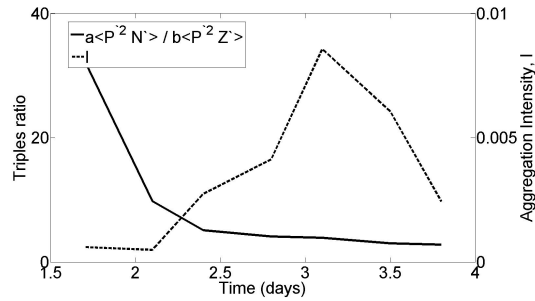
Figure 5.5: Biological doubles and triples for $\mu_P^{\max} = 8.64 \text{ days}^{-1}$. The dashed line shows the evolution of the mean phytoplankton concentration (RHS scale) and the solid line shows the evolution of the individual biological doubles and triples (LHS scale). This was taken at $z \approx 26\text{m}$ which was the optimum aggregation depth for this simulation.



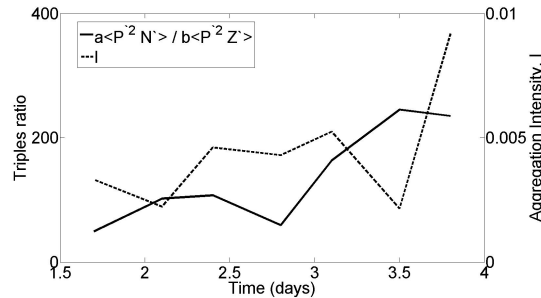
$$(a) \frac{a \langle P' N' \rangle}{b \langle P' Z' \rangle}, \mu_P^{\max} = 4.32 \text{ days}^{-1}$$



$$(b) \frac{a \langle P' N' \rangle}{b \langle P' Z' \rangle}, \mu_P^{\max} = 17.28 \text{ days}^{-1}$$



$$(c) \frac{a \langle P'^2 N' \rangle}{b \langle P'^2 Z' \rangle}, \mu_P^{\max} = 4.32 \text{ days}^{-1}$$



$$(d) \frac{a \langle P'^2 N' \rangle}{b \langle P'^2 Z' \rangle}, \mu_P^{\max} = 17.28 \text{ days}^{-1}$$

Figure 5.6: Biological double ratios and biological triple ratios for different μ_P^{\max} . The dashed line shows the evolution of the mean aggregation intensity (RHS scale) and the solid line shows the evolution of ratios of the various biological doubles and triples (LHS scale). This was taken at $z \approx 26\text{m}$ which was the optimum aggregation depth for this simulation.

5.3 Effect of Friction Velocity, U_*

The rest of this work will use the full LES-NPZ model, without simplifications. It has been shown in chapter 4 that the levels of wind forcing have significant effects on the boundary layer. In particular, at certain wind stresses, the boundary layer becomes fully penetrated and high levels of mixing will be prominent at most depths. However, it is not clear what effect this will have on lateral biological heterogeneity, and so in this section we will explore the dependence of aggregation intensity on wind stress.

5.3.1 Aggregation Depth Dependence

To quantify how strong the level of aggregation is in a simulation, we first need to focus in on the depths at which aggregations are most prominent. Therefore, we need to define a depth for which aggregation is likely to reach its highest level. This will be known as the optimum aggregation, z_{opt} . It is tempting to define z_{opt} as the depth at which I reaches its maximum. However, as discussed previously, maximum intensity is not a robust statistic and any definition of z_{opt} based on such a maximum would exhibit sharp fluctuations. It is much better to define z_{opt} in terms of an averaged aggregation intensity at each depth, as ephemeral aggregations will be smoothed out with this statistic. A (potential) phytoplankton aggregation will then be defined at the depth at which the average aggregation intensity, denoted by $I_{\text{av}}(z)$, reaches its maximum, i.e. at $I_{\text{av}}(z_{\text{opt}})$. This leads to the following mathematical definition for z_{opt} ,

$$\text{Max}_j \left[\frac{\sum_{i=0}^N I(z_j, t_i)}{t_N} \right] = \text{Max}_j [I_{\text{av}}(z_j)] = I_{\text{av}}(z_{\text{opt}}). \quad (5.11)$$

where t_N is the time-scale of the simulation. Graphically, this is shown in figure 5.7.

Figure 5.8 shows profiles of I_{av} of low, medium and high wind stresses, where high wind stress characterises a regime in which the boundary layer is penetrated and low wind stress characterises a regime in which $I_{\text{av}}(z)$ profiles are not unimodal. It is apparent that for low wind stress, profiles of average intensity are bimodal and there is no

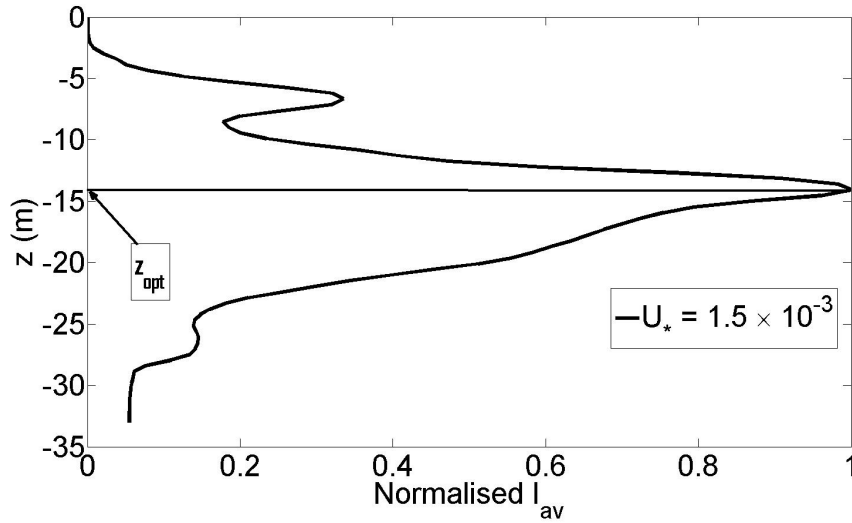
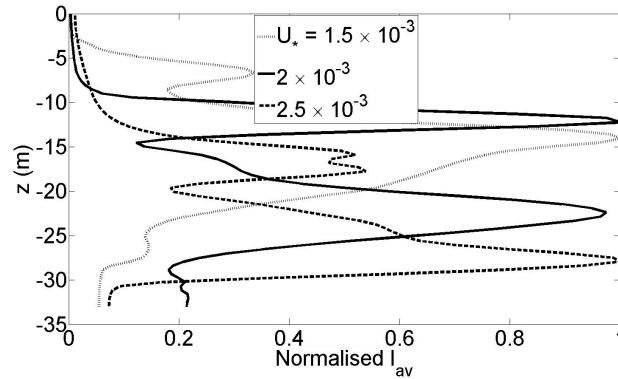


Figure 5.7: Profile of the average aggregation intensity, normalised by its own maximum $\frac{I_{av}(z)}{\max(I_{av}(z))}$. z_{opt} is displayed to show how the optimum aggregation depth is defined graphically. This example was taken for a low wind stress value of $U_* = 1.5 \times 10^{-3} \text{ ms}^{-1}$.

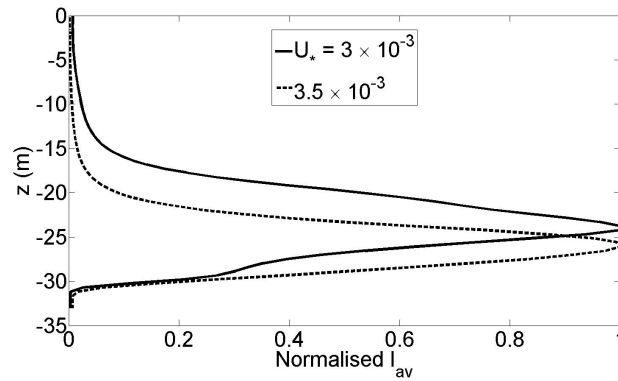
unique depth at which I_{av} reaches a definite maximum (figure 5.11(a)) (Note however, there is no physical reason why the distribution should be bi-modal, in fact the levels of aggregation are very low (although not shown in these graphs) and so any inferences can be disregarded), whereas for medium wind stresses it is evident that the profiles are unimodal and have a distinct optimum aggregation depth (figure 5.11(b)). High wind stresses also have a distinct optimum aggregation depth, however the profile is beginning to show signs of spreading, where the thin peak, observed in the medium wind stress case, is becoming less distinct as U_* increases (figure 5.8(c)). This spreading of average aggregation intensity as U_* increases is indicative that the boundary layer is starting to become extremely well mixed, across the whole of the boundary layer of depth 33 m prescribed here. Further increases in U_* beyond those shown here would see a return to a completely uniformly mixed boundary layer in which no distinct z_{opt} value would be apparent. It can then be inferred that at over intermediate ranges of wind stress, phytoplankton aggregations will tend to thrive close to one distinct depth interval in the boundary layer and more importantly, this depth interval will be

relatively small. That is, one would expect to see aggregations in thin layers, a phenomena observed in many experimental trials (McManus et al., 2003; Menden-Deuer and Grünbaum, 2006; Widder et al., 1999). This depth interval (or layer thickness) will be analysed later in this chapter.

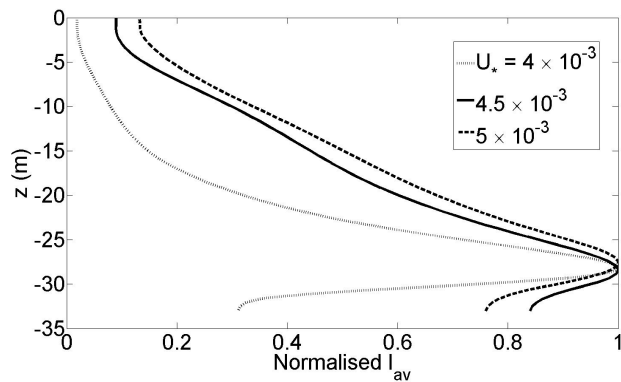
Analysing the behaviour of optimum aggregation depth, z_{opt} , with increasing wind stress, two things are apparent. Firstly, and most obviously, z_{opt} deepens as the wind stress increases. Secondly, for large wind stress, z_{opt} stops deepening and remains constant. This behaviour is almost identical to the penetration depth behaviour, as can be seen in figure 5.9. One can see that the optimum aggregation depth is consistently beneath the penetration depth, z_{pen} . As U_* increases, the transitional band of low Re number, quasi-laminar flow, between the penetration depth and the mixed layer base, becomes thinner, note that this laminar band is artificial, because it is established by the prescribed mixed layer base. The laminar band is artificial in the sense that the mixed layer depth is fixed in this model, with a no-slip boundary condition attached. If the mixed layer depth was doubled, the higher levels of turbulent mixing would likely stay at the same range of depths (down to 10-15m), but the band of laminar flow would increase dramatically. This means that an appropriate choice of mixed layer depth must be chosen and the pycnocline is an apt reference for this choice. The laminar layer thinning promotes a smaller interval of depths at which the phytoplankton are likely to flourish and hence form thin layers. This region of the boundary layer will be termed laminar stratified. As was remarked on in section 4.3.2, at a particular wind stress, the flow becomes more or less fully developed (i.e. active at all depths). This is clear from the levels of heterogeneity in figure 4.11, when the mixing levels increase to a level where phytoplankton concentrations are homogenised over the entire depth of the boundary layer. Now since the amount of wind stress needed to fully penetrate the boundary layer is reached at around $U_* = 4 \times 10^{-3}$, adding more wind stress to the surface would not significantly increase the penetration depth as penetration has already been achieved (note, the penetration depth will never reach the bottom of



(a) low wind stress



(b) medium wind stress



(c) high wind stress

Figure 5.8: Average aggregation intensity profiles, $I_{av}(z)$, normalised by their own maximum, $\max [I_{av}(z)]$ ranging from low to high wind stress regimes.

the boundary layer as this would imply a balance of $\langle w^2 \rangle$ between the top half of the boundary layer and the bottom half, a phenomenon which cannot happen due to friction and energy dissipation). Hence, the start of a plateau in penetration depth happens when U_* hits a critical value (in this case $U_* = 4 \times 10^{-3}$), when the boundary layer is fully penetrated.

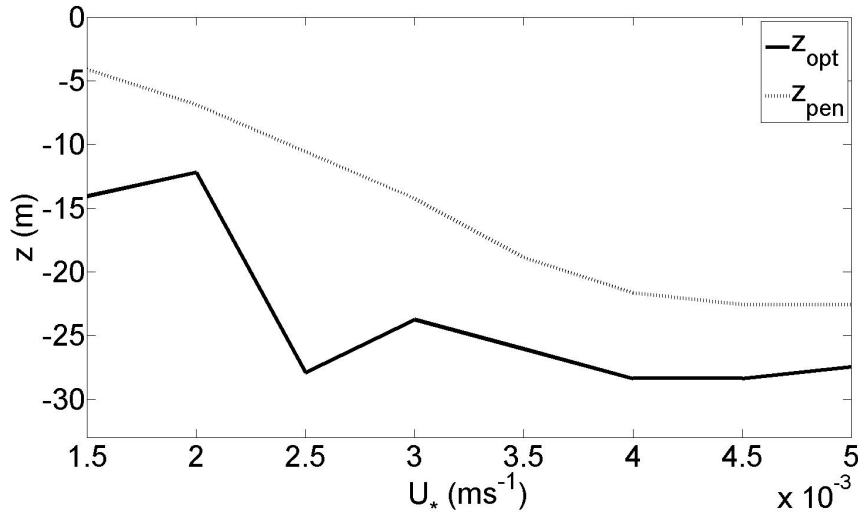


Figure 5.9: Variation of optimum aggregation depth, z_{opt} , a measure of the depth at which lateral biological concentrations are most heterogeneous, with wind stress. The variation of the penetration depth z_{pen} is also shown.

The region of laminar stratification represents a transitional flow between laminar flow and turbulent flow, where vertical currents are still prominent but lateral turbulent mixing is not. If the penetration depth could be thought of as a pseudo mixed layer depth, then planktonic aggregations brought on by means of laminar stratification, would appear in a similar region to that of the pycnocline (i.e. below the mixed layer). In this way, the stratified laminar layer has similar properties to that of the pycnocline, in that turbulent mixing is not present, but vertical currents are (Fernando, 1991). As the physics prescribing density variation is not present, only analogies to the pycnocline can be made. In fact if there was a pycnocline present in the model, it would be likely

that the thin layer aggregation would be enhanced due to the flow being even more quiescent in the laminar layer than what is observed in this model setup.

5.3.2 Aggregation Intensity Magnitude

Now that z_{opt} has been defined, we can explore the intensity of the aggregations for each simulation. Figure 5.10 shows how the optimum aggregation intensity, $I_{\text{av}}(z_{\text{opt}})$, varies with wind stress. It is clear from figure 5.10, that there is an optimum wind stress value, just below the level of wind stress required to fully penetrate the mixed layer (note, the boundary layer was deemed fully penetrated for $U_* = 4.0 \times 10^{-3}$. This is

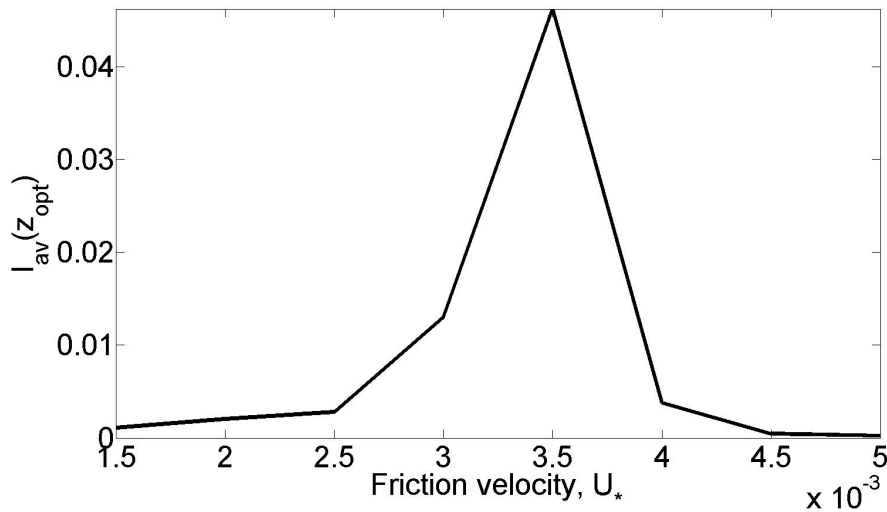


Figure 5.10: Optimum aggregation intensity, $I_{\text{av}}(z_{\text{opt}})$, taken for a range of wind stress values.

an interesting observation as one would have expected aggregations to occur primarily in boundary layers subjected to low wind stress, where there is less turbulent mixing present. An explanation for this non-intuitive phenomenon may lie in the vertical mixing component $\langle w^2 \rangle$. $\langle w^2 \rangle$ governs the vertical mixing strength of the Langmuir cells that are set up in the boundary layer. As discussed in chapter 2, Langmuir cells are sets of vortical tubes that are set up as a result of the Stokes drift associated with the surface waves. These Langmuir cells are observed at each depth in a pattern of

elongated regions of upwellings and downwellings. However, for nutrients to converge in the convergent zones between Langmuir cells (at upwellings), certain requirements must be met. As the nutrient flux boundary condition is applied at the base of the boundary layer, vertical currents (upwellings) must be strong enough to pull nutrients up into convergent zones. Turbulent mixing should not be too prominent, as this increase concentration mixing will act against biological aggregation. In other words, the energy dissipation rate, $\langle \epsilon \rangle$, must be small.

The set of conditions outlined above help to make figure 5.10 more explicable. At low wind stresses, vertical mixing is low near the base of the boundary layer and hence the vertical currents are not strong enough to advect nutrients into the euphotic zone, where biological growth will be most prominent. Hence, rapid biological growth, which is a pre-requisite to the formation of aggregations, is unlikely to occur. At the high wind stress values, the boundary layer is completely penetrated and biological concentrations are mixed (and homogenised) over all depths. But at intermediate wind stress values, $\langle w^2 \rangle$ is sufficiently strong to advect nutrients into the euphotic zone, whilst (near z_{opt}) $\langle \epsilon \rangle$ is insufficient to smooth out the subsequent biological aggregations. Hence, intermediate wind stresses seem to form part of a ‘goldilocks criteria’ necessary for the formation of biological aggregations, at or around z_{opt} in the laminar stratified zone. Although it could be construed that the aggregations are developed by overlapping light and nutrient contribution, stress must lie on the fact that aggregation in the context of this work applies to variation in concentration in the $x - y$ plane. As light does not vary with x and y , the only factor which remains to bring about heterogeneous distribution is the flow field and the nutrient distribution.

5.3.3 Effect of Mixed Layer Depth, z_{ML}

The idea that a fixed boundary layer depth can be used in this model is fair, as the boundary layer splits itself into an oceanic upper mixed layer and a pycnocline (where turbulent mixing is concerned). However, exploring different boundary layer depths for

suitability may enhance modelling this effect. Note that the mixed layer depth is the extent of the numerical domain and not defined by the properties of the flow field.

Taking two different sized boundary layers, $z_{ML} = 20$ m and $z_{ML} = 50$ m, we notice the exact behaviour from before, that is, the optimum aggregation depth, z_{opt} still invariably stays below the penetration depth, z_{pen} (see figure 5.11). However, when

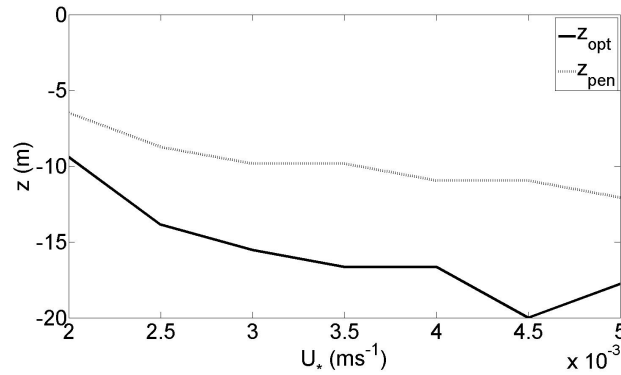
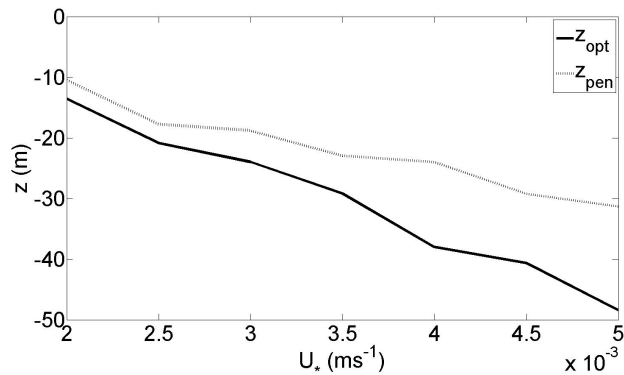
(a) $z_{ML} = 20$ m(b) $z_{ML} = 50$ m

Figure 5.11: Relationship between the optimum aggregation depth, z_{opt} and wind stress, U_* . Also included is the penetration depth, z_{pen} and how that varies with wind stress. This was taken for a shallow boundary layer, $z_{ML} = 20$ m and a deep boundary layer, $z_{ML} = 50$ m.

it comes to the optimum intensity levels for each wind stress value, the behaviour is not quite the same. Figure 5.12(a) shows the same goldilocks zone observed in figure

5.10, for a boundary layer depth of 20 m, however the actual magnitude of optimum intensity is far lower. This is possibly due to turbulent mixing being more prominent

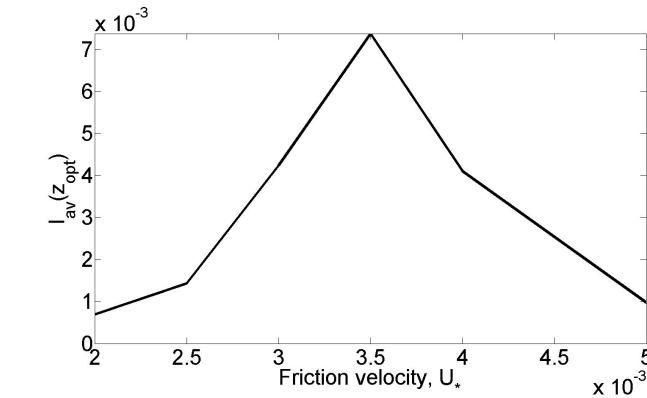
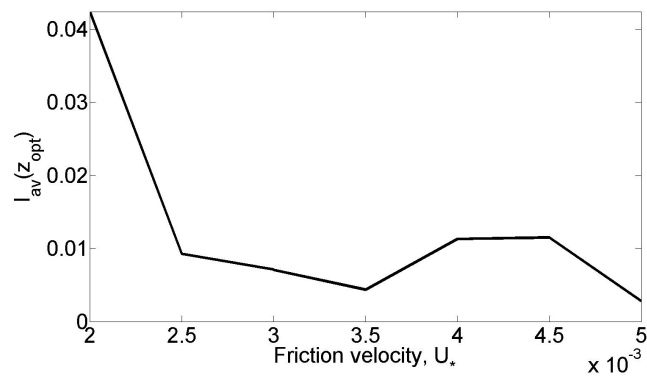
(a) $z_{ML} = 20\text{m}$ (b) $z_{ML} = 50\text{m}$

Figure 5.12: Relationships between optimum aggregation intensity, $I_{av}(z_{opt})$ and the mixed layer depth. Taken for a shallow boundary layer and a deep boundary layer.

over a greater proportion of the boundary layer and so the physical forcing would find it easier to mix the boundary layer. For a larger boundary layer depth of 50 m (figure 5.12(b)) the goldilocks behaviour is not apparent. This is probably due to the vertical mixing struggling to reach the base of the mixed layer to pull nutrients up as wave effects are not strong at these depths.

In shallow waters, high wind stress would try to increase the depth of the entire mixed

layer, so high wind stress regimes may not be realisable in a fixed shallow boundary layer. Similarly, the deeper boundary layer subjected to low wind stress may not be realistic as the depth of the mixed layer would not be sustainable. With these results in mind, it would be a good assumption that a middle ground between the shallow and deep boundary layer depths would be suitable for this analysis and so we will use $z_{\text{ML}} = 33$ m (although this value is arbitrary and is not an ‘optimum’ boundary layer depth).

5.4 Effect of Biology on Aggregation Intensity

There are many biological parameters making up the LES-NPZ model and it is just not possible to investigate the effect of each one on aggregation intensity, due to the large number of simulations that would be necessary. So we need to be somewhat discerning as to which biological parameters are most likely to have a big influence on I_{av} . We have seen that the parameters which promote phytoplankton growth are the nutrient concentration and phytoplankton maximum growth rate, μ_P^{max} . We will use the nitrate pump strength, Q , to parametrise the former (see section 3.3). One other parameter which will also be investigated is the zooplankton predation rate. The decision to choose investigating this over the zooplankton death rate is due to the non-linear nature of the predation rate and the fact that the zooplankton death rate only becomes prominent when the phytoplankton concentration is very low when it simply displays exponential decay. The zooplankton predation rate will be parametrised by the contact radius, R , of the zooplankton, which is the simplest parameter which prescribes zooplankton predation.

5.4.1 Phytoplankton Growth Rate, μ_P^{max}

As discussed in section 4.4.2, μ_P^{max} makes considerable contribution to the growth surge of $\langle P \rangle$. It also exaggerates the length of time $\langle P \rangle$ stays in the near extinction phase. When analysing the level of aggregation intensity, we must take a couple of things into account. First, the aggregation intensity measure will be averaged over

the whole time period, therefore any heterogeneity which occurs during the extinction phases will not be picked up, due to the filter operation imposed on I . Second, the amount of time a single bloom actually lasts for is decreased when μ_P^{max} is increased. Despite these constraints to the aggregation intensity, the phytoplankton concentration reaches a much higher level during a bloom for higher values of μ_P^{max} .

Figure 5.13 shows the average intensity profile with depth for $\mu_P^{max} = (2.16, 4.32, 8.64, 17.28)$. With increasing μ_P^{max} , the magnitude of I_{av} also increases. What is curious is that the

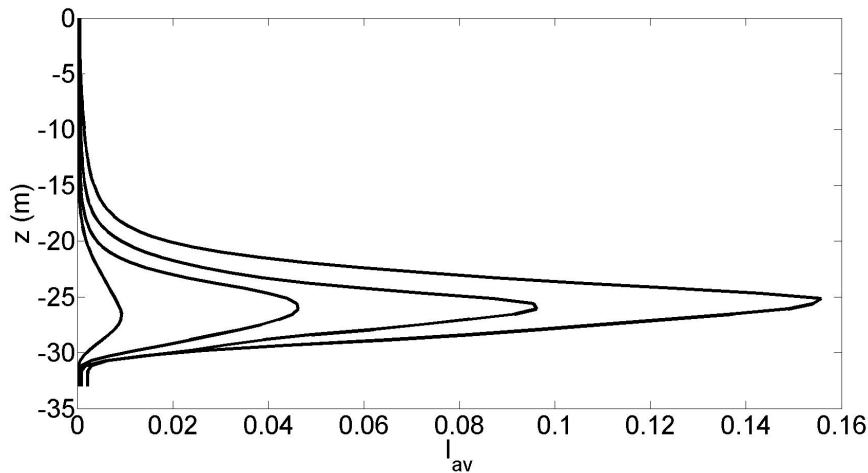


Figure 5.13: Profiles of the average aggregation intensity, $I_{av}(z)$ with increasing phytoplankton maximum growth rate μ_P^{max} . Although not shown the graph, magnitude increases for increasing μ_P^{max} . This was taken for $\mu_P^{max} = (2.16, 4.32, 8.64, 17.28)$ days⁻¹. ($U_* = 3.5 \times 10^{-3}$ ms⁻¹)

optimum depth of each value of μ_P^{max} does not change, as shown in figure 5.14. This would indicate that it is only the flow that z_{opt} is dependent upon, although this hypothesis will be investigated further for other biological parameters. The optimum aggregation intensity, $I_{av}(z_{opt})$, clearly increases with μ_P^{max} (figure 5.15). The increase in $I_{av}(z_{opt})$ is not as large as one might expect, but this is a consequence of the longer periods of extinction and shorter blooms associated with larger μ_P^{max} , which means that the levels of heterogeneity at higher levels of μ_P^{max} are a lot more impressive

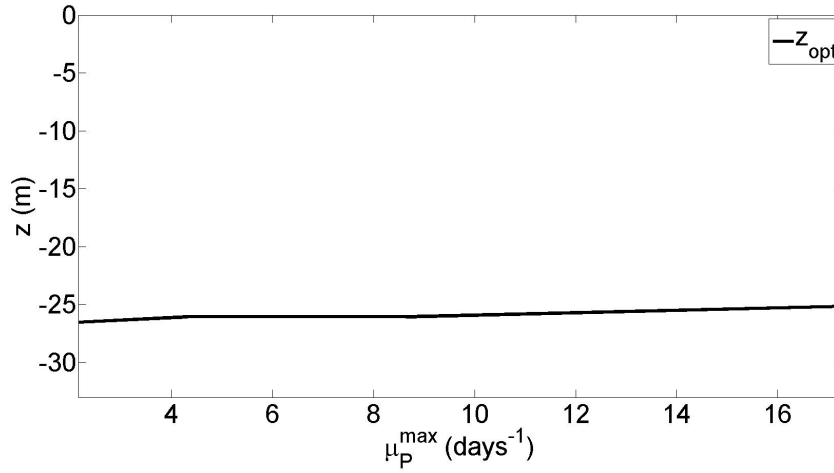


Figure 5.14: Optimum aggregation depth, z_{opt} , for a range of μ_P^{\max} . ($U_* = 3.5 \times 10^{-3} \text{ ms}^{-1}$)

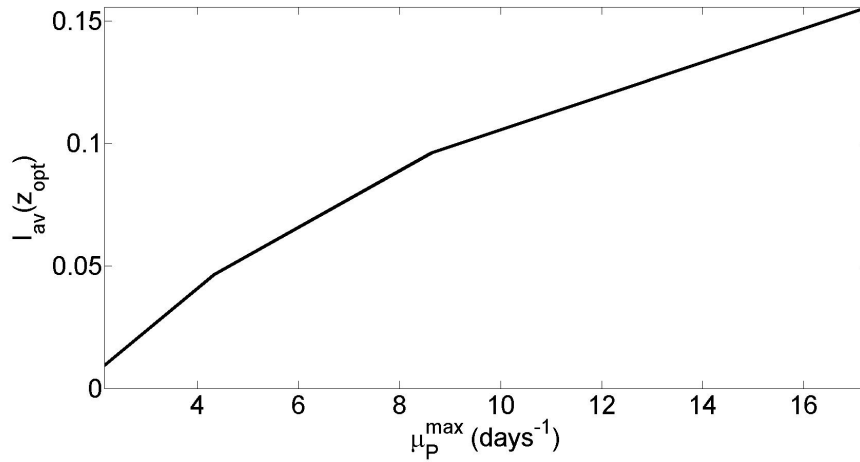


Figure 5.15: Optimum aggregation intensity, $I_{\text{av}}(z_{\text{opt}})$, for a range of μ_P^{\max} . ($U_* = 3.5 \times 10^{-3} \text{ ms}^{-1}$.)

than figure 5.15 shows. The difference in dynamics is much more apparent when comparing $I(z_{\text{opt}}, t)$ for a low and high value of μ_P^{\max} (figure 5.16). The $\mu_P^{\max} = 8.64 \text{ days}^{-1}$ case shows large erratic fluctuations compared to the low $\mu_P^{\max} = 2.16 \text{ days}^{-1}$ case, where a steady (but low) level of I is maintained.

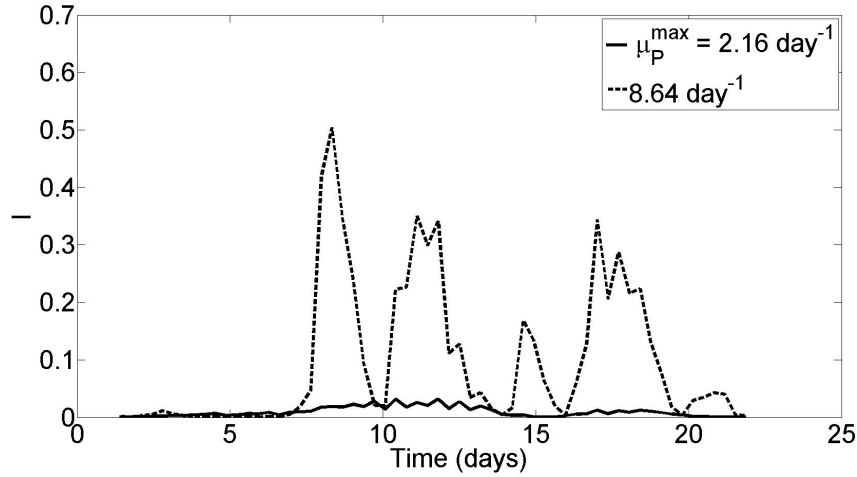


Figure 5.16: Aggregation Intensity for two different μ_P^{max} values at their respective optimum aggregation depth, ≈ 26 m.

Not so surprisingly, there is a positive correlation between μ_P^{max} and I_{av} . We will use similar analysis to find out what effects other biological parameters have on the system and if they change the depth dependence of the aggregation intensity.

5.4.2 Nutrient Pump Strength, Q

The stability analysis for the nitrate concentration is very similar to that of the growth rate, so similar behaviour for intensity is not surprising (see figure 5.17). As the wind stress parameter used here is $U_* = 3.5 \times 10^{-3} \text{ ms}^{-1}$, the place at which aggregation occur most prominently is near the base of the boundary layer. The positive correlation between aggregation intensity and nutrient pump strength is to be expected as the nutrient surge is emanating from the base of the mixed layer. One would expect that the lower wind stress cases lack the vertical mixing capabilities to pull nutrients up from the base of the mixed layer, and so will not be investigated in this section. The graph in figure 5.17 shows only a modest increase in I_{av} as the pump strength is increased. The optimum aggregation depth is 7 metres from the base of the mixed layer, as is shown in figure 5.18 (where again, optimum aggregation depth is unchanging

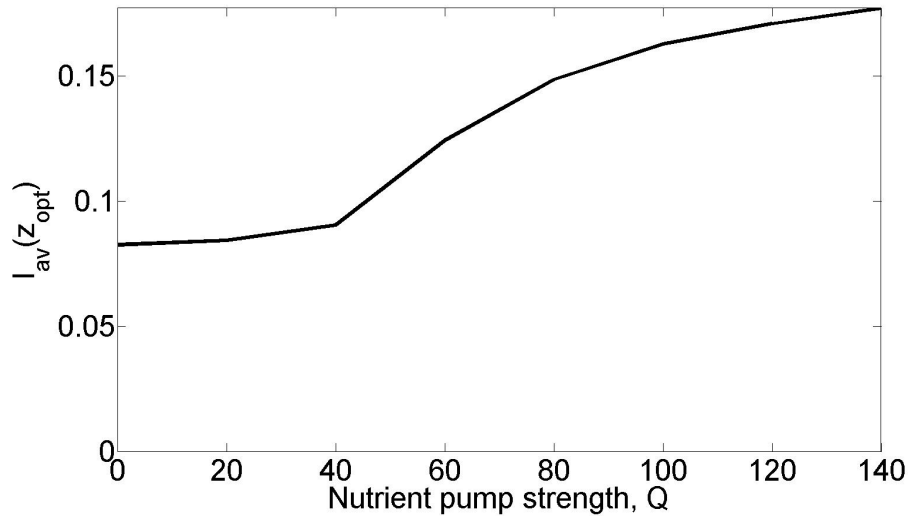


Figure 5.17: Optimum aggregation intensity, $I_{av}(z_{opt})$, for a range of nutrient flux strengths Q . $U_* = 3.5 \times 10^{-3} \text{ ms}^{-1}$

with the biological augmentations). A value of $Q = 130$ will be utilised in subsequent simulations to enhance aggregation signatures.

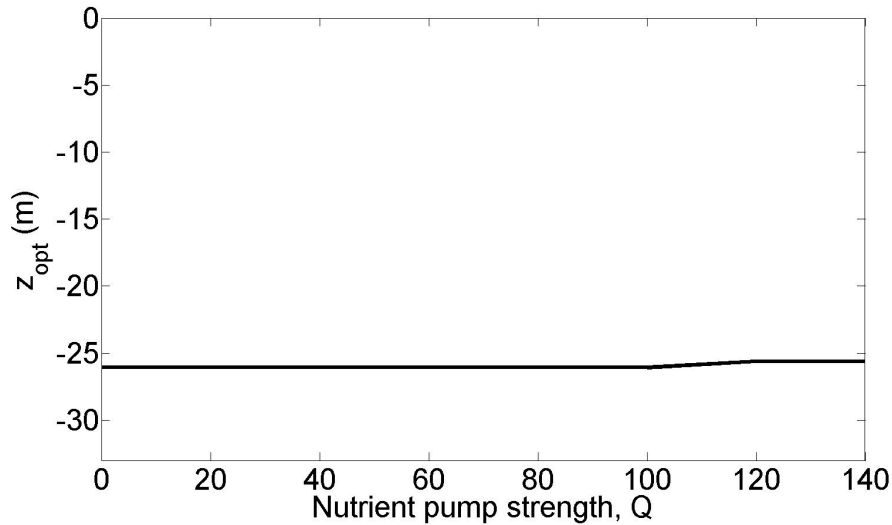


Figure 5.18: Optimum aggregation depth, z_{opt} , for a range of Q .

5.4.3 Zooplankton Contact Radius, R

The dominant parameter which governs this is the zooplankton contact radius, R , due to the predation rate increasing proportional to $R^{\frac{7}{3}}$ (see section 3.2.4).

The stability analysis (section 4.4.2) showed that the dominant effect of changing this parameter was in the equilibrium concentration values, as increasing the predation rate acts to increase Z_{ce} and decrease P_{ce} . This in turn will increase grazing pressure and limit the phytoplankton peak concentrations. With this in mind, it is surprising that $I_{av}(z_{opt})$ decreases by only a factor of one third, when the predation rate is increased by a factor of $\approx 8^{\frac{7}{3}} = 128$ (figure 5.19). One might expect that high predation pressure would markedly reduce the likelihood of any aggregation forming. This outlines the sensitive behaviour of these ecosystems. If the predation rate is strong, the phytoplankton concentration is pushed to near extinction, thereby giving the phytoplankton a small time-frame for recovery. The longer the near extinction phase, the more rapidly the phytoplankton will come back, unless the predation rate is so large that the phytoplankton is kept almost permanently at near extinction levels. The optimum aggregation depth does vary slightly with contact radius, but only in a depth interval of ≈ 3 m, as shown in figure 5.20. This is a better indicator that biology has no significant role in the optimum aggregation depth due to the 2 orders of magnitude increase in the predation rate having no profound effect on the optimum aggregation depth.

In terms of aggregation intensity, high levels are found when the P concentration are pushed to near extinction and is able to explode out of near extinction. However, if the explosion only happens for a very short amount of time before it is pushed back to near extinction (as would happen in the case of high predation), time averages would deplete the large signal. It is this balance of dynamics which makes observations like the one in figure 5.19 not so surprising. So even though the change in predation rate is over a range of 2 orders of magnitude, the change in aggregation intensity only differs

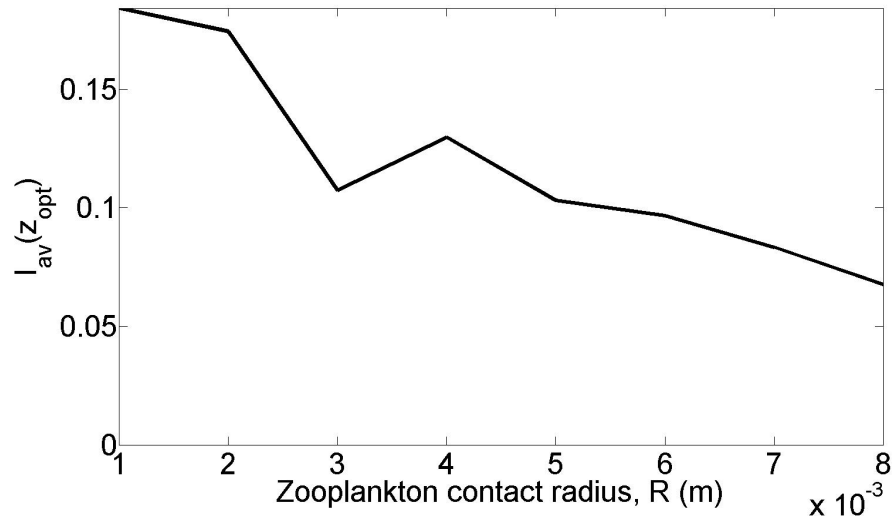


Figure 5.19: Optimum aggregation intensity, $I_{av}(z_{opt})$, for a range of zooplankton contact radius values R m.

by a fraction due to the nature of the system and the qualities of the metric. If it was of interest to see the magnitude of the aggregation during a bloom phase, then an average over the time frame would not be taken and a more suitable metric would be used, but the persistence time of these aggregations are very important and as such this weighting needs to be taken into account.

5.5 Aggregation Depth and Time Persistence

The criteria for a thin phytoplankton layer, given in section 5.1.1, specify that an aggregation must span a range of depths below a certain threshold and that it must last more than a prescribed amount of time. Although we are using aggregation intensity to measure patches, compared with simple concentration ratios, we can still adapt to the criteria in a similar way.

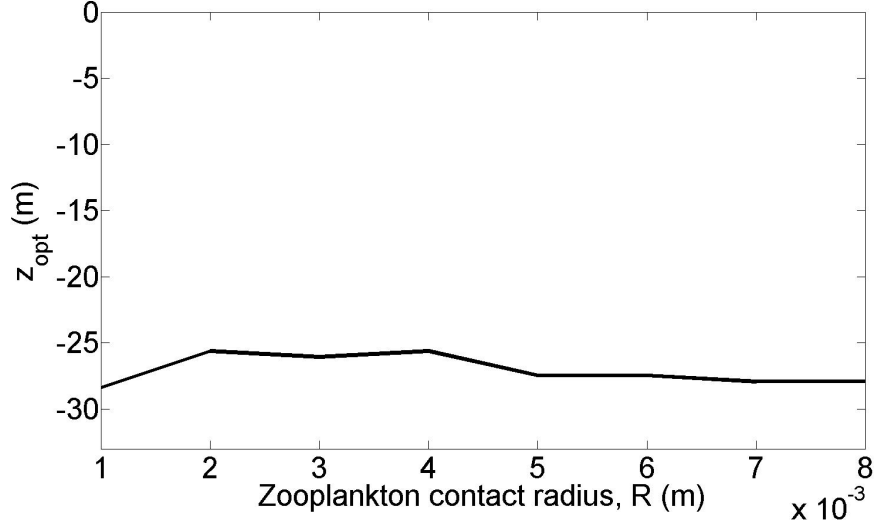


Figure 5.20: Optimum aggregation depth, z_{opt} , for a range of R .

5.5.1 Aggregation Thickness

To define an aggregation thickness in the context of (average) aggregation intensity, I_{av} , we will first define an intensity level to be

$$I_x = x \times \max(I_{\text{av}}), \quad (5.12)$$

where $x \in [0, 1]$ e.g. $I_1 = I_{\text{av}}(z_{\text{opt}})$. Then, we define a length δ_x such that the distance between the two depths which are closest to z_{opt} , z_1 and z_2 , where $z_1 > z_{\text{opt}}$ satisfies $I_x = I_{\text{av}}(z_1)$ and $z_2 < z_{\text{opt}}$ satisfies $I_x = I_{\text{av}}(z_2)$. This is shown graphically in figure 5.21. Then we can simply define our aggregation thickness to be

$$B_\delta = \frac{\delta_{0.25} + \delta_{0.5} + \delta_{0.75}}{3}, \quad (5.13)$$

where B_δ is the aggregation thickness of that particular simulation. In the literature (e.g. Dekshenieks et al. (2001)), an analogous measure of $\delta_{0.5}$ is used to define aggregation thickness. The data that is examined in this work is derived purely from

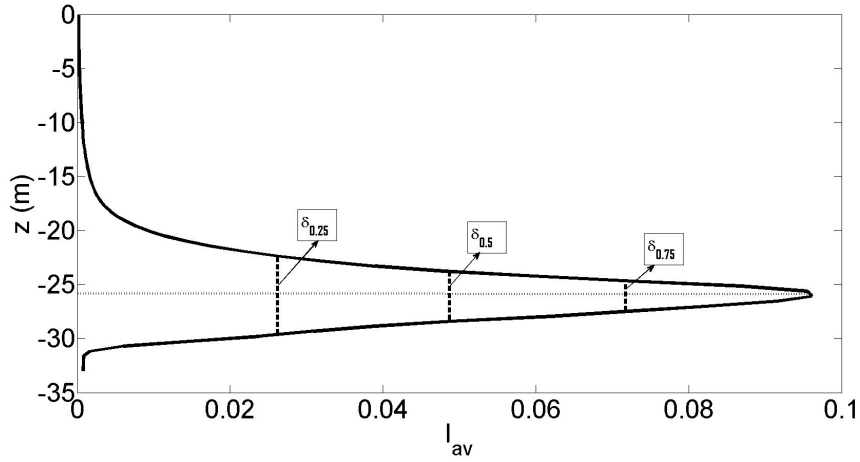


Figure 5.21: Demonstration of how the aggregation thickness is measured. The solid line is a profile of the averaged aggregation intensity, I_{av} , the dashed (vertical) line is the distance metric, δ_x , for $x = (0.25, 0.5, 0.75)$ and the dotted (horizontal) line indicates the optimum aggregation depth, z_{opt} .

simulations, and so doesn't include any noise on any level. Therefore, it is more appropriate in this work to use a slightly more robust measure such as that in equation 5.13, as measurements near the peak intensities are not as sensitive.

Examining the aggregation thickness, B_δ , for simulations of different phytoplankton growth rates and wind stress values, it is observed that the biological parameter is not making much impact as B_δ is distributed similarly for the range of different growth rates (see figure 5.22). However, this is not true for the different levels of wind stress. For low and intermediate wind stress values, aggregation thickness stays roughly around the same value, but once the wind stress exceeds the critical wind stress ($U_* \approx 4 \times 10^{-3} \text{ms}^{-1}$), aggregation thickness increases dramatically, indicative of vertical spreading of the phytoplankton concentration. In other words, the levels of turbulence are high enough to break up the thin aggregation which has been formed and inevitably smooths the concentration field out.

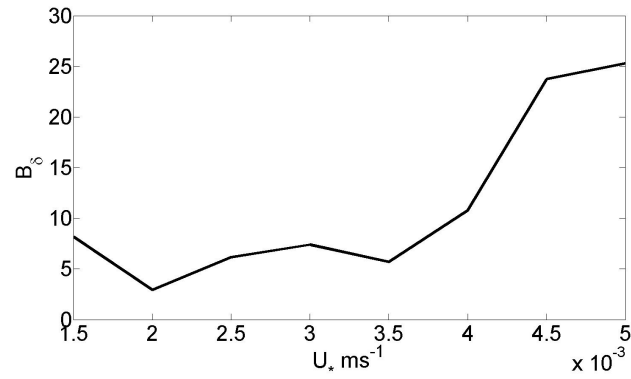
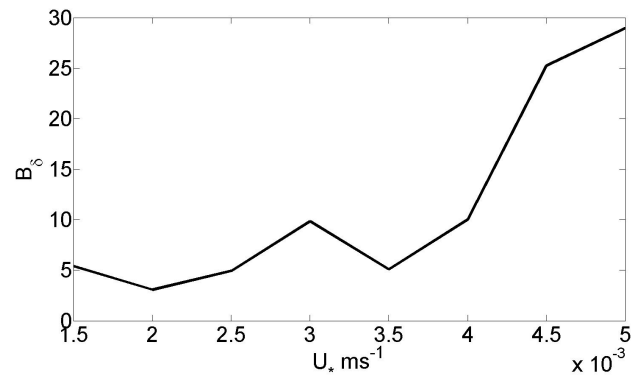
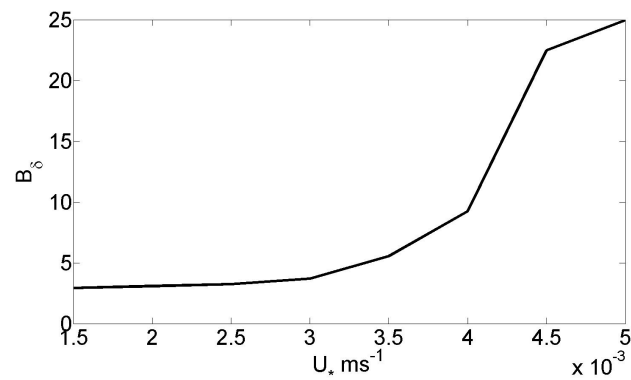
(a) $\mu_P^{\max} = 4.32 \text{ days}^{-1}$ (b) $\mu_P^{\max} = 8.64 \text{ days}^{-1}$ (c) $\mu_P^{\max} = 17.28 \text{ days}^{-1}$

Figure 5.22: Aggregation thickness, B_δ , for three different values of μ_P^{\max} , each measured for a range of wind stress values. ($z_{\text{ML}} = 33\text{m}$)

The scales of the aggregation thickness, for simulations with low to medium wind stress values are $o(5\text{m})$, which is of the same order of that outlined in the literature (Franks, 1995; Deksheniaks et al., 2001; Durham and Stocker, 2012). It must be highlighted that this work neither includes cell swimming nor sharp density gradients which have been proposed as mechanisms for thin layering. Also, due to aggregation thickness being defined by averaged intensities over time, fine scale aggregations which may appear over a range of depths will not be recognised and the depth interval that they appear over will be the prominent signal. This means that the aggregation thickness which is calculated will be very much an upper bound of the actual thickness of the aggregation. Therefore, we can assume that aggregation thickness $o(5\text{m})$ can be regarded as ‘thin’ for the purpose of this work.

In a shallower boundary layer ($z_{\text{ML}} = 20\text{m}$), unsurprisingly, lower aggregation thickness was observed, see figure 5.23. It was also noticed that at the higher end of the wind

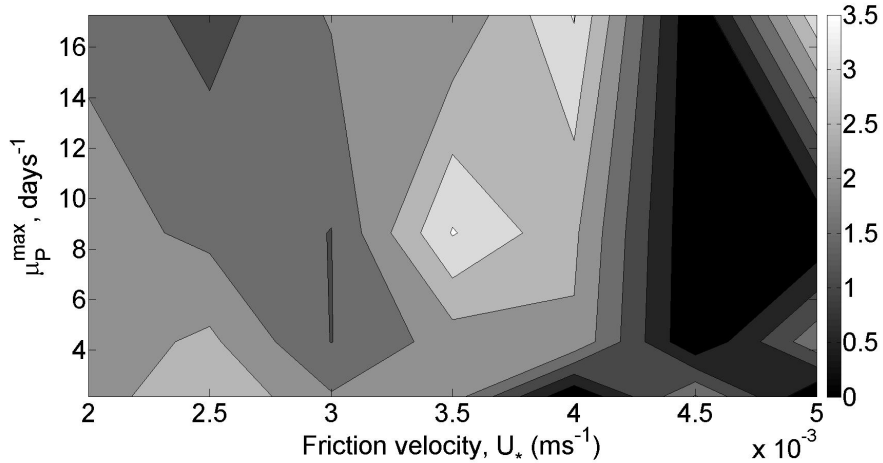


Figure 5.23: Contour plot of the aggregation thickness for a shallow boundary layer, $z_{\text{ML}} = 20\text{m}$, measured for a range of μ_P^{max} and U_* values.

stress spectrum, aggregation thickness drastically decreases, opposite to the behaviour encountered for $z_{\text{ML}} = 33\text{m}$. However due to high wind stress not being realisable for

such a shallow boundary layer, this will be ignored. For a relatively shallow boundary layer, penetration is much easier to achieve and the small portion below where the mixed layer is being penetrated results in a thinner band, where the biology is being able to prevail over the physical forcing. Hence, patches are culminated in the thinner band of laminar stratified fluid. Also, as the nutrient pump is of the same strength to that of the deeper boundary layer, nutrients fill the water column faster and phytoplankton are able to overcome the physical mixing even when the mixed layer has been fully penetrated.

For a much deeper boundary layer, $z_{ML} = 50\text{m}$, penetration is much more difficult to achieve and hence the interval of depths to which the biology dominates becomes larger, see figure 5.24. As for the $z_{ML} = 33\text{m}$ case (figure 5.22), there is a band of wind

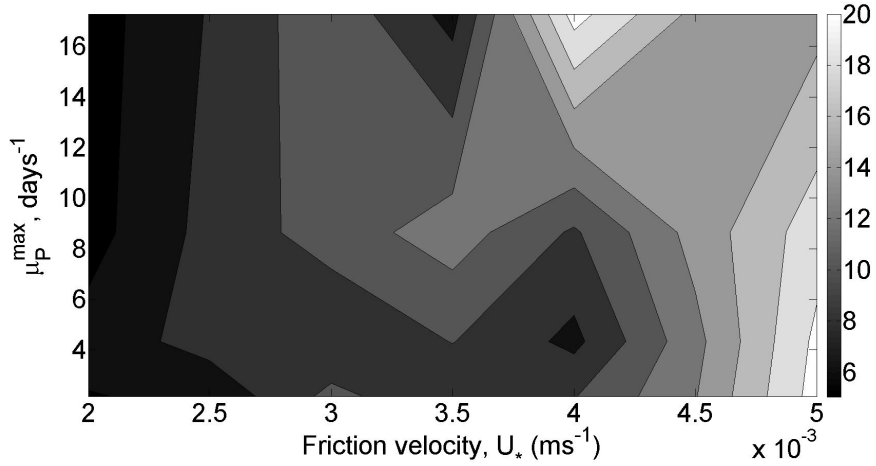


Figure 5.24: Contour plot of the aggregation thickness for a shallow boundary layer, $z_{ML} = 50\text{m}$, measured for a range of μ_P^{\max} and U_* values.

stress values (low to medium) for which the layer thickness stays roughly around the same value. Once the wind stress exceeds the critical wind stress, $U_* \approx 4 \times 10^{-3}\text{ms}^{-1}$, vertical spreading starts and as a result, aggregation thickness increases and the layer breaks up.

5.5.2 Aggregation Time Persistence

To define the aggregation time duration, we will use an analogous approach to that used for the aggregation thickness. Prerequisites will be used before measuring the time scale. For instance, we will use the aggregation optimum depth z_{opt} for analysis (this can be used with confidence as we have deduced that aggregations are spatially persistent around this depth interval by analysing aggregation thickness). We will also take an average time scale as follows. Consider the following function $F_x(t_i)$, defined by

$$F_x(t_i) = \begin{cases} 1 & \text{for } I(z_{\text{opt}}, t_i) > (x \times \max_i [I(z_{\text{opt}}, t_i)]) \\ 0 & \text{otherwise.} \end{cases} \quad (5.14)$$

We can then define the amount of time the aggregation intensity, I , stays above a certain ratio value, x , to be

$$\tau_x = dt \sum_{i=0}^N F_x(t_i), \quad (5.15)$$

where τ_x is the amount of time the intensity stays above a ratio value $x \in [0, 1]$, N is the amount of discrete time points taken (t_N is the total simulation time) and dt is the time-step, which is constant, for example, $\tau_0 = t_N$. τ_x is shown graphically for different values of x in figure 5.25. We can then take a similar average used in calculating the aggregation thickness i.e.

$$B_\tau = \frac{\tau_{0.25} + \tau_{0.5} + \tau_{0.75}}{3 \times t_N}, \quad (5.16)$$

where B_τ is the ratio of the average amount of time the aggregation persists to the total simulation time.

Again, taking different phytoplankton growth rates and analysing B_τ for each growth rate over a range of wind stresses we can gain insight to the persistence of the aggregations, as shown in figure 5.26. Two trends can be discerned from these results. Firstly, the aggregation duration ratio, B_τ , roughly increases with wind stress. This may seem odd on first glance, however, as U_* is increased, z_{opt} decreases and so it is

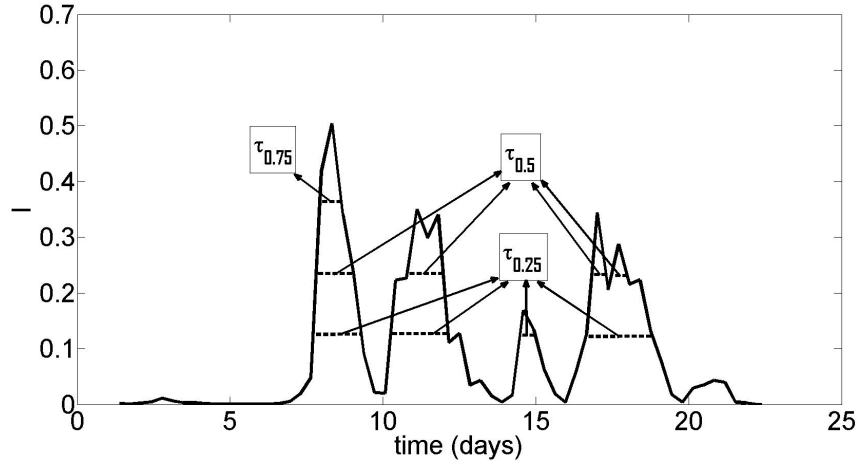


Figure 5.25: Demonstration of how the aggregation time is measured. The solid line is a profile of the aggregation intensity, I , the dashed (horizontal) lines make up the distance metrics, τ_x , for $x = (0.25, 0.5, 0.75)$. The depth at which this will be taken will be at the optimum aggregation depth, z_{opt} .

likely that behaviour is more stable at the depths near to the base of the mixed layer. It was also observed that with increasing growth rate, μ_P^{max} , the persistence time is decreasing slightly. This is not surprising as with higher growth rates comes longer, more intense periods of near extinction followed by explosive growth phases. Hence the relative duration of the growth phase is reduced and this leads to a fall off in persistence time. Aggregations are active in these simulations for roughly between 5% and 20% of the time for $U_* < 4 \times 10^{-3} \text{ms}^{-1}$ which indicates that aggregations last for between 12 hours and 5 days over the 22 day period of these simulations.

For different boundary layer depths, similar behaviour was observed in that persistence time duration roughly decreases with increasing μ_P^{max} (figures 5.27 and 5.28). There is a tendency for the shallower boundary layer aggregations to last more time in the less wind driven regimes. This again is possibly due to stability in the less turbulent waters. We also recall that a shallower boundary layer will have more nutrients contained and there is more light in shallow waters, so growth rates will be larger and

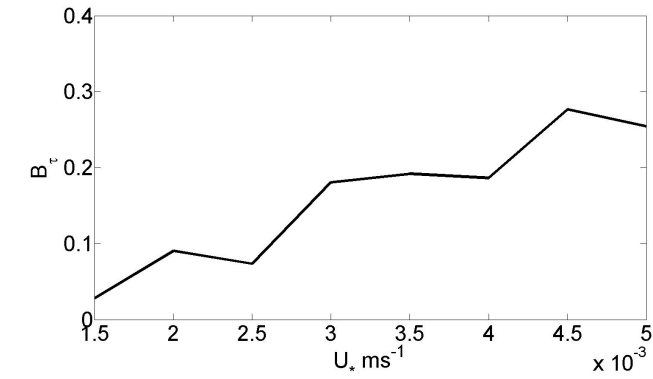
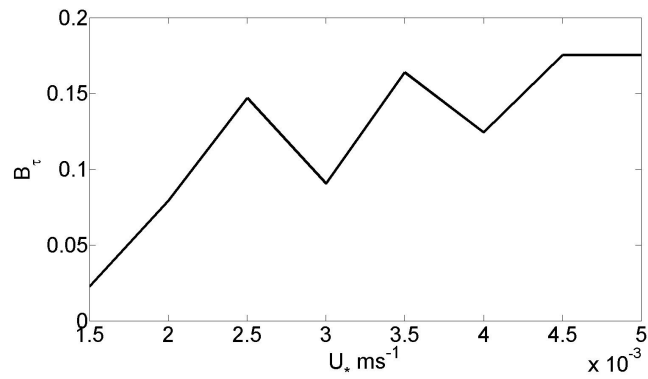
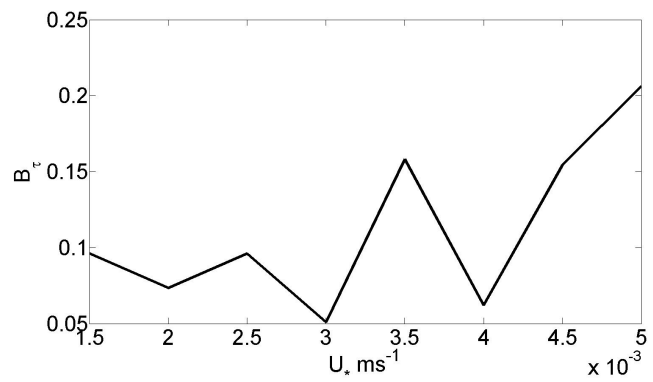
(a) $\mu_P^{\max} = 4.32 \text{ days}^{-1}$ (b) $\mu_P^{\max} = 8.64 \text{ days}^{-1}$ (c) $\mu_P^{\max} = 17.28 \text{ days}^{-1}$

Figure 5.26: Aggregation duration ratio, B_τ , for three different values of μ_P^{\max} , each measured for a range of wind stress values. ($z_{\text{ML}} = 33\text{m}$.)

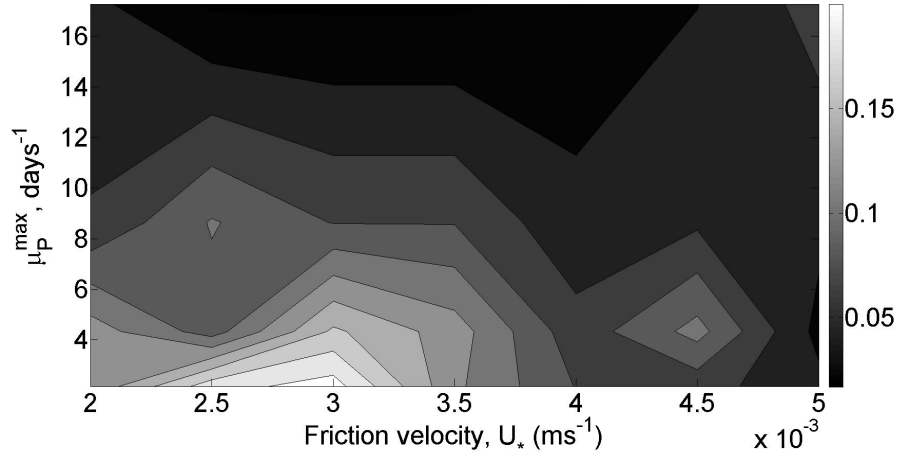


Figure 5.27: Contour plot of the aggregation time ratio, B_τ , for a shallow boundary layer, $z_{ML} = 20\text{m}$, measured for a range of μ_P^{max} and U_* values.

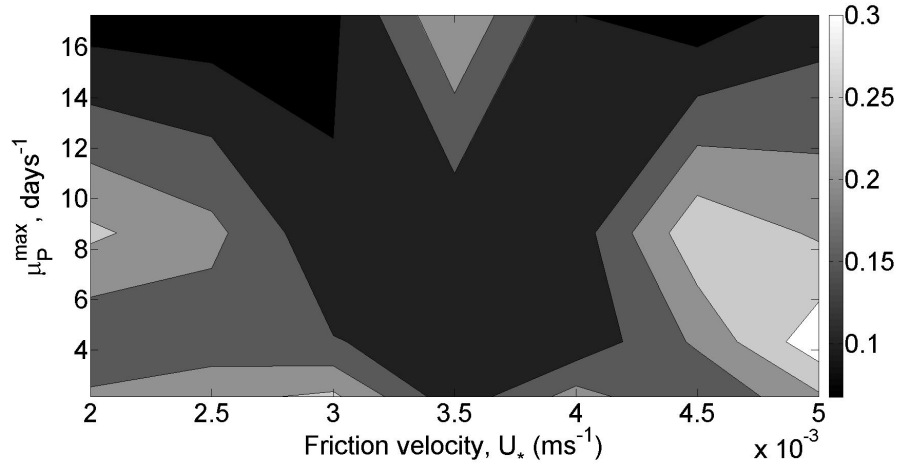


Figure 5.28: Contour plot of the aggregation time ratio, B_τ , for a shallow boundary layer, $z_{ML} = 50\text{m}$, measured for a range of μ_P^{max} and U_* values.

consequently, extinction phases will be prolonged, accounting for the lower overall time persistence than the deeper boundary layer cases. This also serves as a reason for time persistence to be larger in the deeper boundary layer ($z_{ML} = 50\text{ m}$).

In general, it can be inferred that both B_δ and B_τ increase as z_{ML} is increased. This indicates that, like with a lot of things, a compromising boundary layer depth is needed to give a low value of B_δ while still keeping B_τ at a reasonable level. This again comes down to threshold definitions, but examining the results, it clarifies that a boundary layer depth somewhere between the shallow and deep boundary layer will suffice keep a good contrast between aggregation thickness and aggregation time persistence.

5.6 Aggregation Distributions

Many simulations have been completed for this work and so a select few simulations will be used to quantify what intensity means in terms of levels of heterogeneity. The results shown here contain the highest levels of optimum aggregation intensity, $I_{av}(z_{opt})$, reasonably thin aggregations ($< 10m$) and temporal persistence ($> 10\%$) for a boundary layer of depth $z_{ML} = 33m$. Firstly, for optimum intensity, we examine the parameter space over wind stress, U_* and maximum phytoplankton growth rate, μ_P^{max} , to find conditions which permit high intensity (see figure 5.29). The top 4 intensity values

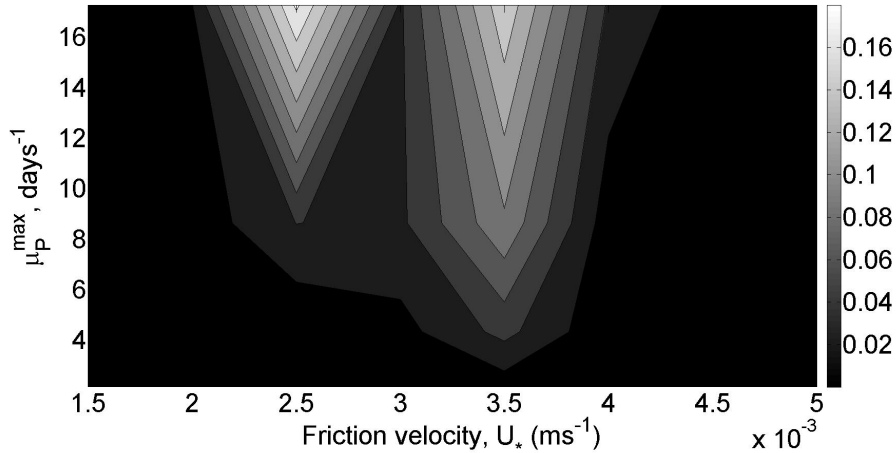


Figure 5.29: Contour plot of the optimum aggregation intensity, $I_{av}(z_{opt})$, for a boundary layer, $z_{ML} = 33m$, measured for a range of μ_P^{max} and U_* values.

here are at $(U_*, \mu_P^{max}) = (2.5, 17.28)$, $(3.5, 4.32)$, $(3.5, 8.64)$, $(3.5, 17.28)$, $(4, 17.28)$

(note - (x, y) refers to $(x \times 10^{-3} \text{ ms}^{-1}, y \text{ days}^{-1})$). This shows that phytoplankton clearly thrive when they have a higher growth rate. However, it is surprising that they thrive so well with a relatively low growth rate when the physical forcing conditions are ideal compared to lower wind stress cases with much higher growth rates. This highlights the importance of the moderate levels of turbulence in the boundary layer, which acts to enhance heterogeneity.

5.6.1 Physical and Biological Correlation

To have a better idea of the mechanisms in this system, we will analyse one simulation, namely the case when $(U_*, \mu_P^{max}) = (3.5, 4.32)$. In particular, we will examine what happens in a primary and secondary surge in intensity during a phytoplankton bloom (An example of a primary and secondary intensity surge is shown in figure 5.2). For the primary surge in intensity (shown in figure 5.30), nutrients are being entrained by upwellings ($w > 0$) (figures 5.30(c) and 5.30(d)). Phytoplankton are responding to this by growing at high nutrient concentrations (and hence in upwelling regions), which has a domino effect on the zooplankton to grow in high phytoplankton regions. The secondary surge (figure 5.31) indicates that zooplankton have consumed the initial high concentration of P , which is why there is a negative correlation between figures 5.31(b) and 5.31(a). Although the P concentration is already satiated in the primary surge, this cycle still occurs because correlations are periodic, with the same period as the biological cycles. This means that this behaviour was stimulated at the beginning of the simulation and fixed itself in this laterally ‘out of phase’ dynamic.

The flow field governs how large or small a patch is, as the shape of the distribution is governed by the upwellings and downwellings. When the nutrient field reaches satiation levels, it can have no further effect on intensifying heterogeneity. However, if there was a small scale mechanism present to further enhance localised growth, then this would enhance aggregation signals. This serves as a link between the small scales and the large scales, as small scale enhancements, such as vortical trapping from gy-

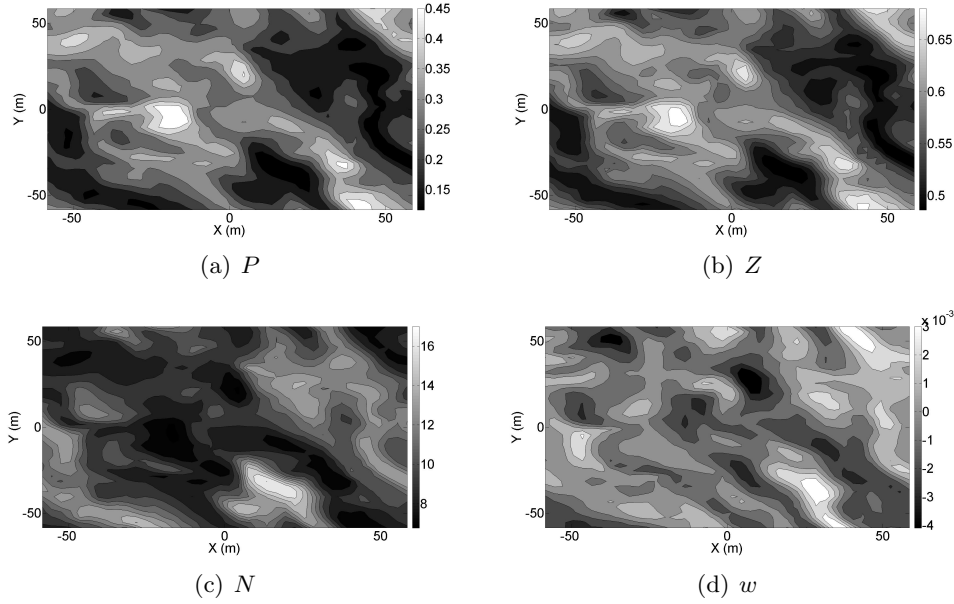


Figure 5.30: Biological and physical distributions at the primary aggregation intensity surge, at the optimum depth, $z_{\text{opt}} \approx 26$ m. In the biological fields, white indicates a relatively high concentration and black a relatively low concentration. For the physical field, namely w , white indicates an upwelling and black indicates a downwelling.

rotaxis (Durham et al., 2011c), would have the most prominent effect when biological levels are near extinction. This small scale structure generated near extinction would manifest in a large scale structure once the bloom takes place.

Now that mechanisms behind spatial structure of biological concentration have been examined and how they change in time, we will next examine the extent to which the phytoplankton can take advantage of the biological and physical distributions.

5.6.2 Phytoplankton Structures

For the four chosen simulations with largest intensity, we will analyse primary surges (at and around the aggregation intensity peaks) at the optimum aggregation depth z_{opt} . To simplify things, we will assign a simulation number to each case from ‘simulation 1’ to ‘simulation 4’ with ‘simulation 1’ being the smallest optimum aggregation intensity

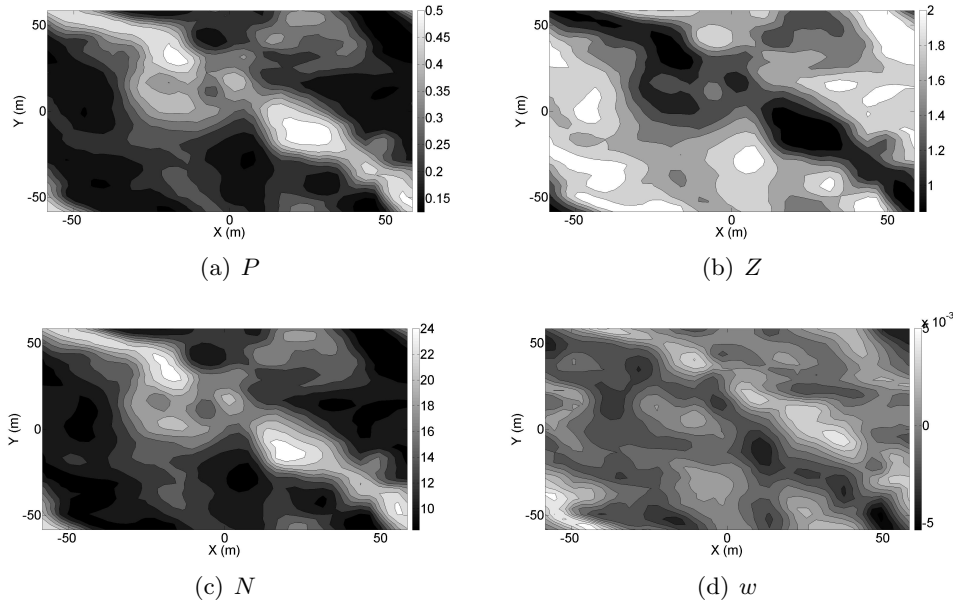


Figure 5.31: Biological and physical distributions at the secondary aggregation intensity surge, at the optimum depth, $z_{\text{opt}} \approx 26$ m.

value and ‘simulation 4’ being the largest.

Simulation 1 - $(U_*, \mu_P^{\text{max}}) = (3.5, 4.32)$

Simulation 2 - $(U_*, \mu_P^{\text{max}}) = (3.5, 8.64)$

Simulation 3 - $(U_*, \mu_P^{\text{max}}) = (3.5, 17.28)$

Simulation 4 - $(U_*, \mu_P^{\text{max}}) = (2.5, 17.28)$

Simulation 1

This simulation shows that, while intensity is lower, on the whole, when compared to the higher growth rate counterparts (simulations 2-4), intensity surges last for longer periods of time. Analysing just two points in the primary aggregation intensity surge, one point at a maximum and the other further in time at around half the intensity (but at a higher mean $\langle P \rangle$ value) we can see that figure 5.32(b) is at a relatively low concentration but the maximum value is more than 3 times the minimum. Phytoplankton

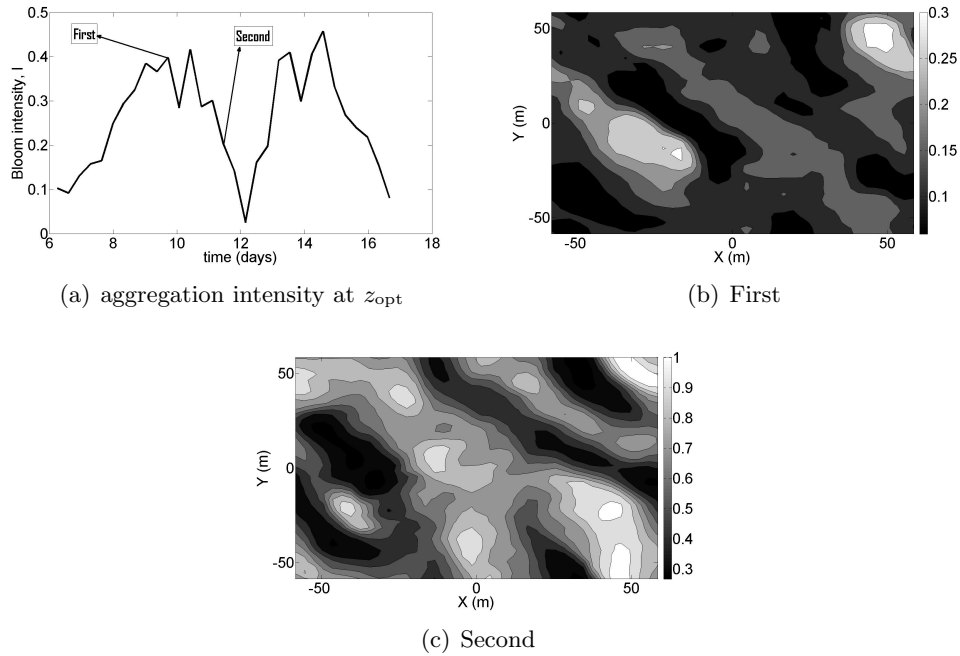


Figure 5.32: Figure 5.32(a) indicates the times at which P distributions shown in figures 5.32(b) and 5.32(c) are taken at. Taken at the the optimum aggregation depth z_{opt} : Simulation 1.

concentrations then grow exponentially, keeping the same level of heterogeneity (i.e. $\max P \approx 3 \times \min P$), as shown in figure 5.32(c).

Simulation 2

Here one observes a similar distribution to simulation 1 except with a greater difference from the minimum phytoplankton concentration to the maximum concentration (figures 5.33(b) and 5.33(c)). We also see that the peak in intensity happens at a much lower concentration of P which means heterogeneity has been able to manifest itself more quickly, before zooplankton can take advantage, a consequence of higher growth rates. This level of heterogeneity is able to sustain itself for longer giving a large difference between minimum and maximum P concentrations.

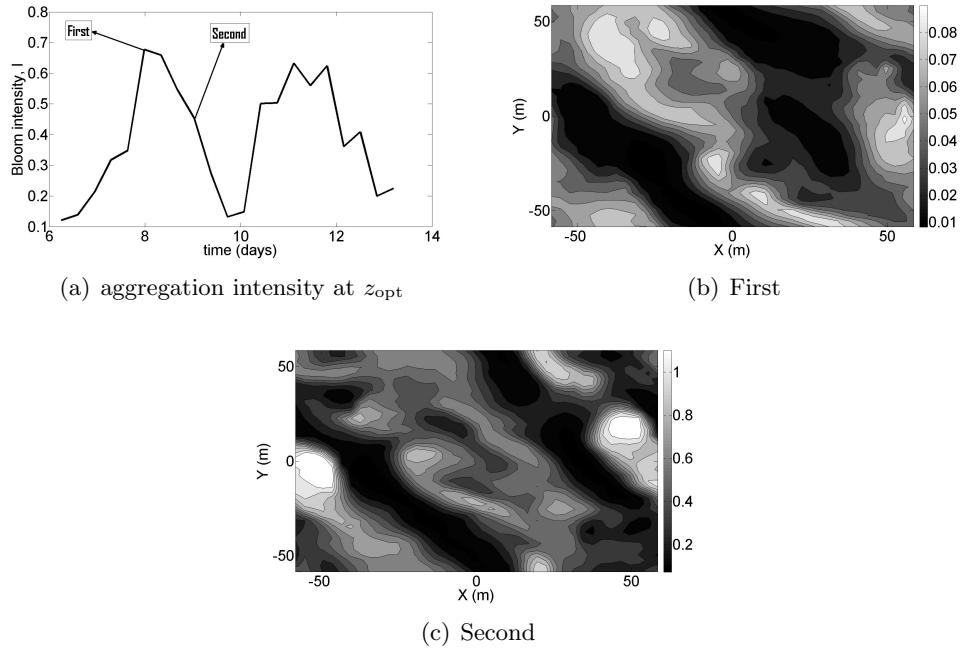


Figure 5.33: Figure 5.33(a) indicates the times at which P distributions shown in figures 5.33(b) and 5.33(c) are taken at. Taken at the the optimum aggregation depth z_{opt} : Simulation 2.

Simulation 3

The distribution of these aggregations is a little different to those shown in the previous simulations as the patches are slightly smaller, giving a larger intensity value (figures 5.34(b) and 5.34(c)). As this growth rate is so large, the biological cycle of high concentration is nearly completely decoupled from the biological cycle of the low concentration. Decoupling in this sense means regions of low concentration are still near extinction, about ready to move into an explosive growth phase. The high concentration regions are ready to collapse, so the two regions of concentration are effectively evolving independently to one another. It is this decoupling which is the prominent mechanism behind high aggregation signals.

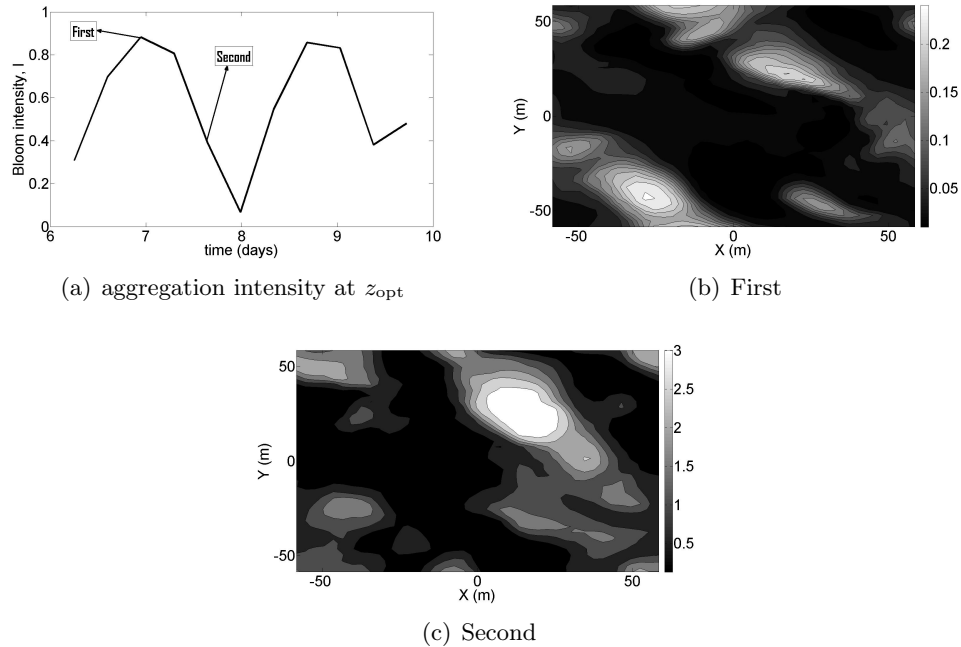


Figure 5.34: Figure 5.34(a) indicates the times at which P distributions shown in figures 5.34(b) and 5.34(c) are taken at. Taken at the the optimum aggregation depth z_{opt} : Simulation 3.

Simulation 4

In this case the wind stress is much lower than simulation 3. This change is apparent in the distributions. As the aggregations are occurring higher in the mixed layer, the flow is a more dominant feature of the environment and, due to the Stokes drift being more prominent at higher depths, the biological concentrations are elongated out at roughly 45 degrees to the direction of wind stress. As a result, patches are more concentrated in smaller areas, which increases the aggregation intensity. As there is a higher growth rate it was again observed that the high concentration patches are decoupling, to some extent, from the low concentration surroundings which is yet to break out of its near extinction phase.

In short, there are both biological and physical reasons for aggregations in the model.

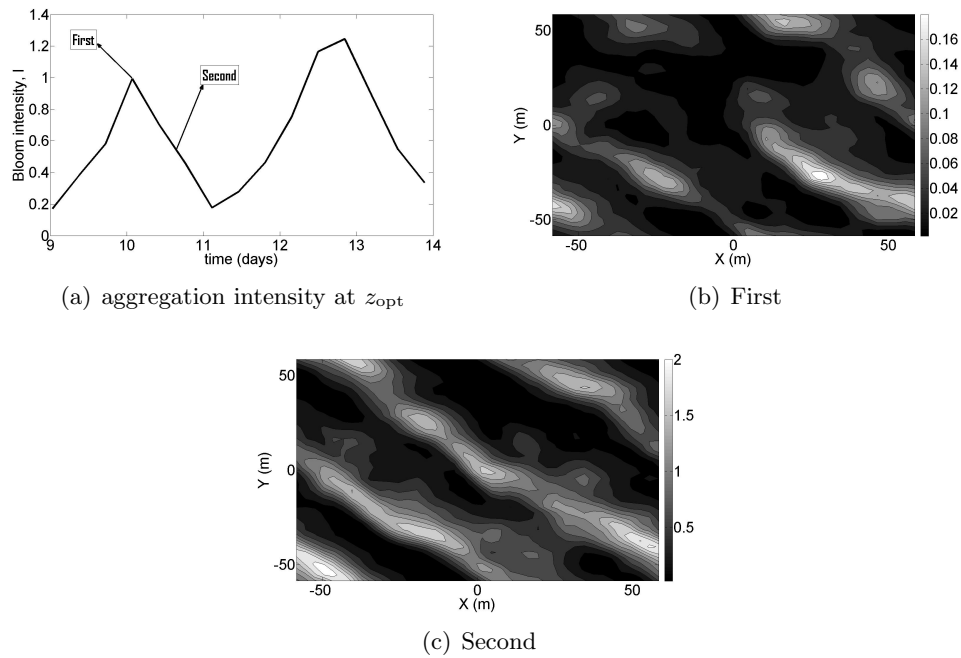


Figure 5.35: Figure 5.35(a) indicates the times at which P distributions shown in figures 5.35(b) and 5.35(c) are taken at. Taken at the the optimum aggregation depth z_{opt} : Simulation 4.

Firstly, the flow field needs to have a certain level of activity to promote considerable upwelling at the base of the boundary layer, as to pull nutrients up from the source. Secondly, Langmuir cells help bias the biological fields laterally, principally into 2 regions, high nutrient level upwelling and relatively low nutrient level downwelling. This promotes biased levels of growth rates and hence stimulates lateral heterogeneity in the plankton. This mechanism for aggregation can be further enhanced by increasing phytoplankton growth rates. This enhances aggregation because dynamics become more erratic around equilibrium and spend time near extinction where dramatic population increases follow and aggregations become much more prominent.

Chapter 6

Summary

6.1 Discussion

When analysing a complex coupled bio-physical model, especially one associated with 3-dimensional turbulent flow field, one needs to understand the components of the physical model and the biological model separately.

Exploration of the physical model in this study revealed that even advanced LES codes are not exempt from numerical error. We found numerical errors built up in statistical moments of the flow field owing to low levels of turbulence in the boundary layer. This meant that the time-step was allowed to increase to a level that was too large for statistical stability to be sustained. However, this was remedied by putting a cap on how large the maximum extent of the time-step. This was also treated, to a certain extent, with the use of a Langmuir turbulent boundary in which wave forcing was permitted. This extra energy from the wave forcing was an ideal solution to increase the levels of turbulence, which made the time-stepping regime more suitable to simulations (but a time-step cap was still needed for low wind stress simulations).

High turbulent mixing dissipates any concentration to homogeneity if that concentration cannot overcome the turbulent flow in some way (which is true of zooplankton

and phytoplankton). For heterogeneity to manifest itself in a turbulent boundary layer, there must be areas of low turbulent mixing and furthermore heterogeneous structures in the flow field which will instigate heterogeneity in the biology. It was found that as turbulence was depth dependant, we would need turbulent mixing (characterised by the energy dissipation rate $\langle \epsilon \rangle$) to be low and vertical mixing (characterised by the vertical velocity variance $\langle w^2 \rangle$) to be at a reasonable level to pull up nutrients which were emanating from the base of the boundary layer, but not too high as to fully mix the entire boundary layer. We then established how the boundary layer was split up into a turbulent layer near the surface and laminar layer near the base of the boundary layer by defining a penetration depth, z_{pen} , which was the depth of division between the two layers. It was hypothesised that aggregations would form in the laminar layer (with appropriate levels of vertical mixing) where turbulent mixing would not be prominent.

The biological model used in the LES-NPZ model was fairly complex as it included the use of mechanistic approaches in the derivation of some parameters, some of which were depth-dependant parameters. To make things simple however, we assumed all parameters were constant so that we could use linear stability analysis. This is useful for a number of reasons. It gives a good qualitative view of the dynamics of the biology, showing the general effects of certain parameters. In particular, we found that increasing the phytoplankton growth rate and the nitrate concentration had the effect of allowing the phytoplankton bloom to reach a higher concentration, decreasing the amount of time the bloom lasted and increasing the amount of time phytoplankton stayed near extinction, which we later found to be desirable for phytoplankton aggregations. If a parameter search was undertaken in the LES-NPZ model, each simulation would take around 2-3 weeks to complete to get any results, whereas the simple model takes seconds to run. So the simple model gives an initial basis and parameter range to start searching the parameter space in the LES-NPZ model.

To define heterogeneity, we used a statistic, I , used in (Lewis, 2005), which gave the

level of heterogeneity without taking into account the level of concentration. Then, observing how this statistic evolved in time revealed how the levels of heterogeneity corresponded to the concentration field of P . To really understand what was driving this heterogeneity, we decomposed the dynamics of I in an attempt to understand which biological or physical processes were inducing or inhibiting heterogeneity. We found that for a test case, at the optimum phytoplankton aggregation depth, z_{opt} , it was the biology which was dominating the effects from the flow field, most likely because z_{opt} is deeper in the boundary layer where the environment is quiescent. This gives an indication that decomposing the dynamic statistics is a useful technique to find how much effect the flow has on the aggregations in certain regions.

Going back to the physical model analysis, we used a parameter, z_{pen} , to distinguish the depth at which turbulent flow and laminar flow split up. To examine how the biology fits in to this divided boundary layer, we defined an optimum aggregation depth, z_{opt} , at which phytoplankton reach a relatively high sustained level of heterogeneity. The correlation between z_{opt} and z_{pen} was striking. We found

$$z_{\text{pen}} > z_{\text{opt}} > z_{\text{ML}}, \quad (6.1)$$

where z_{ML} was the depth of the boundary layer. This implies that as z_{pen} decreases (from increasing wind stress) the optimum aggregation is pushed deeper towards the nutrient source and is compressed in the vertical axis. In the upper level (above z_{pen}) turbulent mixing is high and hence this region is similar to the upper mixed layer in the ocean. Whereas, the region below z_{pen} is relatively quiescent with some levels of vertical mixing, which is has similar properties to that of the pycnocline. The pycnocline is a typical region for phytoplankton aggregations to be found, but the reason given forward is density stratification of neutrally buoyant phytoplankton cells. This coincidence may increase levels of heterogeneity beyond what is found in this model, as variable density effects are not incorporated here.

Levels of aggregation intensity increase dramatically when the phytoplankton population recovers from a near extinction phase. This level of heterogeneity is apparent when the population has a much larger growth rate (owing to species type and/or nutrient levels). This is due to heterogeneity on the micro-scale being relatively large (despite the very low concentration), when the growth spurt occurs, the heterogeneity level stays the same but at a larger concentration, this makes the aggregation very distinctive. Furthermore, assuming the lateral phytoplankton concentration field is split up into two regions (from heterogeneous nutrient upwellings), then for a high growth rate, these two regions become very out of phase with each other. In other words, one region goes through a phase of growth and decay, whilst the second region goes through the same process, just a short time period later. This mechanism increases aggregation intensity drastically as there will come some points in time when the first region is at a high concentration and the second region still near extinction. For a thin layer aggregation to form, phase decoupling between lateral phytoplankton concentrations must happen on a small interval of depths, which will happen when physical conditions are right.

In conclusion, large scale phytoplankton aggregations are very dependent upon the properties of the flow field. Turbulent mixing is a very preferential process for the culmination of thin phytoplankton aggregations in that it dampens aggregations in a large interval of depths (near the surface), leaving a small interval of depths (near the base of the boundary layer) to remain biologically active. A link has also been made to the interaction between small scale processes and large scale processes via 'explosion from near extinction'. This implies that small scale processes are realisable when a large surge in population takes place.

6.2 Future Work

This work has opened up many new avenues for future research. For example

1. A study into the effect of the nutrient source. In this thesis, the nutrient pump has been made Gaussian in the hope that it will stimulate heterogeneity, but does this actually help? Investigation into the difference in spatial heterogeneity in phytoplankton distribution stemming from a non-uniform and uniform nutrient source will help clarify the mechanism behind the heterogeneous phytoplankton distribution - the spatial extent of the nutrient surge itself, or the upwellings and downwellings associated with the flow.
2. We have discovered that heterogeneity is most abundant when the dynamics of the biology are more oscillatory (when near extinction phases are permitted). Does this mean that non-oscillatory biological population dynamics must stay homogeneous? Taking initial conditions at co-existence equilibriums, we can see if patches are formed from the biology, or if they are formed from the physical forcing alone.
3. When running simulations of a turbulent flow field, spatial and time resolutions need to be set such that statistical stability holds. This means that simulations run only slightly faster than real-time due to the amount of spatial and time resolution needed for stable solutions. Investigations should therefore go towards making computations more efficient. There is a plethora of spatial numerical methods to choose from, so these should be implemented in order to increase productivity. There is also the matter of the failing dynamical time stepping regime when turbulence levels are low. A time stepping regime should be implemented to account for low turbulence levels to further improve efficiency of simulations.
4. Fixed wind forcing has been employed for these simulations to see the long term effect of each flow regime on the biology. However, it is not realistic that wind

would remain at a constant level. Incorporation of a variable wind stress in to either look at simple behaviour such as a two-mode (high-low) wind stress regime to account for generic changes in weather in the night and the day, or to use experimental wind stress data.

5. An investigation into the enhancing mechanisms in the literature could be used to see how much it helps bring out planktonic aggregations. The easiest to implement is density stratification and incorporating buoyancy into the planktonic dynamics to see how much of a role density stratification plays.
6. Finally, a parameter set has been found which gives ideal conditions for thin phytoplankton aggregation to occur. Parallelisation of the LES-NPZ code could be completed to investigate the dynamics of this parameter set. For example, a larger horizontal domain, or a finer grid resolution could be used for comparison.

Bibliography

Mark R Abbott and Philip M Zion. Satellite observations of phytoplankton variability during an upwelling event. *Continental Shelf Research*, 4(6):661–680, 1985.

Edward R Abraham. The generation of plankton patchiness by turbulent stirring. *Nature*, 391(6667):577–580, 1998.

Alice L Alldredge, Timothy J Cowles, Sally MacIntyre, Jan EB Rines, Percy L Donaghay, Charles F Greenlaw, DV Holliday, Margaret M Dekshenieks, James M Sullivan, and J Ronald V Zaneveld. Occurrence and mechanisms of formation of a dramatic thin layer of marine snow in a shallow pacific fjord. *Marine Ecology Progress Series*, 233(1), 2002.

S Alvain, C Moulin, Yves Dandonneau, and H Loisel. Seasonal distribution and succession of dominant phytoplankton groups in the global ocean: A satellite view. *Global Biogeochemical Cycles*, 22(3), 2008.

Laura Lucero Álvarez-Molina, Saul Álvarez-Borrego, José Rubén Lara-Lara, and SG Marinone-Moscheto. Annual and semiannual variations of phytoplankton biomass and production in the central gulf of california estimated from satellite data. *Ciencias Marinas*, 39(2):217–230, 2013.

RF Anderson, S Ali, LI Bradtmiller, SHH Nielsen, MQ Fleisher, BE Anderson, and LH Burckle. Wind-driven upwelling in the southern ocean and the deglacial rise in atmospheric co₂. *Science*, 323(5920):1443–1448, 2009.

- Mark E Baird and Steve M Emsley. Towards a mechanistic model of plankton population dynamics. *Journal of Plankton Research*, 21(1):85–126, 1999.
- Mark E Baird, Steve M Emsley, and Jacqueline M Mcglade. Modelling the interacting effects of nutrient uptake, light capture and temperature on phytoplankton growth. *Journal of Plankton Research*, 23(8):829–840, 2001.
- NS Banas, EJ Lessard, RM Kudela, P MacCready, TD Peterson, BM Hickey, and E Frame. Planktonic growth and grazing in the columbia river plume region: A biophysical model study. *Journal of Geophysical Research: Oceans (1978–2012)*, 114(C2), 2009.
- JW Baretta, W Ebenhöh, and P Ruardij. The european regional seas ecosystem model, a complex marine ecosystem model. *Netherlands Journal of Sea Research*, 33(3):233–246, 1995.
- JG Baretta-Bekker, JW Baretta, and W Ebenhöh. Microbial dynamics in the marine ecosystem model ersem ii with decoupled carbon assimilation and nutrient uptake. *Journal of Sea Research*, 38(3):195–211, 1997.
- George K Batchelor. Mass transfer from small particles suspended in turbulent fluid. *Journal of Fluid Mechanics*, 98(03):609–623, 1980.
- George Keith Batchelor. *The theory of homogeneous turbulence*. Cambridge university press, 1953.
- Kelly J Benoit-Bird, Mark A Moline, Chad M Waluk, and Ian C Robbins. Integrated measurements of acoustical and optical thin layers i: Vertical scales of association. *Continental Shelf Research*, 30(1):17–28, 2010.
- Daniele Bianchi, Charles Stock, Eric D Galbraith, and Jorge L Sarmiento. Diel vertical migration: Ecological controls and impacts on the biological pump in a one-dimensional ocean model. *Global Biogeochemical Cycles*, 2013.

- Daniel A. Birch, William R. Young, and Peter J.S. Franks. Thin layers of plankton: Formation by shear and death by diffusion. *Deep Sea Research Part I: Oceanographic Research Papers*, 55(3):277 – 295, 2008.
- Jan E Bissinger, David JS Montagnes, Jonathan Sharples, and David Atkinson. Predicting marine phytoplankton maximum growth rates from temperature: Improving on the eppley curve using quantile regression. *Limnology and Oceanography*, 53(2): 487, 2008.
- Jennifer M Brown and Judith Wolf. Coupled wave and surge modelling for the eastern irish sea and implications for model wind-stress. *Continental Shelf Research*, 29(10): 1329–1342, 2009.
- Marie H Bundy, Thomas F Gross, Henry A Vanderploeg, and J Rudi Strickler. Perception of inert particles by calanoid copepods: behavioral observations and a numerical model. *Journal of Plankton Research*, 20(11):2129–2152, 1998.
- Hans Burchard, Karsten Bolding, and Manuel R Villarreal. *GOTM, a general ocean turbulence model: Theory, implementation and test cases*. Space Applications Institute, 1999.
- James A. Carton, Semyon A. Grodsky, and Liu Hailong. Variability of the oceanic mixed layer, 1960–2004. *Journal of Climate*, 21(5):1029 – 1047, 2008.
- Changsheng Chen, Geoffery Cowles, and RC Beardsley. An unstructured grid, finite-volume coastal ocean model: Fvcom user manual. *SMAST/UMASSD*, 2006.
- OM Cheriton, MA McManus, MT Stacey, JV Steinbuck, and JP Ryan. Physical and biological controls on the maintenance and dissipation of a thin phytoplankton layer. *Mar. Ecol. Prog. Ser.*, 378:55–69, 2009.
- James E Cloern. Tidal stirring and phytoplankton bloom dynamics in an estuary. *Journal of marine research*, 49(1):203–221, 1991.

- Timothy J Cowles and Russell A Desiderio. Resolution of biological microstructure through in situ fluorescence emission spectra. *Oceanography*, 6(3):105–111, 1993.
- PM Cox, RA Betts, CD Jones, SA Spall, and IJ Totterdell. Acceleration of global warming due to carbon-cycle feedbacks in a coupled climate model. *Nature*, 408(6809):184–187, 2000.
- John Crank. *The mathematics of diffusion*. Oxford university press, 1979.
- Roger Cropp and John Norbury. Simple predator-prey interactions control dynamics in a plankton food web model. *Ecological Modelling*, 220(1314):1552 – 1565, 2009.
- JJ Cullen and RW Eppley. Chlorophyll maximum layers of the southern-california bight and possible mechanisms of their formation and maintenance. *Oceanologica Acta*, 4(1):23–32, 1981.
- Peter Alan Davidson. *Turbulence: An Introduction for Scientists and Engineers: An Introduction for Scientists and Engineers*. Oxford University Press, 2004.
- Margaret M Dekshenieks, Percy L Donaghay, James M Sullivan, Jan EB Rines, Thomas R Osborn, and Michael S Twardowski. Temporal and spatial occurrence of thin phytoplankton layers in relation to physical processes. *Marine Ecology Progress Series*, 223:61–71, 2001.
- Kenneth L Denman and Trevor Platt. The variance spectrum of phytoplankton in a turbulent ocean. *J. mar. Res*, 34(4):593–601, 1976.
- Scott C Doney, David M Glover, and Raymond G Najjar. A new coupled, one-dimensional biological-physical model for the upper ocean: Applications to the jgofs bermuda atlantic time-series study (bats) site. *Deep Sea Research Part II: Topical Studies in Oceanography*, 43(2):591–624, 1996.
- Daniel M Dubois. A model of patchiness for prey-predator plankton populations. *Ecological Modelling*, 1(1):67–80, 1975.

- Svend Duggen, Peter Croot, Ulrike Schacht, and Linn Hoffmann. Subduction zone volcanic ash can fertilize the surface ocean and stimulate phytoplankton growth: Evidence from biogeochemical experiments and satellite data. *Geophysical research letters*, 34(1):L01612, 2007.
- William M Durham and Roman Stocker. Thin phytoplankton layers: characteristics, mechanisms, and consequences. *Annual Review of Marine Science*, 4:177–207, 2012.
- William M Durham, Eric Climent, and Roman Stocker. Gyrotaxis in a steady vortical flow. *Physical Review Letters*, 106(23):238102, 2011a.
- William M Durham, Eric Climent, and Roman Stocker. Gyrotaxis in a steady vortical flow. *Physical Review Letters*, 106(23):238102, 2011b.
- William M Durham, Eric Climent, and Roman Stocker. Gyrotaxis in a steady vortical flow. *Physical Review Letters*, 106(23):238102, 2011c.
- William M Durham, Eric Climent, Michael Barry, Filippo De Lillo, Guido Boffetta, Massimo Cencini, and Roman Stocker. Turbulence drives microscale patches of motile phytoplankton. *Nature communications*, 4, 2013.
- J.J. Eiser and R.P. Hassett. A stoichiometric analysis of the zooplankton-phytoplankton interaction in marine and freshwater ecosystems. *Nature*, 370(6486):211–213, 1994.
- VW Ekman. On the influence of the earth's rotation on ocean currents. *Ark. Mat. Astron. Fys.*, 2:1–53, 1905.
- V Eswaran and SB Pope. An examination of forcing in direct numerical simulations of turbulence. *Computers & Fluids*, 16(3):257–278, 1988.
- Michael JR Fasham. Modelling the marine biota. *The global carbon cycle*, 1:15, 1993.
- MJR Fasham, HW Ducklow, and SM McKelvie. A nitrogen-based model of plankton dynamics in the oceanic mixed layer. *Journal of Marine Research*, 48(3):591–639, 1990.

- K Fennel, R Hetland, Y Feng, and S DiMarco. A coupled physical-biological model of the northern gulf of mexico shelf: model description, validation and analysis of phytoplankton variability. *Biogeosciences Discussions*, 8(1):121–156, 2011.
- H J S Fernando. Turbulent mixing in stratified fluids. *Annual Review of Fluid Mechanics*, 23(1):455–493, 1991.
- John R Fessler, Jonathan D Kulick, and John K Eaton. Preferential concentration of heavy particles in a turbulent channel flow. *Physics of Fluids*, 6(11):3742–3749, 1994.
- Øyvind Fiksen. Allocation patterns and diel vertical migration: modeling the optimal daphnia. *Ecology*, 78(5):1446–1456, 1997.
- V. Le Fouest, B. Zakardjian, F.J. Saucier, and S.A. izmeli. Application of seawifs- and avhrr-derived data for mesoscale and regional validation of a 3-d high-resolution physicalbiological model of the gulf of st. lawrence (canada). *Journal of Marine Systems*, 60(12):30 – 50, 2006. ISSN 0924-7963.
- Peter JS Franks. Thin layers of phytoplankton: A model of formation by near-inertial wave shear. *Deep Sea Research Part I: Oceanographic Research Papers*, 42(1):75–91, 1995.
- Peter JS Franks. Npz models of plankton dynamics: their construction, coupling to physics, and application. *Journal of Oceanography*, 58(2):379–387, 2002.
- PJS Franks, JS Wroblewski, and GR Flierl. Behavior of a simple plankton model with food-level acclimation by herbivores. *Marine Biology*, 91(1):121–129, 1986.
- Paul Frogner, Sigurdur Reynir Gíslason, and Niels Óskarsson. Fertilizing potential of volcanic ash in ocean surface water. *Geology*, 29(6):487–490, 2001.
- Peter S Galbraith, Howard I Browman, Roberto G Racca, Anne Berit Skiftesvik, and Jean-François Saint-Pierre. Effect of turbulence on the energetics of foraging in atlantic cod gadus morhua larvae. *Marine Ecology Progress Series*, 281:241–257, 2004.

- Brian Gaylord, Jason Hodin, and Matthew C Ferner. Turbulent shear spurs settlement in larval sea urchins. *Proceedings of the National Academy of Sciences*, 110(17): 6901–6906, 2013.
- Massimo Germano, Ugo Piomelli, Parviz Moin, and William H Cabot. A dynamic subgrid-scale eddy viscosity model. *Physics of Fluids A: Fluid Dynamics*, 3:1760, 1991.
- HL Grant, RW Stewart, and A Moilliet. Turbulence spectra from a tidal channel. *J. fluid Mech*, 12(2):241–268, 1962.
- Benni Winding Hansen. Zooplankton grazing and growth: Scaling within the 2-2,000 - μm body size range. *Limnol. Oceanogr*, 42:687–704, 1997.
- John Happel and Howard Brenner. *Low Reynolds number hydrodynamics: with special applications to particulate media*, volume 1. Springer, 1965.
- R.R. Harcourt and E.A. D’Asaro. Large-eddy simulation of langmuir turbulence in pure wind seas. *Journal of Physical Oceanography*, 38(7):1542–1562, 2008.
- Gary W Harrison. Global stability of predator-prey interactions. *Journal of Mathematical Biology*, 8(2):159–171, 1979.
- JO Hinze. *Turbulence: An introduction to its mechanisms and theory*. New York: McGraw-Hill, 1959.
- Robin J Hogan, Alan LM Grant, Anthony J Illingworth, Guy N Pearson, and Ewan J O’Connor. Vertical velocity variance and skewness in clear and cloud-topped boundary layers as revealed by doppler lidar. *Quarterly Journal of the Royal Meteorological Society*, 135(640):635–643, 2009.
- Song Hu, Changsheng Chen, Rubao Ji, David W Townsend, Rucheng Tian, Robert C Beardsley, and Cabell S Davis. Effects of surface forcing on interannual variability of the fall phytoplankton bloom in the gulf of maine revealed using a process-oriented model. *Mar. Ecol. Prog. Ser*, 427:29–49, 2011.

- Lesley Hughes. Biological consequences of global warming: is the signal already apparent? *Trends in Ecology & Evolution*, 15(2):56 – 61, 2000.
- Jef Huisman, Paul van Oostveen, and Franz J Weissing. Critical depth and critical turbulence: two different mechanisms for the development of phytoplankton blooms. *Limnology and Oceanography*, 44(7):1781–1787, 1999.
- M Ikeda and DD Šiljak. Lotka-volterra equations: decomposition, stability, and structure. *Journal of Mathematical Biology*, 9(1):65–83, 1980.
- H Jeffreys and BS Jeffreys. Methods of mathematical physics. *Mathematical Physics*, page 392, 1956.
- Ian R Jenkinson and Jun Sun. A model of pycnocline thickness modified by the rheological properties of phytoplankton exopolymeric substances. *Journal of Plankton Research*, 33(3):373–383, 2011.
- WP Jones and BE Launder. The prediction of laminarization with a two-equation model of turbulence. *International Journal of Heat and Mass Transfer*, 15(2):301–314, 1972.
- Mikael Jönsson, Lynn Ranåker, P Anders Nilsson, and Christer Brönmark. Prey-type-dependent foraging of young-of-the-year fish in turbid and humic environments. *Ecology of Freshwater Fish*, 21(3):461–468, 2012.
- L Karp-Boss, E Boss, and PA Jumars. Nutrient fluxes to planktonic osmotrophs in the presence of fluid motion. *Oceanography and Marine Biology*, 34:71–108, 1996.
- N. Keshishian, M. Nasr Esfahany, and N. Etesami. Experimental investigation of mass transfer of active ions in silica nanofluids. *International Communications in Heat and Mass Transfer*, 46(0):148 – 153, 2013.
- John Kim, Parviz Moin, and Robert Moser. Turbulence statistics in fully developed channel flow at low reynolds number. *Journal of Fluid Mechanics*, 177:133–166, 3 1987.

- Thomas Kiørboe, Houshuo Jiang, and Sean P Colin. Danger of zooplankton feeding: the fluid signal generated by ambush-feeding copepods. *Proceedings of the Royal Society B: Biological Sciences*, 277(1698):3229–3237, 2010.
- Andrei N Kolmogorov. Sulla teoria di volterra della lotta per lesistenza. *Giornale dell'Istituto italiano degli attuari*, 7:74–80, 1936.
- Andrey Nikolaevich Kolmogorov. Dissipation of energy in locally isotropic turbulence. In *Dokl. Akad. Nauk SSSR*, volume 32, pages 16–18, 1941.
- G. J. Komen. *Dynamics and modelling of ocean waves [electronic book] / [edited by] G. J. Komen ... [et al.]*. Online access with purchase: Cambridge Books Online. Cambridge : Cambridge University Press, 1994., 1994. ISBN 9780511628955.
- Robert H Kraichnan. Eddy viscosity in two and three dimensions. *Journal of the atmospheric sciences*, 33(8):1521–1536, 1976.
- Horace Lamb. *Hydrodynamics*. Cambridge University Press, 1932.
- Christiane Lancelot and Gilles Billen. Activity of heterotrophic bacteria and its coupling to primary production during the spring phytoplankton bloom in the southern bight of the north sea. *Limnology and oceanography*, 29(4):721–730, 1984.
- Christiane Lancelot, A De Montety, H Goosse, Sylvie Becquevort, Véronique Schoemann, Bénédicte Pasquer, and M Vancoppenolle. Spatial distribution of the iron supply to phytoplankton in the southern ocean: a model study. *Biogeosciences*, 6(12):2861–2878, 2009.
- Irving Langmuir. Surface motion of water induced by wind. *Science*, 87(2250):119–123, 1938.
- Michael I Latz, James F Case, and Robert L Gran. Excitation of bioluminescence by laminar fluid shear associated with simple couette flow. *Limnology and oceanography*, 39(6):1424–1439, 1994.

- Humphrey W Lean, Peter A Clark, Mark Dixon, Nigel M Roberts, Anna Fitch, Richard Forbes, and Carol Halliwell. Characteristics of high-resolution versions of the met office unified model for forecasting convection over the united kingdom. *Monthly Weather Review*, 136(9):3408–3424, 2008.
- M. Lesieur, P. Comte, E. Lamballais, O. Mtais, and G. Silvestrini. Large-eddy simulations of shear flows. *Journal of Engineering Mathematics*, 32(2-3):195–215, 1997.
- M Lévy, D Iovino, L Resplandy, P Klein, G Madec, A-M Tréguier, S Masson, and K Takahashi. Large-scale impacts of submesoscale dynamics on phytoplankton: Local and remote effects. *Ocean Modelling*, 43:77–93, 2012.
- Marina Lévy, Patrice Klein, and Anne-Marie Treguier. Impact of sub-mesoscale physics on production and subduction of phytoplankton in an oligotrophic regime. *Journal of Marine Research*, 59(4):535–565, 2001.
- PE Levy, MGR Cannell, and AD Friend. Modelling the impact of future changes in climate, CO₂ concentration and land use on natural ecosystems and the terrestrial carbon sink. *Global Environmental Change*, 14(1):21–30, 2004.
- Aleksandra M. Lewandowska, Petra Breithaupt, Helmut Hillebrand, Hans-Georg Hoppe, Klaus Jrgens, and Ulrich Sommer. Responses of primary productivity to increased temperature and phytoplankton diversity. *Journal of Sea Research*, 72(0): 87 – 93, 2012.
- DM Lewis. The orientation of gyrotactic spheroidal micro-organisms in a homogeneous isotropic turbulent flow. *Proceedings of the Royal Society of London. Series A: Mathematical, Physical and Engineering Sciences*, 459(2033):1293–1323, 2003a.
- DM Lewis. Planktonic encounter rates in homogeneous isotropic turbulence: the case of predators with limited fields of sensory perception. *Journal of theoretical biology*, 222(1):73–97, 2003b.

- DM Lewis. A simple model of plankton population dynamics coupled with a les of the surface mixed layer. *Journal of theoretical biology*, 234(4):565–591, 2005.
- DM Lewis and SI Bala. Plankton predation rates in turbulence: A study of the limitations imposed on a predator with a non-spherical field of sensory perception. *Journal of theoretical biology*, 242(1):44–61, 2006.
- DM Lewis and SE Belcher. Time-dependent, coupled, ekman boundary layer solutions incorporating stokes drift. *Dynamics of atmospheres and oceans*, 37(4):313–351, 2004.
- DM Lewis and AR Brereton. A mathematical study of the formation of spatial heterogeneities in the distribution of phytoplankton concentrations arising in a three dimensional model of the wind driven surface mixed layer. *Not yet submitted*, 2013.
- DM Lewis and TJ Pedley. Planktonic contact rates in homogeneous isotropic turbulence: theoretical predictions and kinematic simulations. *Journal of Theoretical Biology*, 205(3):377–408, 2000.
- DM Lewis and TJ Pedley. The influence of turbulence on plankton predation strategies. *Journal of Theoretical Biology*, 210(3):347–365, 2001.
- Marlon R Lewis. Variability of plankton and plankton processes on the mesoscale. *Phytoplankton Productivity Carbon Assimilation in Marine and Freshwater Ecosystems*, pages 141–155, 2002.
- Ming Li, Chris Garrett, and Eric Skyllingstad. A regime diagram for classifying turbulent large eddies in the upper ocean. *Deep Sea Research Part I: Oceanographic Research Papers*, 52(2):259–278, 2005.
- Shunxing Li, Fengjiao Liu, Fengying Zheng, Yuegang Zuo, and Xuguang Huang. Effects of nitrate addition and iron speciation on trace element transfer in coastal food webs under phosphate and iron enrichment. *Chemosphere*, 2013.
- Elena Litchman, Mark D Ohman, and Thomas Kiørboe. Trait-based approaches to zooplankton communities. *Journal of plankton research*, 35(3):473–484, 2013.

- SR Loarie, PB Duffy, GP Asner, CB Field, H Hamilton, and DD Ackerly. The velocity of climate change. *Nature*, 462(7276):1052–1055, 2009.
- Stephen P Long, Elizabeth A Ainsworth, Alistair Rogers, and Donald R Ort. Rising atmospheric carbon dioxide: plants face the future. *Annu. Rev. Plant Biol.*, 55: 591–628, 2004.
- Alfred J Lotka. Undamped oscillations derived from the law of mass action. *Journal of the american chemical society*, 42(8):1595–1599, 1920.
- S Lovejoy, WJS Currie, Y Tessier, MR Claereboudt, E Bourget, JC Roff, and D Schertzer. Universal multifractals and ocean patchiness: phytoplankton, physical fields and coastal heterogeneity. *Journal of plankton research*, 23(2):117–141, 2001.
- Gurvan Madec. Nemo ocean engine. ., 2008.
- A Mahadevan and JW Campbell. Biogeochemical patchiness at the sea surface. *Geophysical Research Letters*, 29(19):1926, 2002.
- Amala Mahadevan, Eric DAsaro, Craig Lee, and Mary Jane Perry. Eddy-driven stratification initiates north atlantic spring phytoplankton blooms. *Science*, 337(6090): 54–58, 2012.
- Edwin Malkiel, Jian Sheng, Joseph Katz, and J Rudi Strickler. The three-dimensional flow field generated by a feeding calanoid copepod measured using digital holography. *Journal of Experimental Biology*, 206(20):3657–3666, 2003.
- Adrian P Martin, Kelvin J Richards, Annalisa Bracco, and Antonello Provenzale. Patchy productivity in the open ocean. *Global Biogeochemical Cycles*, 16(2):9–1, 2002.
- AP Martin. Phytoplankton patchiness: the role of lateral stirring and mixing. *Progress in Oceanography*, 57(2):125–174, 2003.

- Elodie Martinez, David Antoine, and Dionysios Raitsos. Multi-decadal variability of phytoplankton and related physical forcing in the north atlantic ocean. In *Earth Observation for Ocean-Atmosphere Interactions Science*, 2011.
- J Maurer, P Tabeling, and G Zocchi. Statistics of turbulence between two counter-rotating disks in low-temperature helium gas. *EPL (Europhysics Letters)*, 26(1):31, 1994.
- DJ McGillicuddy, AR Robinson, DA Siegel, HW Jannasch, R Johnson, TD Dickey, J McNeil, AF Michaels, and AH Knap. Influence of mesoscale eddies on new production in the sargasso sea. *Nature*, 394(6690):263–266, 1998.
- MA McManus, AL Alldredge, AH Barnard, Emmanuel Boss, JF Case, TJ Cowles, PL Donaghay, LB Eisner, DJ Gifford, and CF Greenlaw. Characteristics, distribution and persistence of thin layers over a 48 hour period. *Marine Ecology-Progress Series*, 261:1, 2003.
- Margaret A McManus, Olivia M Cheriton, Patrick J Drake, DV Holliday, Curt D Storlazzi, Percy L Donaghay, and Charles F Greenlaw. Effects of physical processes on structure and transport of thin zooplankton layers in the coastal ocean. *Marine Ecology Progress Series*, 301:199–215, 2005.
- Margaret A McManus, Raphael M Kudela, Mary W Silver, Grieg F Steward, Percy L Donaghay, and James M Sullivan. Cryptic blooms: Are thin layers the missing connection? *Estuaries and Coasts*, 31(2):396–401, 2008.
- Abigail McQuatters-Gollop, Philip C Reid, Martin Edwards, Peter H Burkill, Claudia Castellani, Sonia Batten, Winfried Gieskes, Doug Beare, Robert R Bidigare, Erica Head, Rod Johnson, Mati Kahru, J Anthony Koslow, and Angelica Pena. Is there a decline in marine phytoplankton?. *Nature*, 472(7342):E6, 2011.
- JAMES C McWilliams, Peter P Sullivan, and Chin-Hoh Moeng. Langmuir turbulence in the ocean. *Journal of Fluid Mechanics*, 334(1):1–30, 1997.

- Susanne Menden-Deuer and Daniel Grünbaum. Individual foraging behaviors and population distributions of a planktonic predator aggregating to phytoplankton thin layers. *Limnology and Oceanography*, 51(1):109–116, 2006.
- SA Mirbagheri, SA Sadrnejad, and SA Hashemi Monfared. Phytoplankton and zooplankton modeling of pishin reservoir by means of an advection-diffusion drought model. *International Journal of Environmental Research*, 6(1):163–172, 2011.
- Parviz Moin and John Kim. Numerical investigation of turbulent channel flow. *Journal of Fluid Mechanics*, 118:341–377, 1982.
- Mark A Moline, Kelly J Benoit-Bird, Ian C Robbins, Maddie Schroth-Miller, Chad M Waluk, and Brian Zelenke. Integrated measurements of acoustical and optical thin layers ii: Horizontal length scales. *Continental Shelf Research*, 30(1):29–38, 2010.
- AS Monin and AM Yaglom. *Statistical Fluid Mechanics: Mechanics of Turbulence*, volume 2. MIT Press, Cambridge, Mass, 1975.
- Willard S Moore. The effect of submarine groundwater discharge on the ocean. *Annual review of marine science*, 2:59–88, 2010.
- José H Muelbert, Marlon R Lewis, and Dan E Kelley. The importance of small-scale turbulence in the feeding of herring larvae. *Journal of plankton research*, 16(8):927–944, 1994.
- Koenraad Muylaert, Carmen Pérez-Martínez, Pedro Sánchez-Castillo, Torben L Lauridsen, Maarten Vanderstukken, Steven AJ Declerck, Katleen Van der Gucht, José-Maria Conde-Porcuna, Erik Jeppesen, Luc De Meester, et al. Influence of nutrients, submerged macrophytes and zooplankton grazing on phytoplankton biomass and diversity along a latitudinal gradient in europe. *Hydrobiologia*, 653(1):79–90, 2010.
- CL Navier. Mémoire sur les lois du mouvement des fluides. *Mémoires de l'Académie Royale des Sciences de l'Institut de France*, 6:389–440, 1827.

- Mark D Ohman. The demographic benefits of diel vertical migration by zooplankton. *Ecological Monographs*, pages 257–281, 1990.
- C Oseen. Über die stokes sche formel und über eine verwandte aufgabe in der hydrodynamik. *Ark Mat Aston Fys*, 6:69, 1910.
- Daniel M Palacios. Factors influencing the island-mass effect of the galapagos archipelago. *Geophysical Research Letters*, 29(23):2134, 2002.
- JB Palter, JL Sarmiento, A Gnanadesikan, J Simeon, and RD Slater. Fueling export production: Nutrient return pathways from the deep ocean and their dependence on the meridional overturning circulation. *Biogeosciences*, 7:3549–3568, 2010.
- HL Pécseli, J Trulsen, and Ø Fiksen. Predator–prey encounter and capture rates for plankton in turbulent environments. *Progress in Oceanography*, 101(1):14–32, 2012.
- T.J. Pedley and J.O. Kessler. New continuum model for suspensions of gyrotactic micro-organisms. *Journal of Fluid Mechanics*, 212:155–182, 1990.
- Frank Peeters, Onur Kerimoglu, and Dietmar Straile. Implications of seasonal mixing for phytoplankton production and bloom development. *Theoretical Ecology*, pages 1–15, 2013.
- V Pérez-Muñuzuri and F Huhn. The role of mesoscale eddies time and length scales on phytoplankton production. *Nonlinear Processes in Geophysics*, 17(2):177–186, 2010.
- Owen M Phillips. *The dynamics of the upper ocean*. Cambridge university press, 1977.
- JL Pinckney, HW Paerl, MB Harrington, and KE Howe. Annual cycles of phytoplankton community-structure and bloom dynamics in the neuse river estuary, north carolina. *Marine Biology*, 131(2):371–381, 1998.
- Thomas M Powell and Akira Okubo. Turbulence, diffusion and patchiness in the sea. *Philosophical Transactions of the Royal Society of London. Series B: Biological Sciences*, 343(1303):11–18, 1994.

- Holly J Price. Feeding mechanisms in marine and freshwater zooplankton. *Bulletin of Marine Science*, 43(3):327–343, 1988.
- Edward M Purcell. Life at low reynolds number. In *AIP Conference Proceedings*, volume 28, page 49, 1976.
- S. Ratti, A. H. KNOLL, and M. GIORDANO. Did sulfate availability facilitate the evolutionary expansion of chlorophyll a+c phytoplankton in the oceans? *Geobiology*, 9(4):301–312, 2011.
- R. Reigada, R. M. Hillary, M. A. Bees, J. M. Sancho, and F. Sagus. Plankton blooms induced by turbulent flows. *Proceedings of the Royal Society of London. Series B: Biological Sciences*, 270(1517):875–880, 2003.
- Osborne Reynolds. On the dynamical theory of incompressible viscous fluids and the determination of the criterion. *Philosophical Transactions of the Royal Society of London. A*, 186:123–164, 1895.
- Lewis F Richardson. Some measurements of atmospheric turbulence. *Philosophical Transactions of the Royal Society of London. Series A, Containing Papers of a Mathematical or Physical Character*, 221:1–28, 1921.
- Courtney E Richmond, Kenneth A Rose, and Denise L Breitburg. Individual variability and environmental conditions: effects on zooplankton cohort dynamics. *MEPS*, 486: 59–78, 2013.
- JEB Rines, MN McFarland, PL Donaghay, and JM Sullivan. Thin layers and species-specific characterization of the phytoplankton community in monterey bay, california, usa. *Continental Shelf Research*, 30(1):66–80, 2010.
- Tom P Rippeth, Eirwen Williams, and John H Simpson. Reynolds stress and turbulent energy production in a tidal channel. *Journal of Physical Oceanography*, 32(4):1242–1251, 2002.

- BJ Rothschild and TR Osborn. Small-scale turbulence and plankton contact rates. *Journal of Plankton Research*, 10(3):465–474, 1988.
- Shovonlal Roy, David S Broomhead, Trevor Platt, Shubha Sathyendranath, and Stefano Ciavatta. Sequential variations of phytoplankton growth and mortality in an npz model: A remote-sensing-based assessment. *Journal of Marine Systems*, 92(1):16–29, 2012.
- John P. Ryan, Margaret A. McManus, and James M. Sullivan. Interacting physical, chemical and biological forcing of phytoplankton thin-layer variability in monterey bay, california. *Continental Shelf Research*, 30(1):7 – 16, 2010.
- JP Ryan, MA McManus, JD Paduan, and FP Chavez. Phytoplankton thin layers caused by shear in frontal zones of a coastal upwelling system. *Marine Ecology-Progress Series*, 354:21, 2008.
- Pierre Sagaut. *Large eddy simulation for incompressible flows*, volume 3. Springer Berlin, 2000.
- Lawrence P Sanford. Turbulent mixing in experimental ecosystem studies. *Marine Ecology Progress Series*, 161:265–293, 1997.
- Thomas B Sanford, James F Price, and James B Girton. Upper-ocean response to hurricane frances (2004) observed by profiling em-apex floats. *Journal of Physical Oceanography*, 41(6):1041–1056, 2011.
- U Schumann. Subgrid scale model for finite difference simulations of turbulent flows in plane channels and annuli. *Journal of computational physics*, 18(4):376–404, 1975.
- S Servidio, V Carbone, P Dmitruk, and WH Matthaeus. Time decorrelation in isotropic magnetohydrodynamic turbulence. *EPL (Europhysics Letters)*, 96(5):55003, 2011.
- Laurent Seuront, François Schmitt, Yvan Lagadeuc, Daniel Schertzer, Shaun Lovejoy, and Serge Frontier. Multifractal analysis of phytoplankton biomass and temperature in the ocean. *Geophysical Research Letters*, 23(24):3591–3594, 1996.

- Virginie Sibert, Bruno Zakardjian, Michel Gosselin, Michel Starr, Simon Senneville, and Yvonnick LeClainche. 3d bio-physical model of the sympagic and planktonic productions in the hudson bay system. *Journal of Marine Systems*, 88(3):401–422, 2011.
- Andrew Sih. Prey refuges and predator-prey stability. *Theoretical Population Biology*, 31(1):1–12, 1987.
- Eric D Skyllingstad and Donald W Denbo. An ocean large-eddy simulation of langmuir circulations and convection in the surface mixed layer. *Journal of Geophysical Research: Oceans (1978–2012)*, 100(C5):8501–8522, 1995.
- J Smagorinsky. General circulation experiments with the primitive equations. *Mon. Weath. Rev.*, 91(3):99–164, 1963.
- Jerome A Smith. Observed growth of langmuir circulation. *Journal of Geophysical Research: Oceans (1978–2012)*, 97(C4):5651–5664, 1992.
- Ulrich Sommer and Aleksandra Lewandowska. Climate change and the phytoplankton spring bloom: warming and overwintering zooplankton have similar effects on phytoplankton. *Global Change Biology*, 17(1):154–162, 2011.
- Hongjun Song, Rubao Ji, Charles Stock, and Zongling Wang. Phenology of phytoplankton blooms in the nova scotian shelf–gulf of maine region: remote sensing and modeling analysis. *Journal of plankton research*, 32(11):1485–1499, 2010.
- J Hi Steele. Environmental control of photosynthesis in the sea. *Limnology and Oceanography*, 7(2):137–150, 2006.
- JH Steele and EW Henderson. A simple plankton model. *American Naturalist*, pages 676–691, 1981.
- Jonah V Steinbeck, Amatzia Genin, Stephen G Monismith, Jeffrey R Koseff, Roi Holzman, and Rochelle G Labiosa. Turbulent mixing in fine-scale phytoplankton layers:

- Observations and inferences of layer dynamics. *Continental Shelf Research*, 30(5): 442–455, 2010.
- George Gabriel Stokes. On the theory of oscillatory waves. *Trans Cambridge Philos Soc*, 8:441–473, 1847.
- George Gabriel Stokes. *On the effect of the internal friction of fluids on the motion of pendulums*, volume 9. Pitt Press, 1851.
- Dietmar Straile. Gross growth efficiencies of protozoan and metazoan zooplankton and their dependence on food concentration, predator-prey weight ratio, and taxonomic group. *Limnology and Oceanography*, 42(6):1375–1385, 1997.
- Lester K. Su and Noel T. Clemens. The structure of fine-scale scalar mixing in gas-phase planar turbulent jets. *Journal of Fluid Mechanics*, 488:1–29, 6 2003.
- James M Sullivan, Percy L Donaghay, and Jan EB Rines. Coastal thin layer dynamics: consequences to biology and optics. *Continental Shelf Research*, 30(1):50–65, 2010a.
- James M Sullivan, Percy L Donaghay, and Jan EB Rines. Coastal thin layer dynamics: consequences to biology and optics. *Continental Shelf Research*, 30(1):50–65, 2010b.
- P. P. Sullivan, L. Romero, J. C. McWilliams, and W. K. Melville. Transient evolution of langmuir turbulence in ocean boundary layers driven by hurricane winds and waves. *Journal of Physical Oceanography*, 42(11):1959 – 1980, 2012.
- Peter P Sullivan and Edward G Patton. The effect of mesh resolution on convective boundary layer statistics and structures generated by large-eddy simulation. *Journal of the Atmospheric Sciences*, 68(10):2395–2415, 2011a.
- Peter P Sullivan, James C McWilliams, and Chin-Hoh Moeng. A subgrid-scale model for large-eddy simulation of planetary boundary-layer flows. *Boundary-Layer Meteorology*, 71(3):247–276, 1994.

- P.P. Sullivan and E.G. Patton. The effect of mesh resolution on convective boundary layer statistics and structures generated by large-eddy simulation. *Journal of the Atmospheric Sciences*, 68(10):2395–2415, 2011b.
- Alessandro Tagliabue, Laurent Bopp, Jean-Claude Dutay, Andrew R Bowie, Fanny Chever, Philippe Jean-Baptiste, Eva Bucciarelli, Delphine Lannuzel, Tomas Remyeni, and Géraldine Sarthou. Hydrothermal contribution to the oceanic dissolved iron inventory. *Nature Geoscience*, 3(4):252–256, 2010.
- John R Taylor and Raffaele Ferrari. Shutdown of turbulent convection as a new criterion for the onset of spring phytoplankton blooms. *Limnol. Oceanogr*, 56(6):2293–2307, 2011.
- John R Taylor and Roman Stocker. Trade-offs of chemotactic foraging in turbulent water. *Science*, 338(6107):675–679, 2012.
- Hendrik Tennekes and John Leask Lumley. *A first course in turbulence*. The MIT press, 1972.
- Graeme J Thorn and Rachel N Bearon. Transport of spherical gyrotactic organisms in general three-dimensional flow fields. *Physics of Fluids*, 22:041902, 2010.
- Peter Tiselius, Per R Jonsson, Stein Kaartvedt, Esben Moland Olsen, and Tom Jørstad. Effects of copepod foraging behavior on predation risk: an experimental study of the predatory copepod *pareuchaeta norvegica* feeding on *acartia clausi* and *a. tonsa* (copepoda). *Limnology and oceanography*, 42(1):164–170, 1997.
- ED Traganza, DA Nestor, and AK McDonald. Satellite observations of a nutrient upwelling off the coast of california. *Journal of Geophysical Research: Oceans (1978–2012)*, 85(C7):4101–4106, 1980.
- André W Visser, Patrizio Mariani, and Simone Pigolotti. Swimming in turbulence: zooplankton fitness in terms of foraging efficiency and predation risk. *Journal of plankton research*, 31(2):121–133, 2009.

- Vito Volterra. Fluctuations in the abundance of a species considered mathematically. *Nature*, 118:558–560, 1926.
- OF Voropayeva and GG Chernykh. Numerical modeling of interaction between a turbulent mixing zone and a local perturbation of the density field in a pycnocline. *Journal of applied mechanics and technical physics*, 51(2):182–192, 2010.
- Thomas S Weber and Curtis Deutsch. Ocean nutrient ratios governed by plankton biogeography. *Nature*, 467(7315):550–554, 2010.
- Robert A Weller. The relation of near-inertial motions observed in the mixed layer during the jasin (1978) experiment to the local wind stress and to the quasi-geostrophic flow field. *Journal of Physical Oceanography*, 12(10):1122–1136, 1982.
- EA Widder, S Johnsen, SA Bernstein, JF Case, and DJ Neilson. Thin layers of bioluminescent copepods found at density discontinuities in the water column. *Marine Biology*, 134(3):429–437, 1999.
- Richard G Williams. Ocean eddies and plankton blooms. *Nature Geoscience, News and Views*, 4(11):739–740, 2011.
- Richard G Williams and Michael J Follows. The ekman transfer of nutrients and maintenance of new production over the north atlantic. *Deep Sea Research Part I: Oceanographic Research Papers*, 45(2):461–489, 1998.
- V Yakhot and Steven A Orszag. Renormalization group formulation of large eddy simulation. In *Nonlinear Dynamics of Transcritical Flows*, pages 155–174. Springer, 1985.
- V. Yakhot, S.A. Orszag, and R. Panda. Computational test of the renormalization group theory of turbulence. *Journal of Scientific Computing*, 3(2):139–147, 1988.
- Hidekatsu Yamazaki and Daniel Kamykowski. The vertical trajectories of motile phytoplankton in a wind-mixed water column. *Deep Sea Research Part A. Oceanographic Research Papers*, 38(2):219–241, 1991.

Bo Yao, Beidou Xi, Chunming Hu, Shouliang Huo, Jing Su, and Hongliang Liu. A model and experimental study of phosphate uptake kinetics in algae: Considering surface adsorption and p-stress. *Journal of Environmental Sciences*, 23(2):189–198, 2011.